A Thesis Submitted for the Degree of PhD at the University of Warwick

Permanent WRAP URL:

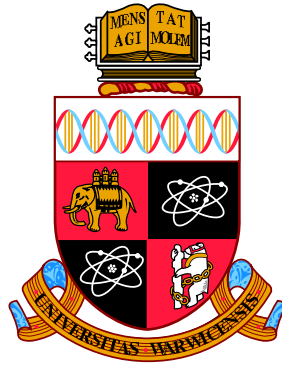http://wrap.warwick.ac.uk/161788

warwick.ac.uk/lib-publications

Bidirectional transport on microtubules: cooperation of Kif1C and dynein

Alexander James Zwetsloot
BSc. (Hons) MSc.

A thesis submitted in fulfilment
of the requirements for the degree of

Doctor of Philosophy in Interdisciplinary Biomedical Research

Warwick Medical School, University of Warwick

March 2021

Supervised by:
Dr. François Nédélec
Sainsbury Laboratory, University of Cambridge, UK

Prof. Anne Straube
Centre for Mechanochemical Cell Biology, University of Warwick, UK

Contents

List of Figures

v

List of Tables

Acknowledgements

I'd like to thank my colleagues and friends at the Centre for Mechanochemical Cell Biology for creating an exciting and collaborative environment in which to do science: members of Computing and Advanced Microscopy Unit (CAMDU) whom keep microscopy hardware functioning; Daniel Roth, a research assistant in the Straube lab, for being available to help with all problems whether personal or professional; Naomi Sheppard for her help in teaching me not to let the ÄKTA sense your fear; and Nida Siddiqui for her patience in helping me get started with single molecule microscopy.

The MRC doctoral training partnership has been a family during my time at the University of Warwick, creating an inclusive environment and a sense of belonging with cohort events and retreats. Sally Blakeman, especially, is a wonderful person who gave me some of the best pastoral support I've had over the course of my PhD.

Our work on dynein here was possible due to a generous collaboration with Andrew Carter's lab. Their entire lab welcomed me in on visits to the MRC-LMB where I got to marvel at pure excellence of the science going on there. I will always remember my times smashing frozen pig brains with Caroline Stone fondly, and Ferdos Abid Ali holds responsibility for opening my eyes to the beautiful results that can be found from electron microscopy.

I thank the members of the Straube lab, past and present, who have handed down their knowledge which I rarely received quietly. I would like to thank the undergraduate students, Elly Straube and Julia Schander, who gave me vital experience in supervising projects, and produced high quality research during their time in our lab. Of course the biggest thanks go to Anne Straube herself, who encouraged me to take on a wildly challenging project, always let me take detours to do the fun experiments that might not work, and who is always there to make me feel better when I feel the side-effects of failure.

Declarations and Attribution

I, Alexander Zwetsloot, declare that:

- This thesis is my own work except where it contains work based on collaborative research, in which case the nature and extent of the author's individual contribution shall be indicated.

- This thesis is submitted to the University of Warwick in support of my application for the degree of Doctor of Philosophy. It has been composed by myself and has not been submitted in any previous application for any degree.

The work presented (including data generated and data analysis) was carried out by the author except in the cases outlined below:

- Figure 3.1: motor-GFP plasmid was cloned by Nida Siddiqui.

- Figure 3.10: Analysis of KIF1C-ΔS-GFP landing rate was performed by Nida Siddiqui.

- Figure 3.2: MST experiment was performed and analysed by Anne Straube.

- Figure 3.5: cloning of shRNAs, data acquisition and image analysis in this section were performed in large part by Elly Straube, a student under the author's supervision while completing this work

- Section 4.1: imaging and data processing of DmrB-KIF1C in cells was performed by Elly Straube under the author's supervision. Elly also cloned some of the DmrB plasmids used in this experiment.

- Section 4.2: Most of the imaging of peroxisomes in cells was performed by Julia Schander, a student under the author's supervison. Julia also did some of the TrackMate tracking of peroxisomes.

- Chapter 5: All dynein-TMR, dynactin and FHF complex used in this chapter were purified by Caroline Stone and Ferdos Abid Ali at the MRC Laboratory of Molecular Biology. The author assisted on some of these protein purifications.

Parts of this thesis have been published by the author:

- Siddiqui, N.*, Zwetsloot, A.J.*, Bachmann, A., Roth, D., Hussain, H., Brandt, J., Kaverina, I. and Straube, A., (2019). PTPN21 and Hook3 relieve KIF1C autoinhibition and activate intracellular transport. *Nature communications*, 10(1), pp.1-16.

- Zwetsloot, A. J., Tut, G., and Straube, A. (2018). Measuring microtubule dynamics. *Essays in biochemistry*, 62(6), pp.725-735.

Abstract

Cells utilise their microtubule cytoskeletal network for transport of cargoes ranging in size from small vesicles to large organelles, and even the nucleus. Kinesin motor proteins transport cargoes towards the plus-end of microtubules, while dynein is responsible for minus-end directed transport. Inside cells, cargoes can be seen to frequently change direction on microtubules, indicating that cargoes have both types of molecular motor bound, and that there exists a mechanism that allows switching between directionality. Bidirectionality likely allows cargoes to avoid obstacles and to rapidly search the cytoplasm for their destination, and kinesin and dynein's functions are interlinked such that depletion of a kinesin is sufficient to disrupt dynein-driven transport and vice versa. A mechanism of bidirectional transport that explains this co-dependence of opposite polarity motors is yet to be elaborated.

A potential key player in bidirectional transport is the kinesin-3 KIF1C, which has been shown to interact with multiple dynein adaptors, and in doing so may link itself to dynein. Using *in vitro* reconstitution, we investigated the mechanism of activation of KIF1C and found that the dynein adaptor Hook3 is able to relieve its autoinhibition. In single-molecule microscopy assays, Hook3, but not BICD2 and BICDR1, frequently forms co-motile complexes. Using a rapamycin-induced cargo transport assay in cells, we found Hook3 driven intracellular transport is rapid, bidirectional, and sensitive to the concentration of active KIF1C. Using an acutely inhibitable KIF1C, we revealed that KIF1C inside the cell is physically interlinked with dynein on short timescales. *In vitro* reconstitution of a co-complex of KIF1C and dynein in the presence of dynactin and Hook3 showed bidirectional motility in single-molecule microscopy assays, and codependence of opposite polarity motors was reconstituted for the first time as dynein's motility improves in the presence of KIF1C by acting as a processivity tether. We developed a method to measure the intensity of running motors and found that KIF1C promotes the formation of complexes containing two dynein dimers. We propose that dynein/kinesin co-complexes may be better able to avoid microtubule obstacles, and predict that other dynein adaptor proteins may permit the formation of yet uncharacterised dynein/kinesin co-complexes.

Acronyms and abbreviations

BICD   Bicaudal D

BICD1   Bicaudal D homolog 1

BICD2   Bicaudal D homolog 2

BICDR1   Bicaudal D-related protein 1

CVs   column volumes

DCV   dense core vesicle

DDFHF   dynein-dynactin-FHF

DDFHFK   dynein-dynactin-FHF-KIF1C

DDH   dynein-dynactin-Hook3

DDHK   dynein-dynactin-Hook3-KIF1C

DDH-KS   dynein-dynactin-Hook3-KIF1C-stalk

DLIC2   cytoplasmic dynein 1 light intermediate chain 2

DYT   double yeast tryptone broth

FHF   FAM160A2/Hook/FTS

FTS   Fused Toes

HK   KIF1C-Hook3

IC2C   cytoplasmic dynein 1 intermediate chain 2

Lis1   Lissencephaly-1

MAPs   microtubule associated proteins

MCAK   Mitotic centromere-associated kinesin

MST   microscale thermophoresis

NIN   Ninein

NINL   Ninein-like

NPY	Neuropeptide-Y
PEI	polyethylenimine
ROI	region of interest
ROIs	regions of interest
SP	Sulfopropyl
Sf9	*Spodoptera frugiperda*
TIRF	total internal reflection fluorescence
TMAO	Trimethylamine N-oxide
TMR	tetramethylrhodamine
shRNA	short hairpin RNA
siRNA	small interfering RNA

Chapter 1

Introduction

1.1   Microtubules for structure and transport

Microtubules are long dynamic structures of αβ-tubulin heterodimers found in most eukaryotic cells (Mitchison & Kirschner, 1984; Nogales, 2001). Protofilaments are formed by the end-to-end attachment of tubulin heterodimers, and typically, thirteen protofilaments bind laterally to create a hollow tubule (Alushin et al., 2014; Nogales, 2001). These microtubules grow by the addition of GTP-bound tubulin heterodimers to the plus-end. Incorporation into the lattice stimulates GTPase activity within the individual subunits. While GTP-bound tubulin is present at the tip, microtubules continue to grow, however when GDP tubulin is exposed at the tip because GTP hydrolysis exceeds the rate of GTP-tubulin addition, microtubules become unstable and depolymerise. Thus microtubule dynamic instability is the switch between stable phases of growth and rapid shrinkage, and this depends on the delicate balance between GTP hydrolysis and the arrival of GTP-bound tubulin heterodimers (Hyman et al., 1992). The switch from elongation to shrinkage upon GTP cap loss is known as catastrophe, while the event of a shrinking microtubule end reverting to growth is known as rescue (see Figure 1.1 a.) (Mitchison & Kirschner, 1984).

One of the most prominent roles of microtubules is the formation of the mitotic spindle. During mitosis, microtubules first align chromosomes in metaphase, then separate sister chromatids in anaphase, and finally together with actin, separate the two daughter cells during cytokinesis (Auckland & McAinsh, 2015; Forth & Kapoor, 2017). Microtubules work alongside two other cytoskeleton components, actin and intermediate filaments, to both gen-

erate and maintain cellular structure, morphology and self-organization. In non-specialised cells, most microtubules are nucleated from the centrosome and the Golgi apparatus that are both located close to the nucleus, and the microtubule plus ends extend outwards towards the cell periphery. However, in differentiated cell types, microtubule structure and distribution is specifically tuned for the cellular function. For example, neuronal cells must maintain polarised bundles of microtubules within their axons and dendrites throughout the lifetime of an animal to allow correct sorting of molecular motors and cargoes (Tas et al., 2017). Muscle cells generate paraxial arrays of microtubules to enable polarisation and elongation, and resist contractile forces (Mogessie et al., 2015). Therefore microtubules are important in most cell types in all stages of the cell cycle.

The dynamic instability of microtubules enables the cytoskeleton to be rebuilt on relatively short timescales, and different arrangements of microtubules are stabilised or destabilised by the concerted action of microtubule associated proteins (MAPs) and motors, while changes in tubulin itself (either through isotype or post-translational modification) may also contribute.

For example, the protein Tau is able to increase microtubule length and stability and is important in axon specification (Black et al., 1996). Tau binds to both the lattice and dynamic ends of microtubules, and is thought to exert its stabilising effect on the labile GTP cap to promote microtubule assembly (Breuzard et al., 2013; Qiang et al., 2018). *In vitro*, tau also undergoes liquid-liquid phase separation and phase-separated Tau is able to locally concentrate tubulin leading to nucleation of new microtubules, though it is not yet known whether this is a physiological role of Tau or whether it may in fact contribute towards the pathological effects of Tau aggregation in neurodegenerative diseases (Hernández-Vega et al., 2017; Wegmann et al., 2018). Similarly, MAP4 which shares homology to Tau in its repeated microtubule binding regions, was found to stabilise microtubules in cells (Bulinski & Borisy, 1980; Nguyen et al., 1997), and its proline rich region stimulates microtubule nucleation *in vitro* (Tokuraku et al., 1999). Just as MAPs and motors can stabilise microtubules, they can also destabilise them. The kinesin Mitotic centromere-associated kinesin (MCAK) has an ATPase cycle specialised for microtubule disassembly. (Friel & Howard, 2011; Wordeman & Mitchison, 1995)

The behaviour of microtubules is also changed by the building blocks they are made from. Distinct isoforms of β-tubulin are conserved between vertebrates and may have functional significance. βI, βII and βIII-tubulin are

found to localise distinctly using immunofluorescence in neuroblastoma cell lines, where βII-tubulin localises almost exclusively to neurites and its depletion correlates with decreased neurite outgrowth (J. Guo et al., 2010). It is now clear that transport of specific tubulin mRNAs by kinesin-2 and their localised translation could be one way in which localisation of tubulin isoforms could be achieved (Baumann et al., 2020). β-tubulin isoform expression levels also correlate with the response of cancer patients to paclitaxel, suggesting different β-tubulin isotypes could generate microtubules with different dynamic properties (Parker et al., 2017). Indeed, reconstitution experiments with purified tubulin isotypes show that dynamicity of microtubules can be altered by the amount of βII/III-tubulin incorporated. (Pamula et al., 2016; Panda et al., 1994)

In vitro reconstitution is typically performed with tubulin purified from animal brains, and therefore contains a mixture of tubulin isoforms. It is becoming more common for researchers to purify specific isotypes of tubulin to consider their effects.(Ti et al., 2018; Vemu et al., 2016) *In vitro*, different isoforms of tubulin have been found to determine microtubule protofilament number, while also controlling the susceptibility of microtubules to depolymerising agents such as MCAK and chTOG (Ti et al., 2018). Thus local control over tubulin isoform expression, or cell-type specific expression of tubulin isoforms, may provide a mechanism for cells to generate the cytoskeleton that best fits their function.

In addition to changing the isoform of tubulin used to build the microtubule, tubulin subunits also undergo post-translational modifications. Historically there was some debate about whether these directly influenced the microtubule's behaviour, or whether they are accumulated over the lifetime of a microtubule and instead act to identify subsets of microtubules within the cell or modulate the transport that occurs along them. Sirajuddin et al. purified 25-different α/β tubulin heterodimers with distinct C-terminal tail types or post-translational modifications, and found that kinesin-1 is sensitive to βIII-tubulin polyglutamylation, whereas kinesin-2 requires detyrosinated α-tubulin for maximal processivity (Sirajuddin et al., 2014). Polyamination of microtubules appears to correlate with neurite outgrowth and axonal microtubule stability in the neurone-like SH-SY5Y cell line (Song et al., 2013). Tubulin isoforms and modifications have surmassed a large and active body of literature in the last ten years, and this has recently been comprehensively reviewed by Janke and Magiera (2020).
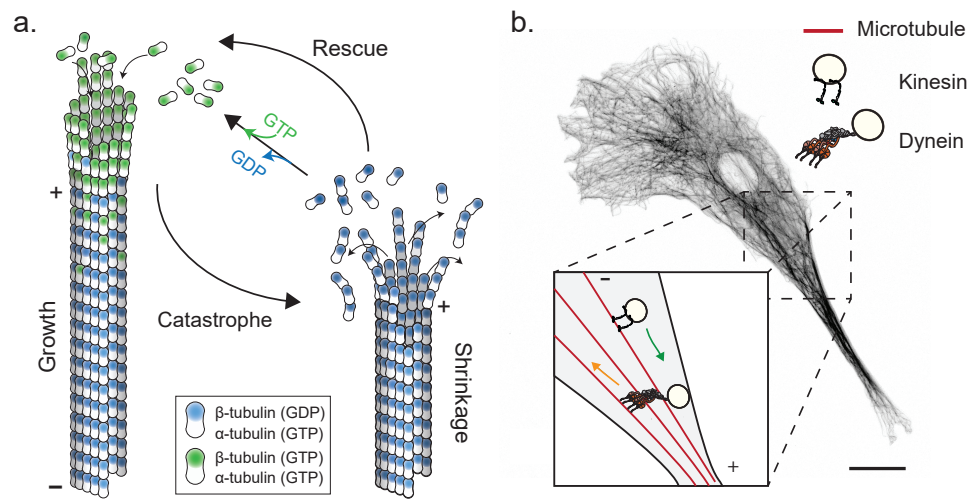
Figure 1.1: Microtubules are a dynamic skeleton that facilitates molecular motor transport | a. Microtubules grow and shrink through addition and removal of αβ-tubulin heterodimers. Stability is governed by the GTP-cap, which degrades over time as GTP is hydrolysed to GDP. Without continuous addition of new tubulin heterodimers, microtubules undergo catastrophe, while re-addition of GTP-bound tubulin heterodimers can revert the microtubule to a growth phase (replicated from Zwetsloot et al. (2018)). **b.** Microtubules span the whole cell, emerging from the periphery of the nucleus where their minus ends are anchored, towards the outside of the cell with their plus-ends. The kinesin family of molecular motors undertakes cargo transport along microtubules towards the plus end, while dynein is minus-end directed. Scale bar is 20 μm. The cell is a myoblast stained with anti-tubulin antibody imaged by Clare Garcin.

As well as providing the cell structural integrity, microtubules are the tracks for the molecular motors kinesin and dynein, which hydrolyse ATP to generate force that is most commonly used to translocate along the track (see Figure 1.1 b.). The cargoes these motors transport are diverse, ranging from small ones such as endosomes and mRNAs, all the way up to large ones like mitochondria and the nucleus, and peturbation in this transport can have severe physiological consequences.

1.2 Kinesin-3 members undertake long-range processive intracellular transport

The kinesin superfamily of motor proteins primarily undertake plus-end driven transport along microtubules. The human cell's repertoire of kinesins amasses 45 members, typically sub-divided into 17 families based broadly on their function, structure, and sequence similarity (Miki et al., 2005; Wickstead & Gull, 2006). These kinesin families have conserved roles within the cell, such as kinesin-3 family members which provide organelle transport, kinesin-5s which play important roles in mitosis, and kinesin-1s which undertake axonal transport (Ferenz et al., 2011; Maday et al., 2014; Siddiqui & Straube, 2017).

The mechanism of kinesin stepping is thought to be broadly similar between kinesins, but is most commonly studied for kinesin-1 family members. The mechanochemical cycle of kinesin starts with one of the two motor heads bound, and the second unbound and trailing the attached head. ATP binding to the bound head is followed by hydroylsis to ADP, and this is coupled to the motion of swinging the unbound trailing head forwards and allowing it to attach to the microtubule. Release of phosphate permits the now trailing bound head to release its attachment to the microtubule, and the cycle repeats, alternating which head is bound at any one time (Hancock, 2016). The neck linker of the kinesin motor domain, which is a short amino acid tether between the catalytic core of the enzyme and the C-terminal portion of the protein which binds cargoes, is important for its directionality and ability to sustain force, though the exact mechanism of this is debated (Budaitis et al., 2019). One idea is that during ATP hydrolysis while the trailing head is being moved forwards, the attached head docks its neck linker when the moving head is in an optimal position, thus limiting the unbound head's binding opportunities to sites further along the microtubule (Z. Zhang et al., 2017).

This work focuses on the kinesin-3 family, which contains five main subfamilies: KIF1, KIF13, KIF14, KIF16, and KIF28, as well as a sixth member of short kinesin-3-like proteins in fungi (Fuchs & Westermann, 2005; Miki et al., 2005). Kinesin-3 motor's have distinct motor domains, containing a family-specific K-loop that sits at the microtubule surface. This charged loop is thought to contribute to kinesin-3's microtubule affinity, but does not fully explain its superprocessivity (Soppina et al., 2009). Mammals express at least eight different kinesin-3 family motor proteins, and this is likely due to each

Human kinesin-3 subfamily

KIF14
KIF16A
KIF16B
KIF13A
KIF13B
KIF1C
KIF1A
KIF1B

Kinesin superfamily
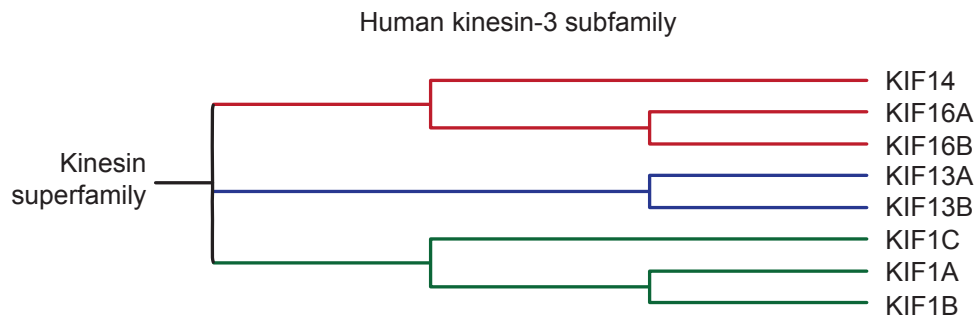
Figure 1.2: Human kinesin-3 family tree | Family tree generated from Clustal analysis of human kinesin-3 protein sequences. The kinesin-3 motors clearly separate into three groups based on sequence homology: the KIF14/16 group, KIF13 group, and KIF1 group.

being specific to different subsets of cargoes.(Siddiqui & Straube, 2017) A list of kinesin-3 motors and their respective cargoes and cell types has been reproduced from Siddiqui and Straube (2017) and is shown in Table 1.1. In humans, kinesin-3s further subdivide into three groups based on their sequence similarity (see Figure 1.2).

In order for kinesin-3 motor proteins to become active transporters, they need to dimerise and any autoinhibition must be relieved. The members of the kinesin-3 family are thought to be regulated either at the monomer-to-dimer transition, or by autoinhibitory mechanisms, but dissecting the exact mechanism is difficult (see Figure 1.3). For example, endogenous KIF1A appears to be a monomer, whereas recombinant full-length KIF1A is a dimer that shows some limited motility *in vitro* (Chiba et al., 2019; Rashid et al., 2005). Meanwhile, endogenous KIF13A is reported to be a dimer while full-length recombinant KIF13A appears to be a monomer (Nakagawa et al., 2000). Later it was shown that the motor domain of KIF13A can be dimerised in the presence of Rab22A and so it seems that KIF13A likely undergoes cargo-mediated dimerisation to become fully active (Patel et al., 2021). Full-length recombinant KIF1C constitutively forms dimers and these dimers are autoinhibited by interactions between the motor and stalk domains of the kinesin which can be relieved by activating proteins (Kendrick et al., 2019; Siddiqui et al., 2019). These examples act to illustrate the difficulty of determining the exact mechanism of activation for these kinesins. While expression and purification of full-length kinesins is challenging, research focused on short truncations of kinesin-3 motor domains that have been artificially dimerised may fail to re-

6

Motor	Cargo	Cell type	Reference
KIF1A	tyrosine kinase A receptor (TrkA)	mouse dorsal root ganglion neurons	Tanaka et al. (2016)
	synaptotagmin and synaptophysin	rat spinal nerves (cauda equina)	Okada et al. (1995)
	dense core vesicles (DCVs)	rat primary hippocampal neurons	Lo et al. (2011)
	beta secretase-1 (BACE-1)	mouse SCG neurons	Hung and Coleman (2016)
	AMPA receptors	rat brain	Shin et al. (2003)
KIF1B	mitochondria	mouse Neuro2a cells	Nangaku et al. (1994)
	SCG10 / Stathmin-2	sensory axons in zebrafish	Drerup et al. (2016)
	lysosomes	Cos7 African green monkey fibroblast cells	Matsushita et al. (2004)
KIF1C	α5β1-integrin	RPE1 human epithelial cell line	Theisen et al. (2012)
	neuropeptide-containing dense core vesicles	rat primary hippocampal neurons	Lipka et al. (2016)
	brain-derived neurotrophic factor-containing dense core vesicles	rat primary hippocampal neurons	Lipka et al. (2016)
KIF13A	serotonin type 1A receptor	mouse hippocampal neurons	Zhou et al. (2013)
	viral matrix proteins	Huh7 human hepatoma cell line	Fehling et al. (2013)
	mannose-6-phosphate receptors (MPRs)	MDCK canine epithelial cell line	Nakagawa et al. (2000)
	FYVE-CENT	HeLa human cervical cancer cell line	Sagona et al. (2010)
KIF13B	human discs large (hDlg) tumor suppressor	in vitro reconstitution with purified human KIF13B	Yamada et al. (2007)
	PtdIns(3,4,5)P3-containing vesicles	rat PC12 cells and in vitro reconstitution	Horiguchi et al. (2006)
	vascular endothelial growth factor receptor 2 (VEGFR2)	human umbilical vein endothelial cells(HUVECs)	Yamada et al. (2014)
	transient receptor potential vanilloid 1(TRPV1)	CHO cells, rat dorsal root ganglion neurons	Xing et al. (2012)
KIF16B	fibroblast growth factor receptor (FGFR)	mouse embryonic stem cells	Ueno et al. (2011)

Table 1.1: **Mammalian kinesin-3 motors and their associated cargoes |** A summary of mammalian kinesin-3 motors and their associated cargoes, reproduced from Siddiqui and Straube (2017) with additions.

Active dimeric kinesin

Non-processive
monomeric kinesin

Autoinhibited dimeric
kinesin

Monomer-to-dimer switch
1 Kinesin activation:
Rab-scaffolded dimerisation
Organelle local enrichment dimerisation

2 Kinesin deactivation:
Neck-coil locking mechanisms
Phosphorylation
Coiled-coil/neck linker interactions

Autoinhibition release
3 Kinesin activation:
Cargo adaptor-scaffolding
Post-translational regulation?

4 Kinesin deactivation:
Intra/inter-molecular interactions
Post-translational regulation?

Figure 1.3: Activation of kinesin-3 motors | Kinesin-3s are thought to switch between active and inactive states either through a monomer-to-dimer switch mechanism (1 and 2), or through switching on and off autoinhibition (3 and 4). Some of the suggested and investigated mechanisms for this are listed, corresponding to following references. (Hammond et al., 2009; Patel et al., 2021; Siddiqui et al., 2019; Soppina & Verhey, 2014)

capitulate the full complexity of the motor (Budaitis et al., 2021), but even full-length motors may require accessory factors to become activated. Thus a mechanistic view of a kinesin's activation is best achieved by determining its protein-protein interactions and reconstituting transport *in vitro* with full-length purified motors and accessory factors.

Kinesin-3 motor proteins, especially those of the KIF1 subfamily, are amongst the fastest and most processive kinesins inside cells (Lipka et al., 2016; Schlager et al., 2010), and the transport they provide is essential for life (Schlager et al., 2010). Indeed, familial mutations in KIF1A and KIF1C lead to hereditary spastic paraplegia and this is thought to arise due to increased, decreased, or slower transport of organelles along neurons (Dor et al., 2014; Gabrych et al., 2019; Oteyza et al., 2014; Pennings et al., 2020; Yücel-Yılmaz et al., 2018). As such, study of hereditary mutations in KIF1A are of keen in-
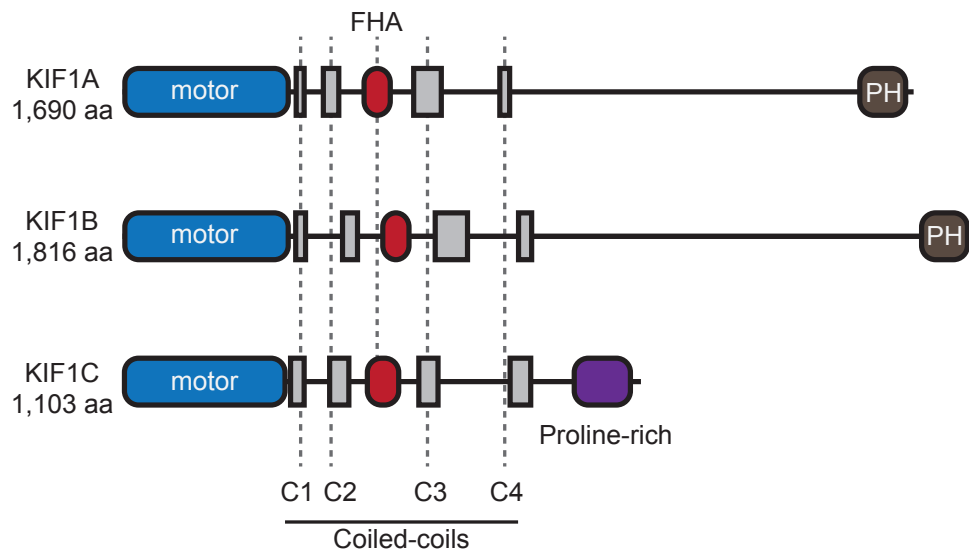
Figure 1.4: KIF1 kinesin-3 motors | Schematics of KIF1A-C motors, showing that they share similarities, such as nearly identical motor domains, the presence of 4 regions of coiled-coil structure, and a FHA domain. KIF1A and B differ from KIF1C by having a pleckstrin-homology domain at the very C-terminus, while KIF1C instead has a proline-rich region. The alignment of coiled-coils/FHA domains is shown by a dashed line based on the position within KIF1A.

terest in finding potential therapeutic routes to alleviate neurological issues in KIF1A patients (Chiba et al., 2019), and hyperactivating KIF1A or KIF1C proteins with activating factors could be one method (Siddiqui et al., 2019). KIF1 motors share many similarities, including near identical motor domains, the presence of an FHA domain, and the presence of four short coiled-coil regions (see Figure 1.4). KIF1C does not contain a C-terminal pleckstrin-homology domain, while KIF1A and KIF1B do, and this may allow them to bind directly to lipid cargoes (Klopfenstein & Vale, 2004). Overall, the spacing between coiled coils, as well as the size of the proteins, differs between different KIF1 proteins and this likely points to each motor having their own set of cargo interactors and regulation mechanisms.

Taken together this literature illustrates how although there are many kinesins, and sequence homology between kinesin members is high, the exact cargoes and mechanisms of activation of these kinesins is diverse. Kinesins are not functionally redundant, and mutations that damage the ability of kinesin-3s to transport cargoes, or prevent their expression, can cause severe disease.
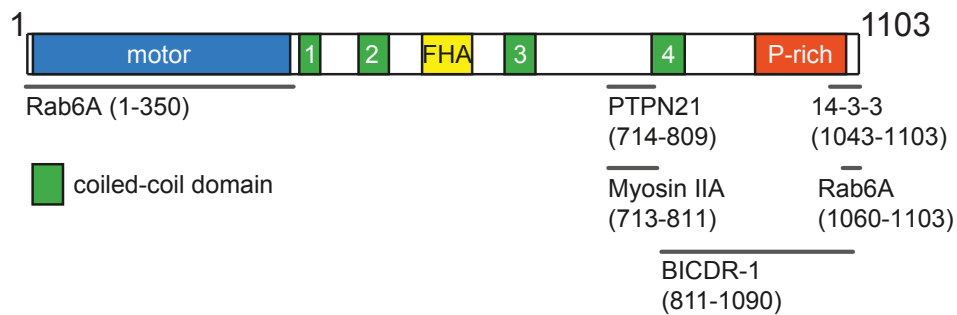
Figure 1.5: KIF1C structure and interactors | KIF1C has a number of known interactors, both with the motor domain and with the C-terminal portion of the protein. These interactors correspond to the following published works: Dorner et al. (1998), Dorner et al. (1999), Kopp et al. (2006), and P. L. Lee et al. (2015), Schlager et al. (2010).

In this work, we will focus on the kinesin-3 KIF1C, which has been established as an important neuronal transporter that traffics neuropeptide-containing dense core vesicles (Lipka et al., 2016; Schlager et al., 2010). KIF1C is known to interact with a number of proteins (summarised in Figure 1.5). Rab6A is reported to regulate KIF1C motor's accessibility to the microtubule, while also binding to the C-terminus of the kinesin to link it to cargo transport (P. L. Lee et al., 2015).The stalk domain of KIF1C binds to the phosphatase PTPN21, and in doing so the kinesin's autoinhibition is relieved (Dorner et al., 1998; Siddiqui et al., 2019). Interaction of PTPN21, BICDR1 and yet uncharacterised cargo adaptors in the stalk region of the kinesin may link it to cargoes (Schlager et al., 2010). The binding of 14-3-3 proteins to the C-terminus of KIF1C points to a possible phosphoregulation of its intracellular activities (Dorner et al., 1999). Myosin IIa is important in KIF1C's role in podosome formation (Kopp et al., 2006). In summary, KIF1C is an interesting motor owing to its described importance in hereditary spastic paraplegia, its fast speed and high processivity in intracellular transport, and for its interaction with cargo adaptor proteins, some of which are also dynein adaptors.

1.3   Cytoplasmic dynein's mechanism of activation

Dynein is a large AAA ATPase, which transports cargoes towards the minus-ends of microtubules. Dynein exists as two main types: axonemal and cyto-

plasmic. Axonemal dynein slides microtubules within cilia, while cytoplasmic dynein is a general purpose motor used for intracellular transport of cargoes and intraflagellar transport in cilia and flagella (Roberts et al., 2013).

Cytoplasmic dynein is a huge molecular assembly consisting of a pair of dynein heavy chains brought together by a number of intermediate, light-intermediate and light chains, and the full dynein holoenzyme is around 1.25-1.5 MDa in size. There are two dynein heavy chain genes, DYNC1H1 and DYNC2H1, which encode cytoplasmic dynein-1 and dynein-2 respectively. Dynein-2 and dynein-1 form distinct complexes with different accessory chains, and these chains have functional significance on the behaviour of the complex (Vuolo et al., 2018). Dynein-2 complexes are thought to almost exclusively undertake intraflagellar transport together with kinesin-2, delivering to and retrieving cargoes from the ciliary tip to support their growth and maintenance (Vuolo et al., 2018). Dynein-1 undertakes the majority of minus-end directed intracellular transport within the cell and is the dynein motor of interest in this work.

Dynein-1 (herein referred to as "dynein") is a dimer of two dynein heavy chains that are brought together by its N-terminal dimerisation domain, and this dimerisation is reinforced along the length of the N-terminal region by the intermediate and light-intermediate chains (cytoplasmic dynein 1 intermediate chain 2 (IC2C) and cytoplasmic dynein 1 light intermediate chain 2 (DLIC2)). The light chains Rob1, TCTEX and LC8, bind to the N-terminus of the intermediate chains (K. Zhang et al., 2017). Purified wildtype dynein complex shows a primarily autoinhibited phi-particle conformation, where the heavy chains stack and the stalks of the two dynein motors are crossed keeping the microtubule binding domains in an orientation that impedes productive engagement with microtubules (K. Zhang et al., 2017). Forced separation of the dynein heavy chains is known to allow activation of the motor and processive transport along microtubules (Torisawa et al., 2014). Activation of wildtype dynein was found to occur through a two-step process. First, closed phi-particle dynein must be opened by breaking the interaction between the pair of motor domains, and second, the motor domains must be constrained in an orientation where the stalks of the two dynein heavy chains are parallel (Chowdhury et al., 2015; K. Zhang et al., 2017) (see Figure 1.6). Dyneins can be arranged in this way through complex formation with their obligate cofactors dynactin and dynein-adaptor proteins, and this results in dynein complexes that are highly processive undertaking long-range and rapid transport

11
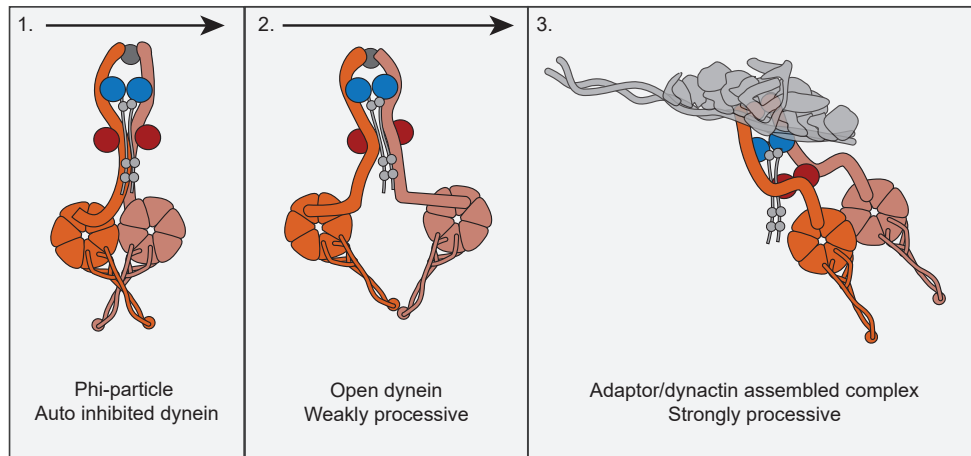
Figure 1.6: Activation of dynein | 1. Dynein is autoinhibited in a form that impedes its interaction with microtubules. The so-called phi-particle is stabilised by interactions of the heavy chain at the ATPase domains, as well as at the stalk. The long extended tail is brought together by dynein's N-terminal dimerisation domain, and the action of light and light-intermediate chains. **2.** In order to begin activation, the phi-particle must be opened to separate the motor domains. In this conformation, dynein can undertake weakly processive movement on microtubules. **3.** The open conformation allows complex formation with dynactin and dynein adaptors, which reorient the dynein heavy chains to be parallel and able to undertake coordinated processive transport. Figure adapted from K. Zhang et al. (2017).

in vitro.

Dynactin itself is a 23-subunit 1 MDa complex built on a ~37 nm long actin-like filament, and is essential for many of dynein's functions (Chowdhury et al., 2015; Urnavicius et al., 2015). Dynactin acts to scaffold the dynein molecules in a parallel orientation with the help of dynein adaptors, and this organisation allows maximal processive movement of dynein-dynactin-adaptor complexes (Chowdhury et al., 2015; McKenney et al., 2014; Urnavicius et al., 2015; K. Zhang et al., 2017). Dynein adaptors are discussed separately in the next section, however, dynactin alone has dynein-independent microtubule binding activity through the CAP-Gly domain of p150(Glued) which is a long and flexible protein attached to the barbed end of dynactin. p150(Glued) is recruited to the plus-ends of microtubules by CLIP-170 which is in turn recruited by EB1, and recruitment of dynactin to the plus-end of microtubules appears to lead to recruitment of dynein (Duellberg et al., 2014; Watson & Stephens, 2006). Interaction of p150(Glued)'s CAP-Gly domain directly with

the microtubule has been shown to be dependent on the tyrosination of α-tubulin, and it seems that p150(Glued)'s recruitment of dynein complexes to the microtubule may be one of the main ways in which processive motility is initiated (McKenney et al., 2016). The p150(Glued) subunit has been found to increase the motility of dynein, and it was thought that the microtubule-binding activity of p150(Glued) allowed it to act as a processivity factor (King & Schroer, 2000). However, dynactin's effect in increasing the processivity of dynein is independent of p150(Glued)'s microtubule-binding ability for yeast dynein-dynactin complexes (Kardon et al., 2009). Consistent with this, mammalian dynein-dynactin-BICD2 complexes appear to undertake more diffuse movement when the p150(Glued)-to-microtubule interaction is prevented with antibody binding, suggesting that p150(Glued)'s primary operation is not as a microtubule processivity tether, but rather that it is probably contributing to structural organisation of the dyneins (Feng et al., 2020). Thus as well as acting as a scaffold, dynactin is able to localise dynein and define the starting point of dynein's motility.

Dynein adaptors, specifically Bicaudal D (BICD), were discovered in *Drosophila* over thirty years ago (Wharton & Struhl, 1989) and their roles in tethering cargoes to dynein and promoting dynein activation had later been found *in vivo* (Bullock & Ish-Horowicz, 2001; Liu et al., 2013). Mammalian homologues of BICD such as Bicaudal D homolog 2 (BICD2) and Bicaudal D-related protein 1 (BICDR1) were identified, and found to link dynein to cargoes as well as activate minus-end directed transport, although the exact mechanism of this activation was unclear (Hoogenraad et al., 2001; Schlager et al., 2010). Processive dynein-dynactin-adaptor complexes were reconstituted *in vitro* by several labs using either recombinant dynein, dynein/dynactin which had been purified from brains, or by using dynein adaptors as a bait to recruit dynein/dynactin from lysates (Chowdhury et al., 2015; McKenney et al., 2014; Schlager et al., 2014; Urnavicius et al., 2015), and this revealed the essential role of dynein adaptors in converting weakly processive individual dynein molecules to processive dynein complexes in the presence of dynactin. The arrangement of the full dynein, dynactin and BICD2 complex bound to the microtubule was shown using complexes made from native bovine-brain purified dynein and dynactin with recombinant BICD2(25-400) (Chowdhury et al., 2015), showing how dynein's heavy chains interact with the microtubule in a way that primes them for unidirectional movement. Higher resolution studies showed the recruitment of two dynein dimers within the complex while it is

13

Adaptor	Cargoes	Dynein motility	Potential kinesin(s)	Evidence for kinesin interaction	References
Spindly	RZZ complex	Reconstituted from lysate	CENP-E	Hypothesised	(Howell et al., 2001; McKenney et al., 2014)
BICD1	Nucleus, Rab3 vesicles	Transport in zebrafish axons	Kinesin-1 family, KIF27, KIF7, Kif1bβ	Localised to nuclear pore complexes in C. elegans, controls nuclear positioning. Kif1bβ -binding through Fignl1 in zebrafish.	(Atkins et al., 2019; Fridolfsson et al., 2010; Redwine et al., 2017)
BICDR1	Rab6a vesicles	Reconstituted in vitro	KIF1C	Yeast two-hybrid interaction.	(Schlager et al., 2010; Urnavicius et al., 2017; Urnavicius et al., 2015)
BICD2	Golgi vesicles	Reconstituted in vitro	KIF7, KIF1C, KIF5B	Localised to nuclear pore complexes in HeLa cells, controls nuclear positioning. Co-IP between KIF1C and BICD2	(Hoogenraad et al., 2001; Redwine et al., 2017; Splinter et al., 2010)
Ninein	?	Reconstituted in vitro	KIF14, KIF7	Bidirectional movement along microtubules in cells. Proximity based labelling in BioID experiment.	(Moss et al., 2007; Redwine et al., 2017)
Ninein Like	?	Reconstituted in vitro	CENP-E, KIF7, KIF14, KIF5A, KIF1B	Proximity based labelling in BioID experiment.	(Redwine et al., 2017)
Hook1	Rab5a early endosomes, Clathrin-independent cargoes	Peroxisome retargetting assay	KIF5C, KIF1C	Proximity based labelling in BioID experiment. KIF1C:Hook1 binding later disproven by Co-IP.	(X. Guo et al., 2016; Kendrick et al., 2019; Olenick et al., 2016; Redwine et al., 2017)
Hook3	Rab5a early endosomes, Golgi	Reconstituted in vitro, and from lysate.	KIF1C	Proximity based labelling in BioID experiment. In vitro reconstitution.	(Kendrick et al., 2019; Maldonado-Báez et al., 2013; McKenney et al., 2014; Redwine et al., 2017; Siddiqui et al., 2019; Urnavicius et al., 2015)
TRAK1	Mitochondria	Co-IP & peroxisome re-targetting assay	KIF5B	Interact with both KIF5B and dynein/dynactin in Co-IP. Reconstituted motility with KIF5B.	(Henrichs et al., 2020; van Spronsen et al., 2013)
TRAK2	Mitchondria	Co-IP & peroxisome re-targetting assay	KIF5B	Interact with both KIF5B and dynein/dynactin in Co-IP.	(van Spronsen et al., 2013)

Table 1.2: **Dynein adaptors and their potential kinesin interactors |** A selection of dynein adaptors and their potential kinesin interactors present in the literature. Partially based on Reck-Peterson et al. (2018).

attached to microtubules, and showed how the four dynein motor domains stack parallel to one another (Grotjahn et al., 2018). Separately, a structural analysis of complexes made with dynactin, dynein-adaptors and dynein tail complex revealed how the two dynein dimers bind at two distinct sites along dynactin: one binding roughly half way between the barbed and pointed end of dynactin, and the second close to the barbed end of dynactin (K. Zhang et al., 2017). Dynein adaptors have diverse primary sequences, but share the structural characteristic of having one or more long coiled-coil domains. These coiled coils have been shown to sit at the interface between dynein and dynactin to allow their assembly (Chowdhury et al., 2015; K. Zhang et al., 2017). The exact binding location of these coiled coils along dynactin's surface differs between adaptor proteins, and that explains why some adaptors are better able to recruit two dynein dimers (e.g. Hook3 and BICDR1), while others primarily recruit one dynein dimer to the complex (e.g. BICD2) (Urnavicius et al., 2018). Two-dynein complexes achieve faster velocities and produce more force (Htet et al., 2020; Urnavicius et al., 2018).

Alongside their role in permitting dynein-dynactin complex formation, dynein adaptors also specify dynein to different cargoes. For example, BICD2 transports Golgi-derived vesicles (Hoogenraad et al., 2001), BICDR1 transports Rab6 vesicles (Schlager et al., 2010), while Hook1 and Hook3 transport Rab5a marked early endosomes (X. Guo et al., 2016). There are numerous dynein adaptors and more continue to be identified. Interestingly, many dynein adaptors also have evidence in the literature for kinesin-based motility: this evidence comes from bidirectional motility of cargoes observed in cells and *in vivo*, as well as a comprehensive proximity-based labelling experiment performed by Redwine and colleagues (Redwine et al., 2017). A selection of dynein adaptors, their potential kinesin interactors and the evidence for such interactions is listed in Table 1.2. Taken together with the fact that dynein adaptors differentially control the stoichiometry of the dynein/dynactin/adaptor complexes by recruiting one or two dynein dimers, cargo adaptors may act within cells to recruit either one-dynein complexes, which have fast velocity and considerable load bearing capacities (e.g. 850 nm/s and 3.7 pN stall force for dynein-dynactin-BICD2), or can instead recruit two-dynein complexes which have extremely high velocity and can produce even higher forces (1350 nm/s and 6.5 pN for dynein-dynactin-BICDR1)(Urnavicius et al., 2018).

Dynein is additionally regulated by the actions of a small protein called Lissencephaly-1 (Lis1). Lis1 is required for dynein dependent organelle posi-

tioning (Lam et al., 2010) and *in vitro* has been found to decrease the ATPase rate of isolated dyneins by sterically blocking their ATPase cycle (Huang et al., 2012; Toropova et al., 2014). Lis1 binds to two regions of dynein's triple-A domains, and the number of Lis1 molecules bound depends on the nucleotide state of AAA3. When a single Lis1 molecule is bound, dynein is in a strong microtubule binding state, whereas binding of two Lis1 molecules promotes a weak bound state, and it is proposed that each state would have different load-bearing properties (DeSantis et al., 2017). Lis1 is also able to increase the idle time of dynein motors at the plus-ends of microtubules in the presence of EB1, perhaps acting to allow the loading of cargoes before transport begins (Baumbach et al., 2017). However, when dynein is in complex with dynactin and a cargo adaptor, Lis1 increases the velocity and run length of dynein complexes (Baumbach et al., 2017; Gutierrez et al., 2017), and this is explained by Lis1 favouring the formation of complexes containing two dynein dimers (Htet et al., 2020). Importantly, Lis1 co-migration isn't required for the increase in velocity and run length (Htet et al., 2020). Therefore it seems that Lis1 acts to keep dynein in a ready state, either at the microtubule or in solution, perhaps to allow time for loading of dynein adaptors, dynactin and cargoes in order to create the fully activated processive two-dynein containing complex. Once formed, the dissociation of Lis1 releases dynein from the starting blocks, allowing it to undertake its fast processive runs.

However, not all functions of dynein appear to require the action of dynactin and dynein adaptor proteins (Raaijmakers et al., 2013). Research from our lab has shown that parallel organisation of microtubules can also promote processive movements of dynein, in the absence of dynactin and cargo adaptors (Chakraborty et al., 2020). Thus the separated tracks of two microtubules could provide another method to make dynein heavy chains more parallel and therefore more able to undertake processive movement. Activation of dynein in this way may be sufficient to allow it to perform its alternative role as a microtubule organiser (del Castillo et al., 2015; Mogessie et al., 2015).

1.4 Bidirectional intracellular transport arises from the interplay between dynein and kinesin

The textbook understanding of motor-driven transport is that kinesin provides plus-end directed transport while dynein is the sole minus-end directed trans-

porter. This idea was challenged when the kinesin-14 family members were characterised, which also undertake minus-end directed transport (McDonald et al., 1990; Walker et al., 1990). Furthermore, some kinesin members specialise their ATP hydrolysis towards tasks other than microtubule translocation, such as the kinesin-13 MCAK which is a potent microtubule depolymeriser (Friel & Howard, 2011; Wordeman & Mitchison, 1995). It is increasingly becoming understood that kinesin operation is also context specific. Microtubule crowding can drive kinesins to change their direction in certain situations,(Britto et al., 2016; Conway & Ross, 2014) and kinesin is also able to direct conformational changes in the microtubule lattice that stabilise it, though the consequences of this for intracellular transport are not yet understood (Peet et al., 2018).

In the simplest view of intracellular transport, these motors get recruited onto cargo, run along microtubule tracks carrying the cargo, drop the cargo off at the end of the track and redistribute through diffusion. This has been observed to be true in certain cases, both experimentally and through mathematical modelling (Blasius et al., 2013). Inconsistent with this, are observations by us and others that opposite polarity motors rely on one another: depleting a plus-end directed motor is sufficient to perturb minus-end directed transport (Theisen et al., 2012). This remains paradoxical as if one motor is abrogated, it would be expected that cargoes would be more often observed travelling in the opposite direction. However, Ciliobrevin D inhibition of dynein reduces transport of organelles in both plus-end and minus-end directions,(Sainath & Gallo, 2015) and similar results are observed from antibody inhibition of the dynactin p150 subunit (Waterman-Storer et al., 1997). The fact that dynein inhibition leads to defects in kinesin-driven transport reveals how these two motors are functionally interlinked, and suggest that motor turnover isn't achieved solely by diffusion. Indeed, even in small eukaryotic cell types such as *Aspergillus nidulans*, dynein and dynactin appear to be actively trafficked to the plus-end of microtubules by the actions of kinesin (J. Zhang et al., 2003). One of the clearest examples of how dynein and kinesin can be linked comes from intraflagellar transport, where kinesin-2 transports packages of ciliary cargoes and autoinhibited dynein-2 along microtubules to the tip of the cilium, where packages are disassembled and dynein-2 becomes activated such that it can return itself and kinesin-2 towards the cell body (Vuolo et al., 2018; Vuolo et al., 2020).

There is also evidence that kinesin-driven motion might activate dynein

transport, as depletion of kinesin-1 leads to decreased dynein-based transport of peroxisomes, but replacement of kinesin-1 with kinesin-3 or kinesin-11 members attached to peroxisomes is sufficient to restore dynein motility and allow cargoes to move bidirectionally (Ally et al., 2009). The ability of these motors to generate force is essential for this effect, and so it is the opposing force itself which is thought to activate the motors (Ally et al., 2009). Consistent with this, in *Drosophila* it was found that the kinesin-3 UNC-104 is responsible for the rapid anterograde transport of dense core vesicles (DCVs), but crucially, mutations in UNC-104 inhibited retrograde (i.e. dynein-dynactin driven) transport, and this effect is not caused by a decrease in dynein concentration in the distal parts of the axon (Barkus et al., 2008). Similarly, when retrograde transport by dynein is decreased by the depletion of NudE/L, lysosomes appear to undertake more bidirectional movement (Yi et al., 2011). However, when dynein is acutely inhibited by injection of NudE/L antibodies, lysosomes appear to undertake slower transport and directional switches (Yi et al., 2011).

Why do cargoes undertake bidirectional movements, is this not a less efficient mode of transport than unidirectional motion? It has been suggested that this bidirectional motion could allow cargoes to explore intracellular space more efficiently, so that they can find their destination more readily (Ally et al., 2009). In intraflagellar transport as previously described, dynein-2 would not be able to get to the ciliary tip without the action of kinesin-2, and kinesin-2 may accumulate in the tip if not for the action of dynein-2 returning it (Vuolo et al., 2018). The same polarised distribution of motors enacts itself on a much larger scale in neurones, where kinesin-1 aids delivery of dynein to the tips of axons (A. E. E. Twelvetrees et al., 2016). Bidirectional transport may also be a mechanism of overcoming obstacles along the microtubule, as individual kinesin-1 motors aren't able to switch protofilaments, and so dissociate from the microtubule when meeting obstacles (Crevel et al., 2004; Telley et al., 2009), but paired with dynein's ability to side-step, a mechanism whereby cargoes can reverse and re-approach on a different protofilament could be hypothesised (Ferro et al., 2019). Microtubule-microtubule intersections present another possible obstacle whereby cargo-laden motors have their motion restricted, as around 50% of lysosomes will pause when approaching an intersection (Bálint et al., 2013). Around 20% of these paused cargoes go on to reverse away from the intersection, while 40% switch to different microtubules (Bálint et al., 2013). This behaviour has also been reconstituted *in*

vitro for bead cargoes, where beads pause at microtubule intersections in a manner that is dependent to the amount of dynein bound to them (Ross et al., 2008). Thus bidirectional transport likely acts as a mechanism to allow robust transport inside cells, and is not an artifact of brief moments of dynein and kinesin opposing one another.

Despite the wealth of evidence showing bidirectional transport, and how it relies on kinesin and dynein functionality, mechanistic understanding of how it is achieved at the single-motor level is still lacking. One idea is that the motors may undertake a tug-of-war. Lipid cargoes, such as vesicles, are able to recruit opposite polarity motors and this is thought to allow a tug-of-war to occur. Estimates for numbers of plus-end directed kinesins versus minus-end directed dyneins vary in the literature, in the range of 1-20 each (Hendricks et al., 2010; Rai et al., 2013). However, these estimations rely on an assumption of the force output of individual motors. In their 2013 paper, Rai *et al.* work on the assumption that dynein outputs between 0-2pN of force, and attribute the 6-8pN force observed inside of cells to the possibility that dyneins work as teams and their collective force is summed (Rai et al., 2013). Contrary to this, optical tweezer experiments using single dynein/dynactin/adapter complexes *in vitro* yield values in the range of 4.0-4.3pN for dynein-dynactin-BICD2 and 6.5pN for dynein-dynactin-BICDR1, which would make dynein a competitive match for a single kinesin-1 whose force output is between 5-6 pN (Belyy et al., 2017; Carter & Cross, 2005; Svoboda et al., 1993; Urnavicius et al., 2017). Directly tethering dynein to kinesin does not reconstitute bidirectional transport but instead results in a tug-of-war where motors move towards either the plus- or minus- end at decreased velocities (Belyy et al., 2017; Derr et al., 2012).

Many models are still centred around the tug-of-war principle, and it is inconceivable that this doesn't occur at least to some extent inside cells, and may indeed be important for organelle positioning (Hancock, 2014; Hendricks et al., 2010). Different ideas for how bidirectional cargo transport may occur are presented in Figure 1.7. A tug-of-war mechanism whereby the number of kinesins vs. dyneins determine the directional force and overall direction of cargoes is hypothesised (see Figure 1.7 a.). One could imagine that given the number of motors interacting with the microtubule from lipid cargoes is supposed to be only a fraction of their total motors (Jiang et al., 2019), perhaps kinesin and dynein alternate in providing cargo motility (see Figure 1.7 b.). In opposition to the tug-of-war theory, it is now becoming increasingly

a.

Tug-of-war

Plus-end

Minus-end

Motors oppose each other, and the number of motors or their cumulative force dictates directionality.

b.

Alternate interaction

Plus-end

Minus-end

Motors interact with the microtubule in distinct phases, and stop when both motor-types are engaged.

c.

Bidirectional complex

Plus-end

Minus-end

Motors form a unified complex of dynein and kinesin that regulates forwards and backwards motion.

Figure 1.7: Models of bidirectional transport | a. Bidirectional transport could occur through a tug-of-war, where the number of kinesins or dyneins or their collective force output determine the direction of transport. In this schematic, three kinesins win the tug of war and transport the cargo towards the plus-end. **b.** Cargoes could be seen to go bidirectionally when the motors that engage with the microtubule alternate, for example, dynein could not make contact with the microtubule allowing kinesin to undertake transport. **c.** Direct complexes of kinesin and dynein could form, and these could regulate themselves to undertake bidirectional transport.

recognised that kinesins can bind to dynein cargo adaptors too, as described previously. This raises the possibility that a bidirectional complex may form between kinesin, dynein and their shared adaptor proteins, and this could be subject to chemical or conformational regulation to avoid a tug-of-war and promote rapid transport of intracellular cargoes (see Figure 1.7 c.).

In summary, bidirectional transport is an important mechanism for cellular cargoes to achieve correct organelle positioning, to maintain the correct distribution of motor proteins, and to avoid obstacles along the microtubule. Mechanistic insight into how motors undertake bidirectional transport is lacking, and the current models are that either the kinesin and dynein undertake a tug of war to determine overall directionality, or there exists a method by which the two motors are coordinated. The kinesin-3 KIF1C is an attractive candidate motor protein for linking dynein and kinesin transport directly, as it is reported to bind to the dynein adaptors BICD2, BICDR1 and Hook3. In this work, we will first study the mechanism of activation of the KIF1C. We will aim to confirm which dynein adaptors interact with KIF1C and what functional consequence this has on KIF1C's activation. Inside cells we will investigate how the balance of KIF1C and dynein-driven transport alters directionality on short timescales. Using purified KIF1C, dynein, dynactin and dynein adaptors, we will attempt to reconstitute a bidirectional complex of KIF1C and dynein, and investigate whether such an arrangement is beneficial to these motors as the theory of motor co-dependence would predict.

Chapter 2

Materials and Methods

2.1 Cloning

2.1.1 Restriction enzyme based cloning

Digestion

All restriction enzymes were purchased from NEB. Typically, 2-4 μg of plasmid DNA was digested using 10-20 units of the relevant restriction enzymes in a total volume of 50 μl of the NEB buffer which maximised enzyme activity. The digestion occurred overnight at 37 °C, except in special cases where enzymes required different temperatures or incubation times. Digested DNA was separated on 1% agarose gels in TAE (40 mM Tris, 20 mM acetic acid, 1mM EDTA) and visualised with SafeView Nucleic Acid Stain (NBS Bio, #NBS-SV1). Correctly digested bands were purified as detailed below.

Ligation

DNA fragments were ligated in a 1:3 molar ratio of backbone:insert in a total volume of 10 μl containing 2μl 5X Rapid Ligation Buffer (Thermo Scientific, #K1422) using 5 units of T4 DNA ligase (Thermo Scientific, #10723941). After assembly, the ligation reaction was incubated for 15 minutes at room temperature, and the entire amount was transformed into TOP10 competent cells.

2.1.2 Gibson assembly

Gibson assembly was performed with a homemade 2X master mix (see Table 2.1). Typically, 5 μl of 2X master mix was added to 5 μl of mixed DNA

fragments, the reaction was incubated at 50 °C for 50 minutes, and the entire amount was transformed into TOP10 competent cells.

Final concentration for 2X	[Stock]	Dilution	Amount for 250 µl
2X Isothermal Reaction Buffer	5X	2:5	100µl
0.008 U/µl T5 Exonuclease (NEB, #M0363S)	10U/µl	1:1250	0.2µl
0.050 U/µl Phusion polymerase (NEB, #M0530S)	2U/µl	1:40	6.25µl
8U/µl TAQ Ligase (NEB, #M0208S)	40U/µl	1:5	50µl
Nuclease Free Water			to 250µl (93.55µl)

Table 2.1: 2X Gibson master mix recipe

Final concentration for 5X	[Stock]	Dilution	Amount for 1ml
500mM Tris pH 7.5	1M	1:2	500µl
50mM MgCl2	1M	1:20	50µl
1mM dNTPs (Sigma, #D7295)	10mM mix	1:10	100µl
50mM DTT (Sigma)	1M	1:20	50µl
5mM NAD+ (NEB, #B9007S)	50mM (NEB)	1:10	100µl
25% PEG-8000 (Sigma, #81268)	powder		0.25g
Nuclease free water			to 1ml (∼200µl)

Table 2.2: 5X Isothermal Reaction Buffer

2.1.3 PCR

PCR was performed using Q5 High-Fidelity DNA Polymerase (NEB, M0491L). Reactions were prepared in a 50 µl volume with 10 µl 5X Q5 reaction buffer, 1 µl of 10 mM mixed dNTPs (Merck, D7295), 2.5 µl of each forward and reverse primer diluted to 10 µM (IDT), 1-10 ng of template DNA and 0.5 µl (2 U/µl) Q5 DNA polymerase. This represents a final concentration of 200 µM dNTPs, 0.5 µM of forward/reverse primers, and 0.02 U/µl Q5 DNA polymerase. Initial denaturing was performed at 98 °C for 30 seconds, then 32 cycles of denaturing, annealing and elongation were performed. The denaturing time was 10 s at 98 °C, annealing was performed for 15 s at temperatures determined by the oligo's composition, and elongation was performed for 30 seconds per kb at 72 °C. A final extension phase of 5 minutes at 72 °C was performed.

2.1.4   DNA extraction and purification

For extraction of DNA, either from agarose gels, from PCR, or small-scale plasmid purification from 2 ml bacterial cultures, kits from NBS Biologicals were used (#BS654, #BS664 and #BS614 respectively).

For large-scale purification of transfection-grade plasmid DNA from bacteria, 50 ml cultures were grown in DYT with the relevant antibiotic and then purified using a column-based midiprep kit (Sigma, #NA0200).

2.1.5   Plasmids and cloning strategies

The following plasmids used in this study were described previously: pKIF1C^{RIP2}-GFP (Efimova et al., 2014), pNPY-RFP (Miller et al., 2009), and pFastBac_His-ZZ-TEV-Lis1 (Baumbach et al., 2017). pFastBac-M13-6His-KIF1C-GFP, pFastBac-M13-6His-KIF1CΔS-GFP, pFastBac-M13-8His-ZZ-LTLT-Hook3-SNAPf, pKan-CMV-Hook3-GFP, pKIF1C-BioID2-HA, pKIF1CΔS-BioID2-HA, motor-GFP (pET22b-KIF1C(1–349)-NTVSVN-GFP-6H) and GST-stalk (pGEX-6P2-LTLT-KIF1C(612–922)) were all described in Siddiqui et al. (2019).

All of the oligonucleotides created for use in this work are listed in Table 2.3.

KIF1C-Stalk-GFP

The GST-KIF1C-stalk-GFP (pET22b-GST-6P2-LTLT-KIF1C(612–922)-GFP) bacterial expression plasmid was created by opening pET22b-HsCLASP2-EBBD-eGFP-6His between the NdeI and SalI sites, and ligating in a PCR product of GST-stalk (previously described) formed between oligonucleotides AS 777 (NdeI-GST FWD) and AS 780 (SalI-KIF1C(922) REV).

shBICDR1, shBICD2 and shHook3

RNAi plasmids for Hook3, BICD2 and BICDR1 were made in pSuperNeoGFP (OligoEngine). Oligonucleotide sequences of validated small interfering RNAs (siRNAs) were taken from the following published works: Hook3 #1 from Herrmann et al. (2015), BICDR1 #88 from Schlager et al. (2010), and BICD2 #1 from Splinter et al. (2010). Pairs of oligonucleotides encoding the targeting sequence and sticky end overhangs for BglII/XhoI were synthesised and annealed (Hook3-1: AS 719 + AS 720; BICDR1-88: AS725 + AS 726;

24

BICD2-1: AS 723 + AS 724). These were ligated into pSuperNeoGFP plasmids linearised with BglII and XhoI to create the final shRNA construct.

BICDR1, BICD2 and Hook3

An insect expression vector for BICDR1 (pFastBacM13-ZZ-LTLT-BICDR1-SNAPf) was made by synthesising *Spodoptera frugiperda* (Sf9) codon-optimised DNA sequence of human BICDR-1 and attaching an N-terminal purification tag containing 8xHis, tandem protein-A binding motifs (ZZ) and tandem TEV recognition sites (LTLT; so called 8xHis-ZZ-LTLT). A SNAPf domain was synthesised at the C-terminal. This synthesised construct was digested with RsrII/NotI and ligated into pFastBacM13 vector cut with RsrII/NotI. A mammalian expression plasmid for BICDR1-GFP (pKan-CMV-BICDR1-GFP) was created by opening pKIF1C-GFP with EcoRI and BamHI. A PCR product of BICDR1 was made from the pFastBac plasmid between AS 667 (EcoRI-coSF-BICDR1-fw) and AS 638 (SNAPf rev), then this was digested with EcoRI and BamHI and ligated into the opened pKan backbone such that the BICDR1 replaced the KIF1C gene and inherited the GFP.

Hook3 and BICD2 were cloned from a human cDNA library by PCR using oligonucleotides which encoded a 5' AscI or EcoRI site and a 3' AgeI/BamHI site (oligonucleotides were AS 689, AS 691 and AS 693 for BICD2; AS 689, AS 690, AS 691 for Hook3). PCR products were cut with AscI/EcoRI at the 5' end and AgeI/BamHI at the 3' end. The AscI prepared versions were ligated into pFastBac-M13-8xHis-LTLT-BICDR1-SNAPf between the AscI and BamHI/AgeI sites, replacing BICDR1 and inheriting the SNAPf domain. The EcoRI prepared versions were ligated into pKIF1C-GFP replacing the KIF1C and inheriting the GFP. Thus the Hook3 and BICD2 insect expression vectors (pFastBac-M13-8xHis-ZZ-LTLT-Hook3-SNAPf and pFastBac-M13-8xHis-ZZ-LTLT-BICD2-SNAPf), and mammalian expression vectors (pKan-CMV-Hook3-GFP and pKan-CMV-BICD2-GFP) were created. An insect expression vector for Hook3 without a C-terminal tag was later produced with a PCR product created between AS 689 (AscI-Hook3 FWD) and AS 967 (NotI-STOP Hook3 REV) using pKan-CMV-Hook3-GFP as a template. This was cut with AscI/NotI and then inserted into pFastBac-M13-8xHis-ZZ-LTLT-Hook3-SNAPf replacing Hook3-SNAPf with Hook3 and creating pFastBac-M13-8xHis-ZZ-LTLT-Hook3. Inserts were sequenced to confirm the identity of the gene and to check for mutations.

DmrB inhibitable KIF1C

DmrB-Δ3-KIF1C-GFP was created by synthesising a region encoding DmrB-KIF1C(aa4-170) with an EcoRI site at the 5' end, and a BsiWI site at the 3' end. The linking region between DmrB and KIF1C's N-terminal was surrounded by SpeI and MluI sites to allow exchanging of the linker between the two domains. The synthesised DmrB-KIF1C(aa4-170) construct was cut with EcoRI and BsiWI, and then ligated into pKIF1C-GFP cut likewise, creating pKan-CMV-DmrB-Δ3-KIF1C-GFP. The linkers were then exchanged by synthesising pairs of oligonucleotides with complementary sticky overhangs for SpeI and MluI, which were annealed and then ligated into pKan-CMV-DmrB-Δ3-KIF1C-GFP that had been opened with SpeI and MluI. To create bicistronic vectors which expressed DmrB-KIF1Cs alongside short hairpin RNA (shRNA) targeting KIF1C, the entire DmrB-Δ1,2,3-KIF1C-GFP genes were cut from pKan backbones using NheI and Not, and then ligated into pSuperGFP-Tubulin-shKIF1C plasmid, replacing the GFP-Tubulin between NheI/NotI sites.

Hook3-FRB/Peroxisome assay plasmid

The C-terminal FRB peroxisome assay plasmid was constructed by synthesising a region of DNA encoding the FRB gene joined together with a P2A autocleavage signal peptide and the N-terminal 42 amino acids of Pex3. A number of unique restriction sites were included between the domains such that the synthesised construct was as follows: [AgeI-BamHI]-**FRB**-[PvuI]-**P2A**-[KpnI]-**Pex3(1-42)**-[AscI]-[SpeI-SalI-MfeI]. This synthesised construct was digested with BamHI and MfeI, and ligated into pKan-CMV-Hook3-GFP between BamHI and MfeI removing the GFP tag and stop codon and creating an intermediate plasmid pKan-CMV-Hook3-FRB-P2A-Pex3. tdTomato-FKBP was cut out of pBa-KIF5C 559-tdTomato-FKBP (Addgene #64211) between the AscI and SpeI sites, and was ligated into the pKan-CMV-Hook3-FRB-P2A-Pex3 plasmid to create pKan-CMV-Hook3-FRB-P2A-Pex3-tdTomato-FKBP.

The N-terminal FRB peroxisome assay plasmid was generated using Gibson assembly of three fragments. The first fragment was a PCR product of pKan-CMV-Hook3-FRB-P2A-Pex3-tdTomato-FKBP between AS 894 and AS 895 which generated an FRB domain with homology at its 5' end for the pKan backbone, and a GGSGGS linker encoded at its 3' end. The second fragment was a PCR product of Hook3 between AS 896 and AS 897 which

had homology to FRB-GGGSGGGS at its 5' end, and homology to the peroxisome plasmid P2A region at the 3' end. The third fragment was the backbone of pKan-CMV-Hook3-FRB-P2A-Pex3-tdTomato-FKBP opened at NheI and PvuI to remove Hook3-FRB. The three fragment reaction was assembled in one step at 50 °C for 50 minutes, creating pKan-CMV-FRB-Hook3-P2A-Pex3-tdTomato-FKBP.

2.2 Mammalian cell culture

2.2.1 Maintenance

hTERT immortalised RPE1 cells (Clontech) were maintained in F-12/DMEM (Merck, D6421) supplemented with 10% FBS (Merck, F7524), 1% pen-strep solution (Merck, P0781; final concentration 100 units/ml penicillin, 100 µg/ml streptomycin), 0.365 g/L L-glutamine (Merck, G7513), and 1.2 g/L sodium bicarbonate (Merck, S8761). For imaging experiments where CO_2 would not be supplied, media was exchanged for phenol-red free L-15 (ThermoFisher Scientific, 21083027) supplemented with FBS and pen-strep solution as above.

RPE1 cells were passaged when their confluency reached 70-80 %. To passage the cells in a T25 flask, the media was removed and the cells were washed in 7.5 ml sterile PBS. 0.5 ml Trypsin-EDTA was added and the cells were incubated at 37 °C for around 3 minutes. The cells were resuspended in 5 ml warmed growth medium, and then diluted 1:5 into a fresh flask containing 5 ml of warmed growth medium so that they were between 15-20% confluent. Cells kept in this way needed passaging three times a week.

Stable cell lines expressing NPY-RFP were maintained by the addition of 500µg/ml geneticin (Merck, G8168).

Cells were checked monthly for contamination with mycoplasma.

2.2.2 Transfection with plasmid DNA

RPE1 cells were seeded at around 20% confluency in a 6-well plate, or in a 35 mm glass bottom dish which had been coated with fibronectin (see next section for fibronectin coating). After 1 day, the cells were transfected. 1.5 µg of plasmid DNA (either a single construct, or a combination of plasmids that did not exceed a total 1.5 µg) was diluted into 100 µl of Optimem (ThermoFisher Scientific, 31985062), and then 4.5 µg of Fugene 6 was added (Promega, E2691). The mixture of transfection reagent and DNA was mixed by flicking

Number	Name	Sequence (5' -> 3')
AS 638	SNAPf rev	GTTCGCACCCAGACAGTTC
AS 667	EcoRI-coSF-BICDR1-fw	AGCGTAgaattcATGAGTGCTTTTTGCCTGGG
AS 674	DmrB-KIF1C Top	CTAGTGTTCGACGTGGAGCTGCTGAAGCTGGAGATGGCTGGTGCCTCGGTGAAAGTGGCAGTA
AS 675	DmrB-KIF1C Bottom	CGCGTACTGCCACTTTCACCGAGGCACCAGCCATCTCCAGCTTCAGCAGCTCCACGTCGAACA
AS 676	DmrB-Δ1-KIF1C Top	CTAGTGTTCGACGTGGAGCTGCTGAAGCTGGAGGCTGGTGCCTCGGTGAAAGTGGCAGTA
AS 677	DmrB-Δ1-KIF1C Bottom	CGCGTACTGCCACTTTCACCGAGGCACCAGCCTCCAGCTTCAGCAGCTCCACGTCGAACA
AS 678	DmrB-Δ2-KIF1C Top	CTAGTGTTCGACGTGGAGCTGCTGAAGCTGGAGGGTGCCTCGGTGAAAGTGGCAGTA
AS 679	DmrB-Δ2-KIF1C Bottom	CGCGTACTGCCACTTTCACCGAGGCACCCTCCAGCTTCAGCAGCTCCACGTCGAACA
AS 689	AscI-Hook3 FWD	ACATAggcgcgccctATGTTCAGCGTAGAGTCGCTG
AS 690	EcoRI Hook3 FWD	CCGTAgaattcATGTTCAGCGTAGAGTCGCTG
AS 691	AgeI-BamHI-Hook3 REV	ACAATaaccggtggatcCCTTGCTGTGGCCGGCTG
AS 692	AscI-BICD2 FWD	AACATAggcgcgccctATGTCGGCGCCGTCGGAG
AS 693	EcoRI BICD2 FWD	CCGTAgaattcATGTCGGCGCCGTCGGAG
AS 694	BamHI BICD2 REV	ACAATggatcCAGGCTCGGTGTGGCTGG
AS 719	shHook3 #1 Top strand	GATCCCCCAGCATGAGAATAAGATGTTATTCAAGAGATAACATCTTATTCTCATGCTGTTTTTC
AS 720	shHook3 #1 Bottom strand	TCGAGAAAAACAGCATGAGAATAAGATGTTATCTCTTGAATAACATCTTATTCTCATGCTGGGG
AS 723	shBICD2 #1 Top strand	GATCCCCGGAGCTGTCACACTACATGTTCAAGAGACATGTAGTGTGACAGCTCCTTTTTC
AS 724	shBICD2 #1 Bottom strand	TCGAGAAAAAGGAGCTGTCACACTACATGTCTCTTGAACATGTAGTGTGACAGCTCCGGG
AS 725	shBICDR1-88 Top strand	gatccccGCACTTAGAGCAAGAGAAAttcaagagaTTTCTCTTGCTCTAAGTGCtttttc
AS 726	shBICDR1-88 Bottom strand	tcgagaaaaaGCACTTAGAGCAAGAGAAAtctcttgaaTTTCTCTTGCTCTAAGTGCggg
AS 777	NdeI-GST FWD	TGCCAcatATGTCCCCTATACTAGGTTATT
AS 780	SalI-KIF1C aa922 REV	ATATTgtcgaccCTCCCAGCTTGACAG
AS 894	HomologyA-FRB FWD	TTAGTGAACCGTCAGATCCGCTAGCatgATCCTCTGGCATGAGATG
AS 895	HomologyB-GGSGGS FRB REV	AGAACCTCCAGAGCCTCCGAATTCctttgagattcgtcggaac
AS 896	HomologyB-Hook3 FWD	GAATTCGGAGGCTCTGGAGGTTCTatgttcagcgtagagtcg
AS 897	HomologyA-Hook3 REV	ATTTGTGGCCCCAGAGCCCCGATCGGTccttgctgtggccggctg
AS 967	NotI-STOP Hook3 REV	ATAAATgcggccgcCGaccggtttaCCTTGCTGTGGCCGGCTG

Table 2.3: DNA oligonucleotides used in this work

the tube, and then was incubated at room temperature for 20 minutes. After incubation, the transfection reaction was spread drop-wise over prepared cells. Cells were typically imaged within 72 hours of transfection.

2.2.3   Transfection with siRNA

RPE1 cells were seeded at around 20% confluency as described in the previous section. siRNAs were transfected using Oligofectamine (ThermoFisher Scientific, 12252011). For each well of a 6-well plate or 35 mm imaging dish, two tubes were prepared, the first with 0.6 µM siRNA oligonucleotide in 155 µl of Optimem, and the second with 9 µl of Oligofectamine diluted in a total volume of 45 µl in Optimem. The two tubes were mixed and incubated for 25 minutes at room temperature before being added dropwise to cells in 1.5 ml fresh growth medium. Cells were typically grown for 48-72 hours before imaging. The oligonucleotides used are listed in Table 2.4.

Name	Sequence (5'->3')	Reference
siControl	GGACCUGGAGGUCUGCUGU-[dT]-[dT]	Theisen et al. (2012)
siKIF1C	CCCAUGCCGUCUUUACCAU-[dC]-[dG]	Theisen et al. (2012)
siDHC	GGAUCAAACAUGACGGAAU-[dT]-[dT]	Schlager et al. (2010)

Table 2.4: siRNA oligonucleotides used in this study

2.2.4   Glass imaging dishes

When cells were plated on glass surfaces, the surfaces were first coated with Fibronectin. Fibronectin (Merck, F1141) was diluted to 10 µg/ml in distilled water, and then added to glass fluorodishes. Either flat-bottomed or quadrant-divided glass bottomed dishes were used (WPI, FD35-100 and Greiner, 627870 respectively). Fluorodishes were kept at room temperature for at least 16 hours, and then the fibronectin coating solution was taken off and the surface was washed with distilled water. Coated fluorodishes were usually used immediately, but if they were not then they were fully dried and stored at room temperature until use.

2.3 Acutely inhibitable KIF1C

2.3.1 Cell preparation and imaging

RPE1 cells were seeded at around 20% confluency in 6-well plates, and the next day were transfected with the relevant DmrB-KIF1C-GFP plasmid using Fugene. After a further day, the cells were trypsinised in around 100 µl Trypsin-EDTA, resuspended in 2 ml growth medium, and divided between quadrant glass-bottom dishes which had been coated with fibronectin as described. Once cells had adhered and had time to settle (at least 6 hours, or the next day), the media in each quadrant was exchanged for 500 µl of L-15 and they were placed on the microscope without a lid. Using a DeltaVision Personal widefield microscope equipped with a 40X Olympus objective, several cells within a quadrant had their positions marked, and the microscope visited those points and took an image in the GFP channel each minute using an exposure time of 500 ms and a LED intensity of 32%. Once the microscope had imaged all cells at least once, a final concentration of 2 µM of B/B homodimeriser (Takara, 635058) was added directly to the quadrant without pausing imaging. The cells in each quadrant were imaged for a total of 16 minutes.

2.3.2 Analysis of KIF1C accumulations

The mean intensity of a square region around the centrosome was measured, and divided by the mean intensity of an area of cytoplasm nearby to give the fold-brightness of the centrosome over the background. This was done likewise for a region around the tail or peripheral accumulation of KIF1C. Tails of cells were identified by their morphology as long tapering trailing adhesions at the opposite end of the cell to the lamellipodia (see Theisen et al. (2012) for definition of "tails"). When a clear tail was not visible, the most distant peripheral accumulation of KIF1C from the nucleus was used. These values were measured at the beginning and end of imaging to elaborate the effects of KIF1C acute inhibition.

2.4 Peroxisome sorting assay

2.4.1 Cell preparation and imaging

Cells were prepared as described for DmrB-KIF1C-GFP experiments, however, where depletion with siRNA was performed, cells were seeded as before, RNAi depletion was started after 24 hours, cells were transfected with plasmids at 48 hours and then imaged at between 72-96 hours.

Cells were imaged on a DeltaVision Personal widefield microscope using an Olympus 60X objective and 2x2 camera binning. Cells were imaged with an exposure time of 200ms and typically 5% LED power using an mCherry excitation/emission filter set. Cells were imaged for around 20 seconds, rapamycin was added directly to the well at a final concentration of 0.2 µM, and then cells were imaged for a further 2-3 minutes at 2.5 frames per second.

2.4.2 Analysis of peroxisome motility

Peroxisome motility was tracked using TrackMate, a plugin for ImageJ (Tinevez et al., 2017). Spots were first fit to the frames of the movie using a Laplacian of Gaussian method with an estimated blob-size of 0.5 µm. The threshold for detection was manually altered to ensure the detected spots were real and not background. The spots were then linked using TrackMate's Linear Assignment Problem tracker with a frame-to-frame maximum linking distance of 2 µm. After track linking, the data were exported from TrackMate as an XML file and further analysed in a purpose made python package.

We developed a python package to read trackmate formatted XML files and interpret the spot and track data into object-orientated programming. The main axis of the cell was found by fitting an ellipse to the tracked points, and upon import of data, a graph of the tracked points was shown to the user to allow them to determine the centrepoint of the cell. This centrepoint was used to segment tracks into movements that went towards or away-from the centrepoint. The diffusion coefficient of non-activated peroxisomes was estimated from mean-squared displacement calculations. Moments of diffusion were segmented from tracks by implementing a method developed by our colleagues that looks at the sequential trajectories a particle has and comparing their movement to the diffusion coefficient. For more details, see Jeanneret et al. (2016).

2.5 BioID proximity based labelling

For each BioID experiment, 3x 15cm dishes of RPE1 cells were grown (as described in 2.2) to a confluency of 90%. BioID plasmids were transfected using 20 µg of DNA pre-diluted in 1.5 ml optimem, which was then mixed by vortexing with 60 µg polyethylenimine (PEI). After 15 minutes of incubation, the transfection mixture was placed onto the cells dropwise, and the dish was mixed in a North-South East-West motion. After 24 hours, cells were placed into fresh medium containing 20 µM d-Biotin (Merck, B4501) . After a further 12 hours, cells from all three replicate dishes were harvested by trypsinisation and stored as a single pellet.

Pellets of cells (10-15 million) were lysed in 1 ml RIPA buffer (Merck, 20-188) containing 1x cOmplete protease inhibitor by passing through a needle. Insoluble material was cleared in a table-top centrifuge, 20,000 rpm for 30 minutes at 4 °C. The resultant supernatant was incubated with 50 µl streptavidin Dynabeads for 1.5 hours, and the beads were washed with 1 ml PBS three times. Beads were stored at -20 °C until they were processed for mass spectrometry.

To prepare peptide samples for mass spectrometry, beads were resuspended in 45 µl of 50 mM ammonium bicarbonate, reduced by the addition of 10 mM TCEP, and subsequently alkylated by adjusting to 40 mM chloroacetamide incubating at 70 °C for 5 minutes. Peptides were separated from beads using a 0.22 µm spin-filter and then desalted using C18 stage tips. 20 µl of peptides were analyased by nano LC-ESI-MS/MS in an Ultimate 3000/Orbitrap Fusion.

After identification and quantification in MaxQuant, data were imported to Scaffolds software and compared statistically using a Fisher's exact test with Benjamini-Hochberg correction, which resulted in a significance threshold of 0.0019 for a 5% FDR.

2.6 Insect cell culture

2.6.1 Maintenance

Sf9 insect cells were maintained in Ex-Cell 420 serum-free media (Sigma, 14420C) at a pre-log density of 0.5-0.75x10^6 cells/ml. When large cultures were required, cells were rapidly expanded by keeping them in mid-log phase

around 1-2x10^6 cells/ml, allowing them to double approximately every 24 hours.

2.6.2 Transfection with bacmid DNA

For each transfection, 1 million cells were plated into a 35 mm dish in a total volume of 2 ml. 2 µg of recombinant bacmid DNA was diluted into a total volume of 200 µl SF9 media, 6 µl FuGENE HD transfection reagent (Promega, E2311) was added and the solution was mixed by pipetting. After 15 minutes, the transfection mix was dribbled over the dishes containing cells, and dishes were kept at 27 °C with humidity for 3-5 days, until the monolayer of cells showed signs of infection, and those cells that remained in suspension had acquired YFP signal. At this point, P1 virus was harvested from the supernatant after removing remaining cells by centrifugation, 13,000x RPM, 5 minutes.

2.6.3 Viral expansion

To produce P2 virus, the entire P1 virus was diluted 1:100 into Sf9 cells at a density of 0.5x10^6 cells/ml (typically 50 ml) and incubated for up to 5 days until cell density had fallen and those that remained exhibited bright YFP fluorescence. To harvest the virus, the cells were spun 2,500 x g for 5 minutes and the supernatant was filtered through 0.45 µm PVDF membrane (Merck Millipore, SLHV033RS) and was stored at 4 °C protected from light until it was used. Virus-containing supernatants were used within 2 months or discarded. In some cases, virus was futher expanded to make P3 viruses, diluting P2 virus 1:10 into 50 ml of Sf9 cells at a density of 0.5x10^6 cells/ml and growing for 2-3 days until the majority of cells showed YFP fluorescence.

2.6.4 Protein expression

Cells were infected at a density between 1.5-2x10^6 cells/ml with 1:100 dilution of P2 or P3 virus. Cultures grown for 48-72 hours or until all cells contained YFP fluorescence under the microscope. Cells were harvested by centrifugation, 500 x g for 15 minutes, and pellets were stored at -80°C until used.

2.7 Protein purification

Unless otherwise stated, all protein purification procedures were performed at 4°C.

2.7.1 Cell lysis

Bacterial or SF9 cells were lysed in lysis buffer (protein dependent, detailed below) supplemented with 1x cOmplete protease inhibitor cocktail (Roche, 6538282001). For bacterial cells, lysis was achieved using a sonicator in 1 minute intervals for a total of 3 minutes at 50% duty ratio. For insect cells, lysis took place in a tissue dounce, using 20-30 strokes. The resultant lysate was cleared by centrifugation, 50,000xg, 40 minutes.

2.7.2 Purification of KIF1C-GFP, KIF1C-(d623-825)-GFP, and KIF1C(R463A-K464E)-GFP

Buffer	Composition
Kif1C SP Lysis	50mM Sodium phosphate buffer pH 7.5, 50mM NaCl, 1mM MgCl2, 0.1mM ATP
Kif1C SP Wash	50mM Sodium phosphate buffer pH 7.5, 150mM NaCl,
Kif1C SP Elution	50mM Sodium phosphate buffer pH 7.5, 300mM NaCl
Kif1C Ni-NTA Wash	50mM Sodium phosphate buffer pH 7.5, 150mM NaCl, 40mM Imidazole, 10% Glycerol
Kif1C Ni-NTA Elution	50mM Sodium phosphate buffer pH 7.5, 150mM NaCl, 300mM Imidazole, 10% Glycerol

All variants of Kif1C were purified by a two-step procedure, starting with SP ion-exchange chromatography and ending with a Ni-NTA affinity chromoatography.

Sf9 cell pellets (5-15 g) were lysed and cleared of insoluble debris as described. Cleared lysate was incubated with 0.5-3ml of SP Sepharose (Cytiva, 17-0729-01) for 1.5 hours, loaded into a gravity flow column, and washed with 100 column volumes (CVs) of KIF1C lysis buffer. The column was then washed with 100 CVs of KIF1C SP wash buffer and eluted in KIF1C SP elution buffer.

Elutions from the SP purification were adjusted to 150 mM NaCl, 20 mM imidazole, 1 mM $MgCl_2$ and 0.1 mM ATP before being batch bound to 500 µl Ni-NTA beads (Qiagen, 30250) for 1.5 hours. The beads were washed with 250 CVs Kif1C Ni-NTA wash buffer before being eluted 250 µl volumes of

Kif1C Ni-NTA elution buffer. Purified protein was aliquotted and kept in liquid nitrogen until use.

2.7.3 Purification of BICD2-SNAPf, BICDR1-SNAPf and HOOK3-SNAPf

Buffer	Composition
His Adaptor Lysis Buffer (HA-LB)	50mM HEPES pH 7.4, 150mM NaCl, 20mM Imidazole
His Adaptor Wash Buffer (HA-WB)	50mM HEPES pH 7.4, 150mM NaCl, 60mM Imidazole
His Adaptor Elution Buffer (HA-EB)	50mM HEPES, pH 7.4, 150mM NaCl, 300mM Imidazole
TEV Cleavage Buffer	50mM Tris pH 7.4, 148mM KAc, 2mM MgAc, 1mM EGTA, 10% Glycerol

Sf9 cell pellets (5-15 g) were lysed in HA-LB and cleared of insoluble debris as described. Cleared lysate was loaded on to 1-2ml of Ni-NTA agarose beads (Qiagen, 30250) and batch-bound for 1.5 hours. Beads were transferred to a gravity flow column and washed with 100-200 CVs of HA-LB followed by 100-200 CVs of HA-WB. Protein was eluted in up to 10ml of HA-EB, which was subsequently batch-bound to 1ml IgG Sepharose (Cytiva, 17096901) for 1.5 hours. When not labelling SNAP-tag protein with organic fluorophores, the protein-bound IgG beads were washed with 100-200 CVs TEV Cleavage Buffer, transferred to an eppendorf tube, and the protein was cut off of beads by incubation with 40 µg/ml TEV protease either at 25 °C for 1 hour, or overnight at 4 °C. Alternatively, when labelling was required, protein-bound IgG beads were first washed with 100 CVs of TEV Cleavage buffer, transferred to an eppendorf and incubated with 3-5 µM benzylguanine conjugated fluorophore (NEB, S9136S) for 2 hours before being returned to the column, washed with a further 100 CVs of TEV Cleavage buffer, and cut off the beads with TEV protease as described above. The protein was collected from the beads and the bead bed was washed with a further 1 CV of buffer. The collected protein was subjected to a clearing spin at 13,000 rpm at 4 °C for 5 minutes before being aliquotted.

2.7.4 Purification of Hook3-SNAPf with size-exclusion chromatography

For purification of Hook3-SNAPf where a gel filtration step was desired, a single step Ni-NTA purification was performed as described above, protein was eluted from Ni-NTA resins and then concentrated to a volume of around 600 µl using 30 KDa cut-off centrifugal filters (Millipore, UFC803024). The concentrated protein was simultaneously digested with TEV protease and labelled with Alexa-647 SNAP dye in solution for 2 hours at 4 °C. Protein was spun at 13,000 rpm at 4 °C for 5 minutes before 500 µl was injected into a Superose 6 increase 10/300 column prepared in gel filtration buffer (50 mM HEPES 7.4, 150 mM NaCl, 1 mM DTT). The peak corresponding to Hook3-SNAPf between 11-12 ml was pooled and concentrated with a 30 KDa centrifugal concentrator in the presence of 10% glycerol. The final concentrated product was aliquotted, snap-frozen and stored in liquid nitrogen until use. A typical final concentration of Hook3-SNAPf was around 0.36 mg/ml with an estimated labelling efficiency of 70%.

2.7.5 Purification of untagged Hook3 with size-exclusion chromatography

Minimally tagged His-ZZ-LTLT-Hook3 was purified by a single-step IgG sepharose purification followed by gel filtration over a Superose 6 increase 10/300 column. The purification buffer used throughout was 50 mM HEPES 7.5, 150 mM NaCl, 2.5 mM $MgSO_4$, 10% Glycerol, 2 mM DTT, 0.1 mM ATP and 0.05% Triton X. Lysis was performed as previously described, cleared lysates were bound to 750 µl of IgG sepharose beads for 3 hours, and the beads were washed with 300-400 ml of purification buffer. Beads were resuspended in a 1.5 ml eppendorf and incubated with 40 µg/ml TEV protease for 1 hour at 25 °C with agitation. Eluate was collected in a gravity flow column, the beads were washed with an additional 1 CV of buffer, and then the protein was concentrated using a 30 KDa centrifugal concentrator to a final volume of around 600 µl. The protein was clear spun at 13,000 rpm at 4 °C for 5 minutes before being injected into a prepared Superose 6 increase 10/300 column in gel filtration buffer (50 mM HEPES 7.4, 150 mM NaCl, 2.5mM $MgSO_4$, 1 mM DTT). The peak corresponding to Hook3 at around 11-12 ml was concentrated in the presence of 10% glycerol and then aliquotted, snap-frozen, and stored in liquid nitrogen until use. The final concentration of Hook3 prepared in this

way was 0.141 mg/ml as measured by A280nm absorbance.

2.7.6 Purification of Lis1

Sf9 cell pellets (~10 g) were lysed and cleared as described. The purification buffer used throughout was 50 mM Tris pH 8.0, 250 mM KOAc, 2 mM MgOAc, 1 mM EGTA, 10% glycerol, 1 mM DTT. Cleared lysates were bound to 2 ml of IgG Sepharose beads which had been pre-washed in 0.5 M HAc brought to pH 3.5 with NH_4Ac. Batch-binding occured for 2 hours at 4 °C on a roller, and then the beads were placed in a polypropylene gravity-flow chromatography column and washed with 100 CVs of purification buffer. The beads were re-suspended in 4 ml total volume of purification buffer, and incubated with 0.3 mg/ml TEV protease at 25 °C for 1 hour with agitation. The cleaved protein was collected from the beads, and the beads were washed with a further 1 CV of buffer to recover the remaining cleaved protein. The 4 ml of eluted Lis1 was hard-spun at 4 °C for 15 minutes and was then injected into a pre-pared Superdex 200pg 16/60 column in gel filtration buffer (25mM Tris pH 8.0, 150mM KCl, 1mM $MgCl_2$, 5 mM DTT). Lis1 was eluted in one peak at around 75 ml and the peak fraction's concentration was 3.2 mg/ml. The peak fraction was adjusted to 10% glycerol, aliquotted, snap-frozen and stored in liquid nitrogen. The fractions surrounding the peak were pooled and concentrated in a 30 KDa cut-off centrifugal filter in the presence of 10% glycerol until the volume was 800 μl and the concentration was 13.87 mg/ml. This protein was aliquotted as described for the peak fraction.

2.7.7 GST-control, GST-KIF1C-stalk and GST-KIF1C-stalk-GFP

KIF1C-stalk construct encoded the amino acids of KIF1C's stalk domain between 612-912. GST-control, GST-KIF1C-stalk and GST-KIF1C-stalk-GFP were expressed in BL21-CodonPlus (DE3)-RIPL (Agilent, 230240) *E. coli* cells in double yeast tryptone broth (DYT). Transformed cells were grown to an OD_{600} of 0.5 at 37 °C, 200 rpm, and then shifted to 18 °C and grown for a further 16 hours with 1 mM IPTG (VWR, 367-93-1). Cells were harvested by spinning at 4,000 x g for 15 minutes in an Fiberlite F10-4 rotor.

Bacteria were resuspended in GST lysis buffer (50 mM Tris pH 7.4, 300 mM NaCl, 0.05% v/v Tween 20 and 1 mM DTT), were lysed by sonication, and cleared of insoluble material as described. The cleared lysate was bound to 1.5 ml GSH Agarose beads (Generon, SuperGlu25A) for 1.5 hours at 4 °C.

Beads were loaded into a polypropylene gravity-flow column and washed with 300 CVs of GST wash buffer (lysis buffer with 500 mM NaCl). Finally, protein was eluted from beads using GST elution buffer (lysis buffer with 10% glycerol and 20 mM reduced glutathione). Eluted protein was aliquotted, snap-frozen and stored in liquid nitrogen until use. Proteins were typically between 0.5-6.0 mg/ml in concentration.

2.7.8 KIF1C-motor-GFP purification

KIF1C-motor-GFP, encoding amino acids 1-349 of KIF1C and known as "motor-GFP" in this work, was expressed in *E. coli*, harvested and lysed as has already been described in Method 2.7.7. Cells were lysed in Motor lysis buffer (50 mM Tris pH 7.4, 300 mM NaCl, 20 mM Imidazole, 0.1 mM MgATP, 1 mM MgCl$_2$, 1 mM DTT fresh). Cleared lysates were bound to 1.5 ml of Ni-NTA beads for 1.5 hours at 4 °C, then loaded into polypropylene gravity-flow columns and washed with 300 CVs of lysis buffer, followed by 150 CVs of wash buffer (lysis buffer containing 40 mM imidazole). Finally, protein was eluted from Ni-NTA resins in sequential 0.5 CV volumes using elution buffer (lysis buffer containing 500 mM imdiazole and 10% glycerol). Protein was aliquotted, snap-frozen and stored in liquid nitrogen until use. Protein prepared in this way had typical concentrations of 0.1-0.4 mg/ml.

2.8 *In vitro* reconstitution

2.8.1 Acid-washed glass preparation

Menzel Gläser No. 1.5 22x22 mm and 22x50mm coverslips were placed in holding racks and were submerged in 6.4% wt/v HCl at 60 °C for 16 hours. The HCl was exchanged for distilled water, and the coverslips were sonicated in a sonic waterbath for 5 minutes at a time, exchanging the distilled water between sonications. The sonication step was repeated 5 times and then coverslips were dried with compressed air. Coverslips were stored between layers of lense tissue (Ross Optical, AG806) inside pipette boxes until they were used.

2.8.2 TIRF flow-chamber construction

Before chamber construction, the acid-washed glass coverslips were plasma cleaned in a Henniker plasma clean (Henniker Plasma, HPT-200) for 5 minutes. For each flow chamber, a 75x25 mm SuperFrost Plus glass slide (Thermo Scientific, J1800AMNZ) was taken and double-sided tape (Tesa, 64621) was laid in two parallel lines with a gap of 5mm in between them. A single coverslip was laid over the tape and flattened to create an enclosed chamber with a volume of approximately 10-15 µl. Imaging was performed through the 22x22 mm coverslip by upturning the chamber and placing it on to the microscope objective. In order to keep chamber construction consistent, a to-scale drawing was made and used to guide tape and coverslip placement (see Figure 2.1 a.).

In experiments where additional components would be added to the TIRF flow-chamber while it was on the microscope, an open chamber design was adopted. Chambers were constructed between a 22x50 mm coverslip with a 22x22 mm coverslip on top. By imaging through the 22x50 mm coverslip, the top of the chamber was left open allowing additional components to be flowed into the chamber *in situ*. Again, a to-scale drawing was used to aid consistent placement of tape and coverslips (see Figure 2.1 b.). These chambers were not as hydrophillic as those created with the SuperFrost Plus coated glass slides, and therefore they were pre-wet with 0.1% v/v Triton X-100 to prevent formation of air gaps.

2.8.3 Single-molecule microscopy buffers

1X MRB80 and 5X TAB stocks were stored at -20 °C. 1X TAB and 1X TAB-KC-KCl were made fresh on the day of use.

Buffer	Composition
1X MRB80	80 mM PIPES pH 6.8, 4 mM $MgCl_2$, 1 mM EGTA, 1 mM DTT
5X TAB	125 mM HEPES pH 7.2, 25 mM $MgSO_4$, 5 mM EGTA
1X TAB	25 mM HEPES pH 7.2, 5 mM $MgSO_4$, 1mM EGTA, 1mM DTT, 10 µM paclitaxel
1X TAB-KC-KCL	1X TAB with 0.2 mg/ml κ-casein, 25 mM KCl and 20 µM paclitaxel
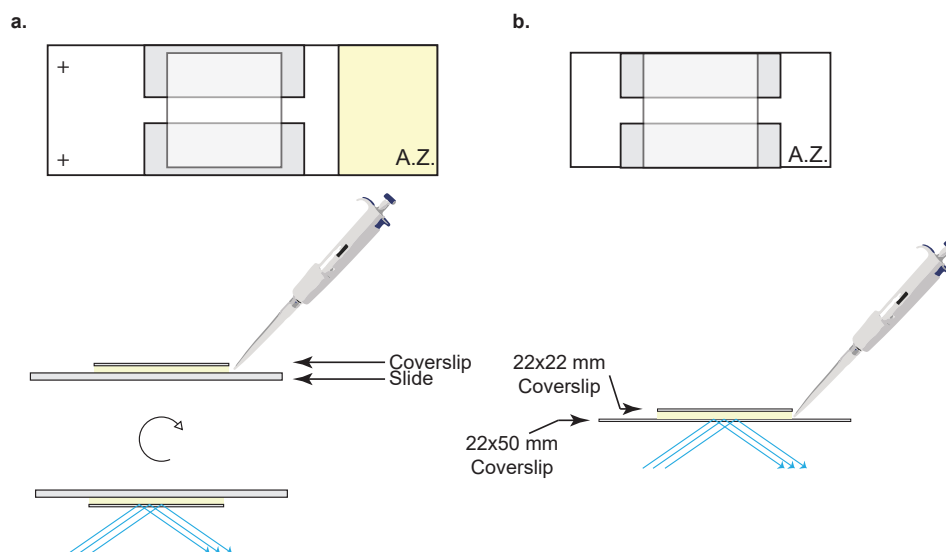
Figure 2.1: TIRF flow-chamber construction | a-b. To-scale drawings of TIRF chamber construction used as a guide for constructing TIRF chambers, along with their imaging mode where **a.** shows a typical design where the flow chamber would not be accessible during imaging, whereas **b.** shows an alternative open design where components could be flowed in *in situ*.

2.8.4 GDP-Taxol microtubule polymerisation

Microtubules were polymerised in a final volume of 20 µl MRB80 using 82 µg of unlabelled porcine tubulin with 2.5 µg of biotin-labelled porcine tubulin (Cytoskeleton, T333P-B), and 2 µg of HiLyte-647 porcine tubulin (Cytoskeleton, TL670M) when fluorescence was desired. The mixture of diluted tubulin was pipetted to mix, and then spun for 5 minutes in a chilled airfuge (Beckman Coulter, 340401) at around 80,000 rpm. The spun tubulin mixture was placed into a 0.5 ml eppendorf tube, a final concentration of 5 mM GTP was added, and microtubules were allowed to polymerise for 1 hour at 37 °C. After 1 hour, the mixture was topped up to 100 µl by the addition of 80 µl MRB80 containing 50 µM paclitaxel (Alfa Aesar, J62734.MC), flicked to mix, and kept at room temperature. The next day, microtubules were pelleted in a benchtop centrifuge at 13,000 x rpm for 12 minutes, the supernatant containing any unpolymerised tubulin was removed and replaced with 100 µl MRB80 containing 50 µM paclitaxel. The microtubule pellet was flicked to resuspend it, and once it had been broken up, the microtubules were pipetted gently 5-10 times with a 200 µl pipette tip until no traces of the pellet were remaining. Microtubules prepared in this way were kept for 3-4 weeks with the tube wrapped

in aluminium foil, and diluted 1:50 in taxol-containing buffer prior to use in microscopy chambers.

2.8.5 Microtubule attachment to flow-chamber

Throughout the following steps, flow chambers were kept up-turned in humidified chambers to avoid drying.

Chambers were first coated with PLL(20)-g[3.5]- PEG(2)/PEG(3.4)-biotin(50%) (Susos) by flowing in 12 µl of a 0.2 mg/ml solution in MRB80. Chambers were incubated for at least 10 minutes before being washed with 30µl TAB, and then 12 µl of 0.625 mg/ml streptavidin (Merck, S4762) in TAB was added.

The primed chambers were stored in a humidified environment for up to 4 hours before being used. Directly before use, excess streptavidin was washed away with 30µl TAB. One tube of 1:50 diluted polymerised GDP-taxol microtubules was made prior to a single day's experiments, and 14 µl of this dilution was added to the chamber. The microtubules were allowed to attach for 10-20 seconds before unstuck microtubules were washed away with 14 µl TAB. The chamber was blocked for a period of 1-2 minutes using 1 mg/ml κ-casein (Merck, C0406) in TAB buffer. Excess κ-casein was washed away with 14 µl TAB and then reaction mixtures were flowed into the chamber. All steps following streptavidin addition were performed at the microscope and chambers were imaged as soon as the reaction mixture had been added.

2.8.6 Reaction mixtures for single-molecule microscopy

The reaction mixture which was imaged in TIRF microscopy contained an ATP regenerating system as well as an oxygen scavenger system. Stocks of MgATP (Melford,B3003), phosphocreatine (Merck, P7936), creatine phosphokinase (Merck, C3755), catalase (Merck, C9322), glucose oxidase (Merck, G7141), DTT and glucose were all diluted in TAB such that a 1:20 dilution in the 20 µl reaction mixture (made up in TAB-KC-KCl) achieved the desired final concentrations. The final concentration of these components was 5 mM ATP, 5 mM phosphocreatine, 7 U/ml creatine phosphokinase, 0.2 mg/ml catalase, 0.4 mg/ml glucose oxidase, 4 mM DTT and 50 mM glucose.

To this prepared imaging mixture, either 0.4, 0.5 or 1 µl of protein complexes were added depending on the experiment, and this represented dilution factors of 1:50, 1:40 and 1:20 respectively.

2.8.7   Protein complex mixtures for single-molecule microscopy

For multi-protein complex reconstitutions, the proteins were incubated to-
gether at a higher concentration and then diluted into the TIRF assay. The
exact concentrations in pre-mixtures and final concentrations in assays are
indicated in the relevant Results sections. Dynein complexes were always
mixed in the same way. First, the protein components are pipetted into a 0.5
ml eppendorf tube on ice. The protein complex mixture is made up to 2.5 μl
with either the relevant control buffer (where proteins are added or removed),
or GF150 (25 mM HEPES 7.4, 150 mM KCl). These proteins are then mixed
1:1 with TAB which contains no added salt, and thus the final salt concentra-
tion during protein interaction is ~75 mM KCl. The complex mixture is pipetted,
spun down, and then retained on ice for 45-60 minutes. Just before use, the
complexes are mixed once more by pipetting.

2.9   TIRF-based microtubule binding assay

To measure the ability of KIF1C's motor domain to bind to microtubules in the
presence of its stalk, 80 nM motor-GFP was pre-incubated with either 20 μM
GST-stalk or the same amount of GST as control. These mixtures were then
diluted 1:20 into TIRF imaging mix as described in Method 2.8.6, such that the
final concentration of motor-GFP and GST-stalk/GST-control was 4 nM and
1 μM. The mixture was flowed in to chambers containing unlabelled GDP-
taxol microtubules, and for each experimental replicate, 10 random fields of
view were captured with an exposure time of 400 ms and 21.4% 488 laser
power. To account for time effects, control and experimental chambers were
prepared in parallel and we alternated which was imaged. To capture mean
intensities along the microtubule, microtubules were hand traced with a line
ROI in ImageJ and then measured. A portion of background close to the mi-
crotubule was also measured and subtracted from the microtubule's intensity
measurement to create a local-background corrected intensity.

2.10   Fluorescent spot co-localisation and bleaching

To co-localise spots of motors and adaptors, flow-chambers were prepared
with cleaned coverslips, pre-wet with TAB, but not coated with any solutions.
Mixtures of dynein-TMR, dynactin, adaptor-647 and KIF1C-GFP were made

with concentrations of 100 nM dynein, 100 nM dynactin, 800 nM adaptor (BICD2-SNAPf, Hook3-SNAPf or BICDR1-SNAPf) and 90 nM KIF1C-GFP. After incubation on ice for 45 minutes, the premixed complexes were diluted 1:20 into a TIRF reaction mixture as described in Method 2.8.6, however the ATP regeneration system was omitted for this experiment. The mixture was flowed into TIRF chambers and allowed to adhere non-specifically for 10-20 seconds, then the buffer was exchanged with fresh TIRF reaction mixture to wash away any unstuck fluorescent molecules. Fields of view were chosen where fluorescent dots were isolated with space around them, and an image was taken in each channel using 200 ms exposure time with the following laser lines and powers: 488 nm 30%, 561 nm 20%, 640 nm 20%.

The spot's positions in each channel were captured using ImageJ's "Find Maxima" function, and the threshold for detection was altered manually to ensure background was not selected as spots. The captured locations were then fit with a 2D Gaussian using ImageJ's GaussFit_OnSpot plugin, and the fit was constrained within a 6x6 pixel box around the center of the detected maxima. The Gaussian fit parameters such as location, width and intensity were recorded. A python script was made to read these detection data, and further filter any detections which showed a very large Gaussian width (>= 800nm), or that had an integrated spot intensity below local background. A masking system was implemented to only include detections from the central portion of the image where the laser illumination was brightest, but use of this masking did not change the resultant co-localisation results and so it was not used. A spot in one channel was then said to co-localise with a spot in another channel if both spots had an integrated Gaussian intensity of >= 500 AU.

For step-wise photobleaching of Hook3-SNAPf, 5 nM of Hook3 was flowed into chambers in the same way as described for spot co-localisation experiments. The laser power and exposure time were chosen so that the majority of spots bleached over 2000-3000 frames, and typical laser powers were 25-30% 640 nm with an exposure time of 100 or 150 ms. Fluorescent spots were found in the first frame of the movie using ImageJ's "Find Maxima" function, and then the mean intensity of the spot was recorded for all frames of the movie in a 5x5 square centred on the spot. A python script was created to plot the mean intensity of spots over time along with a filtered signal, and then show them to the user for the bleach steps to be assigned manually. The python script took keyboard input from the user to assign a bleach step number to the trace, or press "0" if no steps could be identified. The proportions

43

of 1-4 bleach steps as well as >= 5 bleach steps were presented in the final figure.

2.11   Analysis of motor motility

In analysing motor trajectories, we needed to consistently link together data from the creation of kymographs from microscopy recordings, through to the individual motor's movements and fluorescence, and in each step the multiple channels that had been recorded needed to be factored in. To do this successfully, we needed to standardise each section of the analysis pipeline, as well as the file names and directory structures that were created to store the different data.

Our kymograph analysis pipeline consists of three main stages: first, microtubules are hand-traced in a maximum intensity projection or reference image, and then kymographs are generated for all the channels that were recorded. Next, motor tracks are hand traced in kymographs and the path they took is stored in nanometer and second terms in a .csv file, while the pixel path they took is also saved as a region of interest (ROI) file. Finally, a python analysis software package reads the saved tracks and makes sense of them.

2.11.1   Multi-ROI multi-colour kymographs

To generate kymographs for all recorded channels of a microscopy experiment, an ImageJ script was created that visited each recorded microtubule ROI in each channel and generated a kymograph for it. The kymographs were named uniquely, such that a single kymograph could be easily linked back to an experiment. This naming scheme was as follows:

Experiment_Name_Kymograph_**number_channel**.tif

For example:

2021_01_27_Ch2_DDHL_KS_001_Kymograph_**1_488ec2**.tif

From this naming scheme it could easily be determined that this kymograph originated from the second chamber made on the 27th January 2021, the complex observed was DDHL-KS, it was the first movie recorded, the kymograph was the first created and this particular file corresponds to the 488ec2

imaging channel. A corresponding ROI file is saved should the original micro-tubule need to be re-visited, and a square of the reference image from which the microtubule was traced is also saved should it need to be referred back to.

2.11.2 Motor tracing

Motor tracing from kymographs was also performed by hand, as we found this gave greater accuracy than the currently available automated alternatives. An ImageJ macro was created that recorded the polyline ROI which was used to trace the motor's path, and also saved a .csv file containing the motor's path in real terms (distance in nm and speed in nm/s) along with the kymographs dimensions. These files contained the full kymograph name, as well as a unique track number. This macro also aided motor tracing by additional helping functions such as drawing a numbered grid for finding corresponding motor traces between several kymographs drawn in different channels.

2.11.3 Python motor-track analysis package

In order to link together information about motor's run characteristics, a python motor-track analysis package was created. The key functionality of this package was that it allowed you to investigate parameters of the motor's motility at the single motor level, the per-microtubule level, the per-movie level, the per-experiment level as well as compare experimental repeats. With the ability to deconstruct the data in this way, we could identify if single experiments were artificially affecting average measurements, and could also compare experiments across several days.

The python analysis package was responsible for taking the discrete points that were hand tracked from kymographs and making sense of them. The core of the code reads the recorded data and calculates the parameters described below: run length, dwell times, run speeds, landing rates and directionality. Using the python package, the user can call commands to get per-microtubule, per-experiment or per-dataset level accumulations of these parameters and parameters that derive from them. Key to usefulness of the package is the implementation of a "filter" method. The user may write their own method to determine which tracks they wish to include in their analysis, and can combine any number of parameters to select the most relevant subset of data. For example, a filter method to find only the most motile Plus-end

directed motors might look like this:

```python
def example_filter(track: Motor_Track):
    if track.directional_classification == "Plus" and track.average_speed() >
    ↪  200:
        return True
    else:
        return False
```

Run lengths and dwell times

Using the phase duration, length change, and speed recorded for each part
of a path, paths were segmented into runs. A run was defined as the distance
covered before falling static (having an absolute speed of less than 20 nm/s),
or the distance covered before changing direction (having a speed of more
than 20 nm/s in one direction and then a speed of more than 20 nm/s in the
opposite direction). For each segment of the path, it was determined whether
this segment was going towards the plus- or minus-end of the microtubule, or
whether the motor was paused, and the time spent in each mode of transport
was tallied. The total time a motor spend on the microtubule was its dwell
time. The total run length in the plus- or minus-end direction was also tallied
for the individual runs within the track. The total run length was defined as the
sum of the absolute values of the individual runs:

$$\sum_{i=1}^{i=n} |R_i|$$

where R = individual run distances.

Speeds

From the total distance and time-spent values, the average speed of a particle
was defined as:

$$\overline{v} = \frac{|d_{minus}| + d_{plus}}{t_{plus} + t_{minus} + t_{paused}}$$

Where d is the distance travelled, $\overline{v}$ is average speed and t is time.

Alternatively, by segmenting tracks in this way we could calculate the average speed of motors ignoring any paused periods:

$$\overline{v} = \frac{|d_{minus}| + d_{plus}}{t_{plus} + t_{minus}}$$

Landing rate

Using the predictable file naming scheme described above, individual tracks had names in the format:

(Experiment_name)_Kymograph_**(number)_(channel)**.tif_**(tracknumber)**.csv

The number of tracks for an individual microtubule could be calculated by counting how many files matched the kymograph's name and number (but not channel, as often tracks were drawn in multiple channels). The kymograph width was stored within the tracking data allowed calculation of a landing rate as the number of tracks divided by the width of the kymograph in nanometers, and the length of the kymograph in seconds. This value was scaled to per micron per minute by multipying it by 60,000.

Directionality

The overall directionality of a track was defined in the following way. Firstly, any track that travelled a total distance of less than 1000nm was labelled as "Static". Any remaining track that travelled only towards the plus-end was labelled "Plus", while any track that travelled only towards the minus-end was labelled "Minus". Any track that travelled more than 1,500 nm in the plus- and minus- end directions was labelled "Bidirectional". After this classification, any remaining track that travelled more towards the plus-end than the minus- was labelled "Plus", while the opposite was labelled "Minus". Therefore a track that travelled 20,000 nm in the minus-end direction and 200 nm in the plus-end direction would still be labelled as "Minus".

2.12   Measuring fluorescence of running motors

The fluorescence of motor complexes was measured using the traces which had been captured when measuring motor motility, as well as the recorded regions of interest (ROIs) of the microtubule's position within movies. Motor

47

traces were mapped back to their original position in movies, and 2D Gaussians were fitted to spots to measure motor's intensities.

2.12.1 Testing kymographs for horizontal flipping

Kymographs were often flipped during analysis so that the minus-end of the microtubule was always on the left side of the image. In this way, the motor tracing macro interpreted movements towards the right-hand side of a kymograph as positive values, whereas movements towards the left-hand side of the kymograph were negative values, and thus the polarity of the run events was captured. In order to find intensities of motors within the original TIRF movie, we first needed to work out if the motors had been traced within a flipped kymograph. Using the recorded ROI of the microtubule, a test kymograph was generated and compared to the stored kymograph from which motor tracing had been performed. The test kymograph was compared to the stored kymograph before and after horizontal flipping, and the average per-pixel intensity differences were calculated. The mean difference was largest when the test kymograph and stored kymograph were flipped with respect to each other, whereas it was close to zero if the stored and test kymographs were in the same orientation. By comparing these two mean differences, the flip state of the kymograph was solved.

2.12.2 Mapping motor traces to original 2D positions

Motor traces were sampled along the polyline ROI every 0.5 pixels, giving the X position of the motor along the kymograph and the Y position within the kymograph, which was the frame number within the original movie. The ROI corresponding to the microtubule within the 2D movie was also sampled every 0.5 pixels, and an array of the cumulative distance along the microtubule between these points was calculated and mappped to their corresponding (X, Y) positions. The X position of the motor was mapped to the closest cumulative distance on the microtubule, and this was converted to the (X, Y, T) position within the movie. These (X, Y, T) values were saved and used as locations for intensity measurements to be taken.

2.12.3 Measuring intensities of motor spots

All (X, Y, T) positions of the motors were visited for all channels of the original movie, and a 2D Gaussian function was fitted using GaussFit_OnSpot ImageJ macro in a 5x5 subregion. The fitting data for each track was collated and mapped back to the track's tracking data within the python motor analysis package. Spot fits were further filtered to exclude any fits where the Gaussian width was >= 400 nm. The signal-to-noise ratios were calculated using the local background calculation and the integrated spot intensity, and fits where this ratio was not >= 5 were discarded. Average intensites were then calculated from the first 10 good spot fits from the track to avoid measuring the effect of photobleaching of the motors.

2.13 Microscopy

2.13.1 TIRF microscopy

TIRF microscopy was performed with a Olympus TIRF system using a ×100 NA 1.49 objective, 488, 561 and 640 nm laser lines, an ImageEM emCCD camera (Hamamatsu Photonics) under the control of xCellence software (Olympus), with an environmental chamber maintained at 25 °C (Okolab, Ottaviano, Italy). Emission resulting from illumination with 488 or 561 nm laser lines was filtered by bandpass filters controlled by a filter wheel (Olympus) to avoid bleedthrough.

2.13.2 Widefield microscopy

Live cells were imaged using a ×60 oil NA 1.4 objective on an Olympus Deltavision microscope (Applied Precision, LLC) equipped with GFP and mCherry filter sets, and a CoolSNAP HQ2 camera (Roper Scientific) under the control of SoftWorx (Applied Precision). The environment was maintained at 37 °C and 5 % CO2 using a stage-top incubator (Tokai Hit) and a weather station (Precision control).

2.14 Statistical analyses, data plotting and figure preparation

Statistical analyses were performed in Python with use of the following modules: `scipy` (Virtanen et al., 2020) and `scikit-posthocs`. All statistical analyses were performed as follows. The data were tested to see if they followed a normal distribution using D'Agostino and Pearson's test. If data were normally distributed, pairwise interactions were tested using a two-tailed t-test for independent samples, and the resulting p-values were corrected for multiple comparisons if necessary. Where t-tests have been used, this is indicated in the figure legend; otherwise all statistical analyses relate to the following non-parametric testing process. If one or more experimental groups were not normally distributed, a Kruskal-Wallis H test was used to determine if any of the medians of the experimental groups differed. If the Kruskal-Wallis H test showed that one group was significantly different, then pairwise interactions were tested using Conover's post-hoc test. The p-values of these pairwise interactions were corrected for multiple comparisons.

Data were plotted using `matplotlib` (Hunter, 2007), and superplots were created with a custom made extension to `matplotlib`. Graphs were edited in Adobe Illustrator (Adobe), where modifications were limited to colours, line widths, spacing and text size.

Microscopy images were prepared in FiJi (Schindelin et al., 2012). Image manipulations were limited to scaling of contrast (between minimum and maximum values), and displaying images with different colour lookup tables. Where images from the same experiment are displayed alongside one another, their contrast is scaled equally.

Chapter 3

Hook3 activates KIF1C by releasing its autoinhibition

3.1 Investigation of KIF1C stalk-motor interaction

Previous data from our lab had identified KIF1C's stalk region (623-825) as being important in its intramolecular autoinhibiton. In fact, intramolecular cross-linking analyses had shown that the stalk region makes contact with the motor domain of KIF1C, and that this could be a potential mechanism whereby KIF1C is able to occlude its microtubule binding site and thus become autoinhibited (Siddiqui, 2018; Siddiqui et al., 2019). To directly test whether binding of KIF1C motor domains to the stalk domain is able to prevent microtubule binding, we cloned, expressed and purified KIF1C motor and stalk domains separately.

A motor-only construct was created by cloning a PCR product of KIF1C amino acids 1-349 with six amino acids of the kinesin-1 neck linker region attached to the end (encoding NTVSVN) into a pET22b vector containing a C-terminal GFP-6xHis tag. KIF1C stalk domain, corresponding to amino acids 612-922, was cloned into a modified pGEX-6P2 vector containing the addition of a tandem TEV protease recognition site after the GST tag. Each construct was expressed in BL21 (DE3) CodonPlus RIPL cells, and then purified in a one-step purification using either Ni-NTA or GSH resins (see Figure 3.1 a-d.).

To test the interaction of motor and stalk domains directly, a technique called MST was employed which is able to detect differences in the dispersion of fluorescent molecules upon heating with an infrared laser (Wienken et al., 2010). This dispersion is dependent on diffusivity of the molecule, which
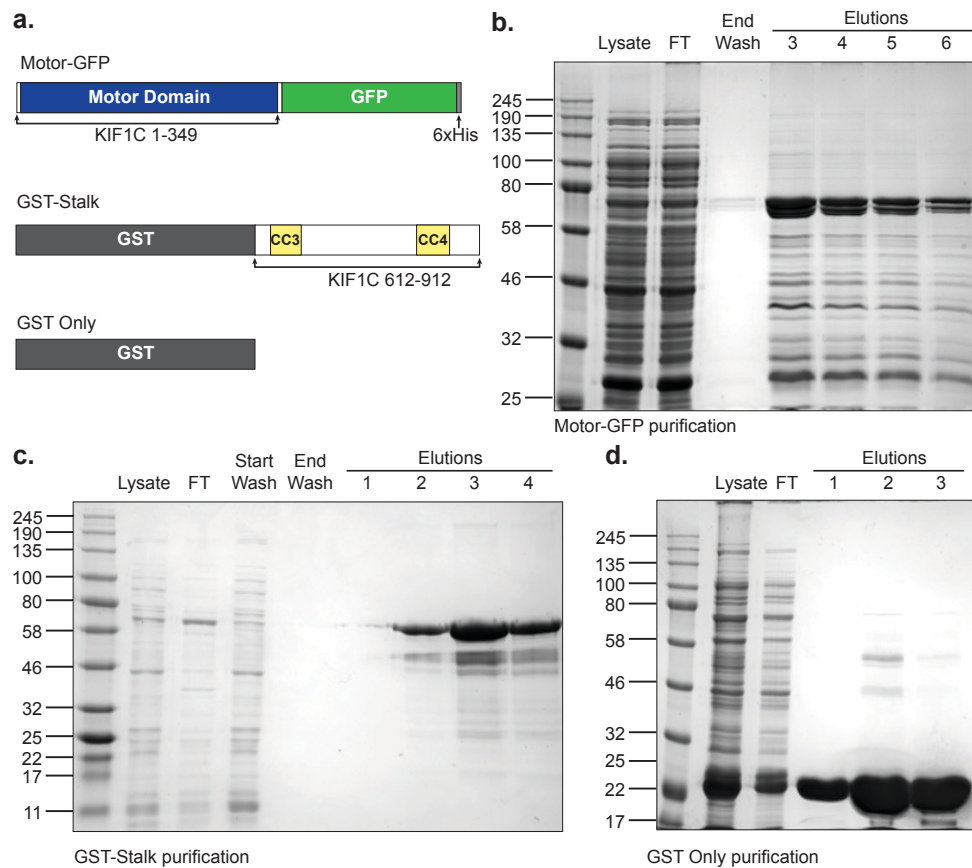
Figure 3.1: KIF1C motor and stalk construct purification | a. Schematics of KIF1C motor and stalk constructs, as well as GST-only control. KIF1C motor contains amino acids 1-349 of KIF1C which includes the minimal consensus sequence for the motor domain, and is tagged with a C-terminal GFP-6His tag. KIF1C stalk covers KIF1C amino acids 612-912 which includes coiled-coil domains 3 and 4 (CC3, CC4), and is tagged with an N-terminal GST tag. **b-d.** Acrylamide gels of purification of motor-GFP, GST-stalk and GST-only respectively. *Lysate* refers to cleared lysate following centrifugation, *FT* refers to flow-through, the unbound fraction after incubation with beads, *elutions* refer to fractions collected upon elution with either imidazole or glutathione.

a. 50nM motor-GFP + GST-stalk

K_d=0.94±0.20μM
K_d=0.97±0.17μM
K_d=1.00±0.16μM

b.

***

c. 4nM motor-GFP + 1μM GST   intensity   4nM motor-GFP + 1μM GST-stalk
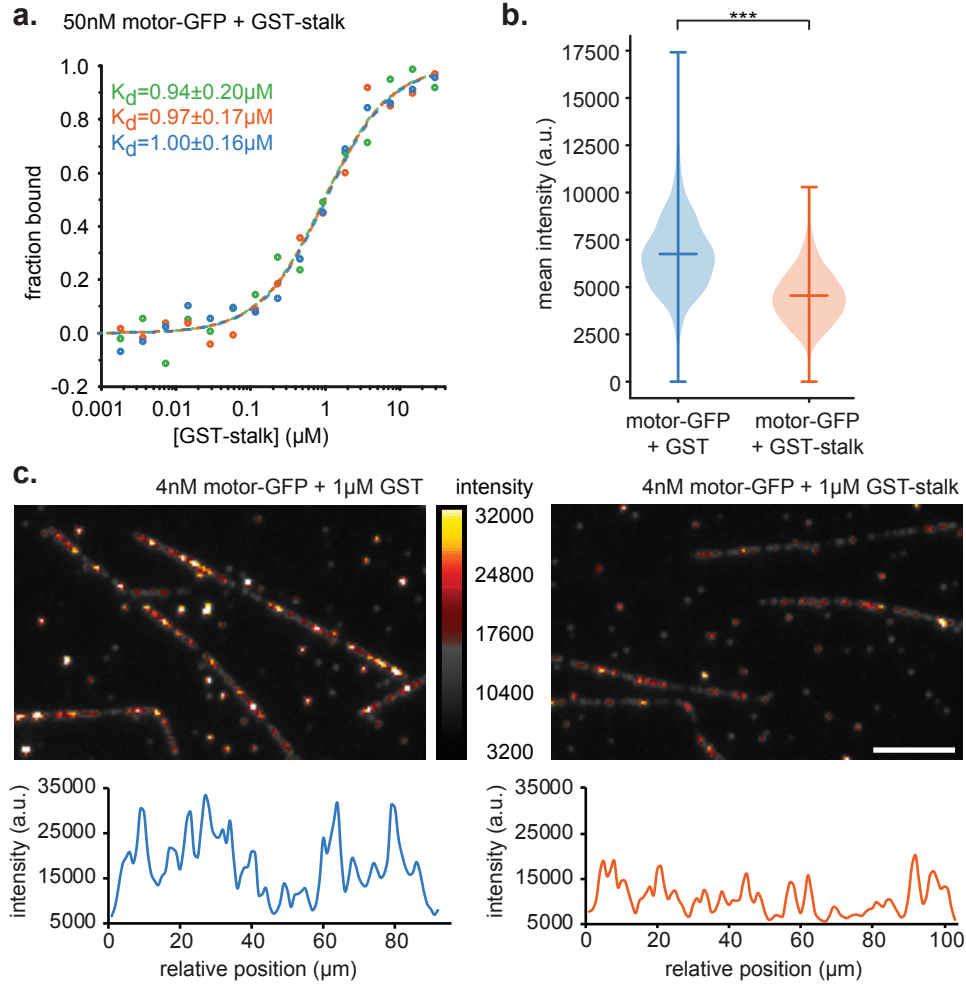
Figure 3.2: Measurement of KIF1C motor and stalk interaction by MST and TIRF | a. microscale thermophoresis (MST) was measured for 50 nM motor-GFP in the presence of varied concentrations of GST-stalk, and the K_d was found to be 1 μM. **b-c.** The intensity of motor-GFP on microtubules in total internal reflection fluorescence (TIRF) chambers was measured in the presence of 1 μM GST-stalk or 1 μM GST, where **b.** shows a violin plot of background-corrected microtubule intensities, and **c.** shows example traces of microtubules in each condition. *** indicates p = 10^{-99} (*t-test*).

53

changes when the molecule is in a complex, for example when two proteins bind to each other. Motor-GFP was added at a fixed concentration of 50 nM, while KIF1C stalk domain was added as two-fold serial dilution series from 29.6 µM to 903 pM, and the MST was measured to reveal the binding affinity of the stalk-motor interaction. The experiment was repeated three times, a K_d model was fitted to each curve and K_d was found to be around 1 µM (see Figure 3.2 a.).

Having revealed that these two parts of KIF1C are able to bind to one another directly, we next investigated whether this had the hypothesised effect of preventing the motor domain from binding to microtubules. Flow chambers were prepared with biotin-labelled, Taxol-stabilised GDP microtubules, and then 4 nM motor-GFP was added, either in the presence of 1 µM GST-stalk, or 1 µM GST as a negative control. The intensity of motor-GFP on micro-tubules was measured and corrected against the background, revealing that the addition of GST-stalk decreased motor-GFP intensity on microtubules to 67 ± 29% of control values, consistent with the stalk being able to prevent the motor domain from binding to the microtubule (see Figure 3.2 b-c.).

3.2   Identification of KIF1C stalk interactors

The interaction of KIF1C stalk and motor domains provided strong evidence for KIF1C's auto-inhibitory mechanism, but inside cells there must be a way to release this autoinhibiton to activate KIF1C. We hypothesised that any protein that was capable of binding specifically to the stalk region of KIF1C would have the ability to prevent the stalk from inhibiting the motor protein, and would therefore act as an activator. Therefore we sought to identify proteins that interact specifically with the stalk region in the context of the full length motor protein.

To identify KIF1C-stalk interactors, we utilised BioID which is a proximity-based labelling technique whereby the BioID-tagged bait protein within the cell is able to catalyse the addition of biotin to any proteins it comes into contact with (Kim et al., 2016; Roux et al., 2012). To specifically identify interactions that occur in the stalk region of KIF1C, we made two constructs of KIF1C tagged with a BioID2 tag: full-length KIF1C (KIF1C-FL-BioID2), and KIF1C-Δ623-825 (KIF1CΔS-BioID2) where the stalk region of the protein was removed. In both cases, the BioID2-HA tag was added to the C-terminus of KIF1C. We hypothesised that the differences in proteins that were biotiny-

lated with KIF1C-FL-BioID2 versus those that were biotinylated with KIF1C-ΔS-BioID2 would allow the detection of interactions that occur specifically in the stalk region.

RPE1 cells were transfected with BioID constructs, and left for 24 hours before supplementing growth media with 20 µM Biotin. The expression of the bait protein, as well as the amount of biotinylated proteins, was monitored with western blotting (see Figure 3.3 a-b.). From this we concluded 12 hours of biotin supplementation was sufficient. We then performed three experimental repeats comparing KIF1C-FL-BioID2 to KIF1C-ΔS-BioID2, including one experiment that was done in triplicate, and in each case the enrichment of bait and target proteins on streptavidin beads was monitored by western blotting (see Figure 3.3 c.). Enriched proteins were digested from streptavidin beads with trypsin, and then subjected to tandem mass spectrometry.

Tandem mass spectrometry data were processed using MaxQuant to identify and quantify peptide data against the human proteome. Data from multiple experiments were combined into experimental groups in the mass spectrometry analysis package Scaffolds, and a Fishers Exact T-test with Benjamini–Hochberg correction was applied, which resulted in a significance threshold of 0.0019 for a 5% false-discovery rate. Using these criteria, 45 proteins were found to be enriched above the false-discovery cutoff. 11 of these were more enriched in the KIF1C-ΔS-BioID2 sample, while the remaining 34 were enriched in the KIF1C-FL-BioID2 sample, indicating that they may require the KIF1C stalk for their interaction (see Figure 3.4). The most significantly enriched protein was Hook3, a dynein adaptor protein (see Table 3.1).
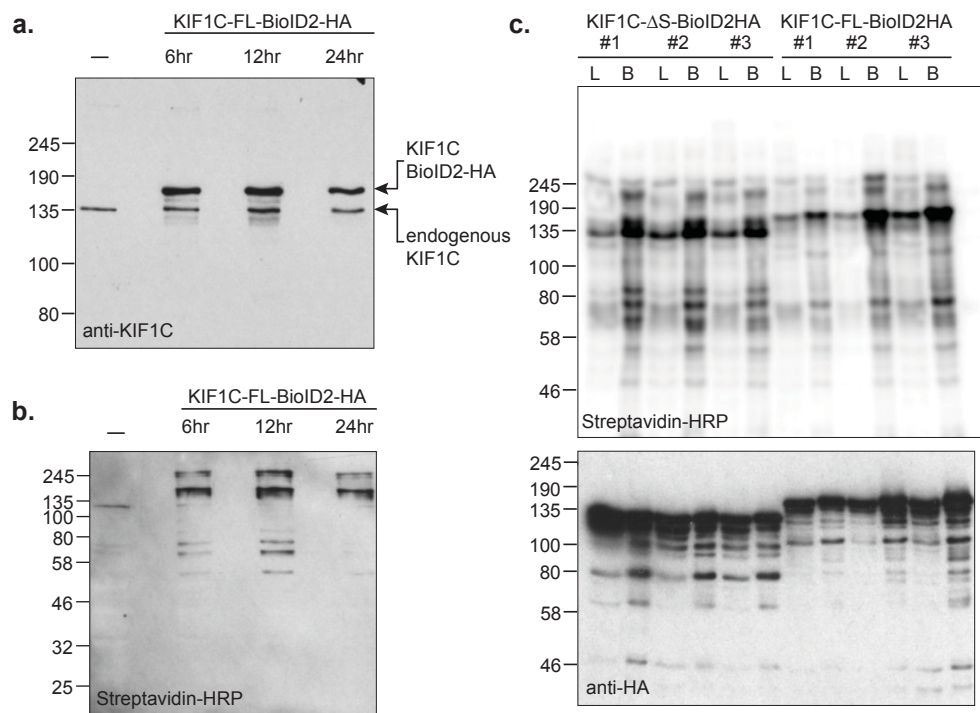
Figure 3.3: KIF1C BioID Time-course and verification of pulldown efficiency | a-b. Time-course of RPE1 cells transfected with KIF1C-FL-BioID2-HA, where cells were transfected and then exchanged into media containing 20 µM Biotin for the indicated time before being harvested, compared to a negative control (-) which received no transfection but still received biotin supplementation for 12 hours. **a.** shows recombinant protein levels detected with KIF1C antibody, while **b.** shows the same samples probed with streptavidin-HRP to show biotinylated proteins. **c.** Blots of triplicate experiments for KIF1C-ΔS-BioID2-HA and KIF1C-FL-BioID2-HA probed both for biotinylated proteins and recombinant protein levels. *L* indicates sample of cell lysate, *B* indicates a proportional amount of beads after pulldown of biotinylated proteins. In each case, enrichment of the biotinylated proteins on beads can be seen.

56
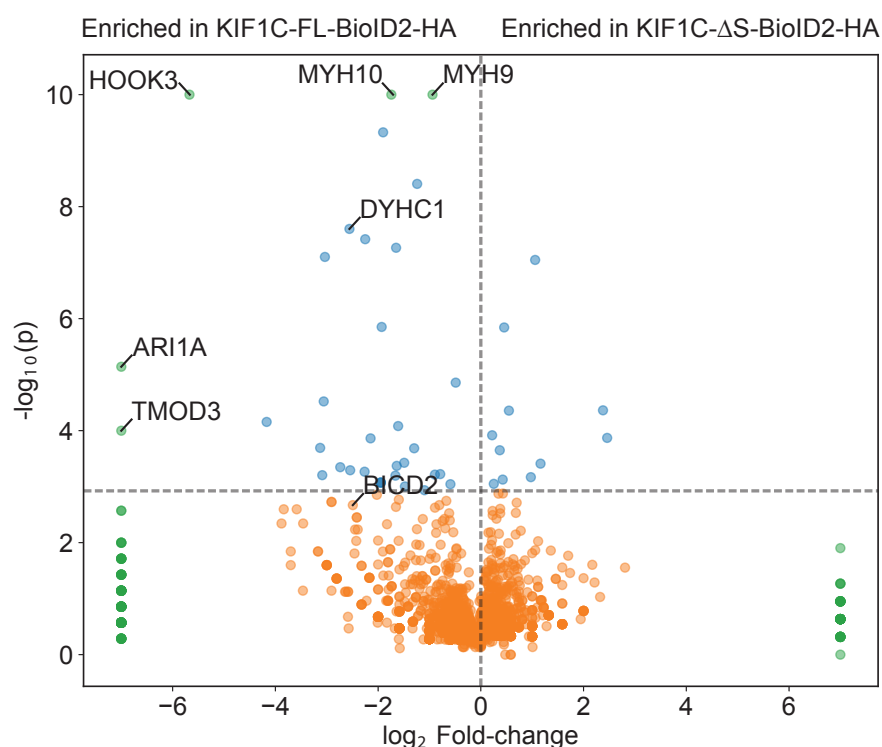
Figure 3.4: BioID hits for KIF1C-FL-BioID vs. KIF1C-ΔS-BioID Volcano plot showing the distribution of identified proteins from a KIF1C BioID screen performed with KIF1C-FL-BioID vs. KIF1C-ΔS-BioID (where a region corresponding to amino acids 623-825 is deleted). The horizontal dotted line indicates the multiple-corrections corrected significance threshold for a 5% false-discovery rate, whereas the vertical line indicates the location of equal abundance between the two experiments. Blue dots indicate those hits above the false-discovery rate, while orange dots are those below it. Green dots are those who have had either their enrichment or statistical significance capped to fit within the plot, for example, if a protein exists in only one sample it will be infinitely enriched. Several potentially interesting hits have been identified with their gene names, the full list of identified proteins is in Table 3.1.

Gene	Fold enrichment in FL	p-value
TMOD3_HUMAN	128.00	1.00×10^{-04}
ARI1A_HUMAN	128.00	7.22×10^{-06}
HOOK3_HUMAN	51.00	1.00×10^{-10}
E9PDF6_HUMAN	18.00	6.99×10^{-05}
CON__P04259	8.74	2.03×10^{-04}
CAND1_HUMAN	8.50	6.24×10^{-04}
GCN1_HUMAN	8.33	3.01×10^{-05}
F5H6E2_HUMAN	8.20	7.91×10^{-08}
EFTU_HUMAN	6.67	4.49×10^{-04}
DYHC1_HUMAN	5.89	2.50×10^{-08}
TPM1_HUMAN	5.83	5.10×10^{-04}
COPB_HUMAN	4.80	5.41×10^{-04}
RBP2_HUMAN	4.76	3.82×10^{-08}
RAGP1_HUMAN	4.43	1.37×10^{-04}
ENSBTAP00000031900	3.86	8.46×10^{-04}
GLYR1_HUMAN	3.86	8.46×10^{-04}
GSLG1_HUMAN	3.86	8.46×10^{-04}
A0A0C4DGG9_HUMAN	3.81	1.41×10^{-06}
K1C16_HUMAN	3.74	4.71×10^{-10}
MYH10_HUMAN	3.35	1.00×10^{-10}
PFKAP_HUMAN	3.17	6.37×10^{-04}
PRKDC_HUMAN	3.14	5.43×10^{-08}
K1C17_HUMAN	3.11	4.26×10^{-04}
MYL6_HUMAN	3.05	8.28×10^{-05}
COPA_HUMAN	2.81	3.75×10^{-04}
TCPD_HUMAN	2.79	9.91×10^{-04}
ML12B_HUMAN	2.46	2.06×10^{-04}
PLEC_HUMAN	2.36	3.92×10^{-09}
ZN638_HUMAN	2.14	1.16×10^{-03}
MYH9_HUMAN	1.92	1.00×10^{-10}
ACTG_HUMAN	1.86	6.10×10^{-04}
KI67_HUMAN	1.73	5.97×10^{-04}
IQGA1_HUMAN	1.51	9.04×10^{-04}
ACACA_HUMAN	1.40	1.39×10^{-05}
E9PGC8_HUMAN	-1.16	1.21×10^{-04}
CE170_HUMAN	-1.19	8.91×10^{-04}
A0A024R4E5_HUMAN	-1.29	2.24×10^{-04}
PABP1_HUMAN	-1.34	7.48×10^{-04}
E7EVA0_HUMAN	-1.37	1.44×10^{-06}
SRC8_HUMAN	-1.46	4.39×10^{-05}
A0A1B0GUI1_HUMAN	-1.96	6.77×10^{-04}
MTAP2_HUMAN	-2.08	8.94×10^{-08}
A0A1B0GUA3_HUMAN	-2.24	3.89×10^{-04}
EP15R_HUMAN	-5.20	4.33×10^{-05}
EPS15_HUMAN	-5.50	1.35×10^{-04}

Table 3.1: Mass spectrometry data of significantly enriched proteins in KIF1C-FL and KIF1C-ΔS BioID samples

3.3   Interaction of KIF1C with dynein adaptor proteins

From our BioID experiment, we identified Hook3 as a strong interactor of KIF1C inside cells. We also found BICD2 at a level below the significance threshold applied, while another dynein adaptor, BICDR1, was not found despite evidence from the literature showing an interaction with KIF1C (Schlager et al., 2010). When consulting published RNA sequencing data of RPE1 and U2OS cells, we found that BICD2 and BICDR1 are transcribed in levels much lower than Hook3, and so we could not entirely rule out an interaction with KIF1C on the results of our BioID experiment alone (see Table 3.2).

To verify whether these adaptors had an effect on kinesin-driven transport in cells, we made short hairpin RNA (shRNA) plasmids based on verified and published oligonucleotide sequences, and transfected a Neuropeptide-Y (NPY)-expressing RPE1 cell line with these to deplete either Hook3, BICD2 or BICDR1. NPY is a cargo of KIF1C in neurons, and has also previously been used as a BICDR1/KIF1C dependent cargo marker in non-neuronal cells (Schlager et al., 2010; Siddiqui et al., 2019). Depleting BICD2 and BICDR1 lead to an inhibitory effect on the trafficking of NPY vesicles away from the perinuclear region, suggesting an inhibitory effect on the action of kinesin-driven transport (see Figure 3.5 a.).

We next sought to answer whether the opposite was true; if increasing the concentration of the adaptor proteins inside the cells would have a kinesin-activation phenotype. Therefore, Hook3, BICD2 and BICDR1 were cloned into mammalian expression plasmids from a human cDNA library and tagged at the C-terminus with GFP. When these constructs were transfected into the same NPY-expressing RPE1 cell line, vesicles crowded towards the periphery of the cell, indicative of a kinesin-activation phenotype (see Figure 3.5b.). This could also be an effect of dynein being sequestered at the centrosome as it may become hyper-activated by the abundance of dynein adaptor.

Adaptor	RPE1 RNA count	% of Hook3	U2OS RNA count	% of Hook3
Hook3	76,438 +/- 8,834	100%	26,232 +/- 7,000	100%
BICD2	26,116 +/- 2,324	34%	15,417 +/- 7,312	59%
BICDR1	240 +/- 341	0.3%	1,904 +/- 1,410	7.2%

Table 3.2: Relative gene counts for Hook3, BICD2 and BICDR1 taken from the control transcriptomics data from Jenal et al. (2012) with accession ID SRP007596.
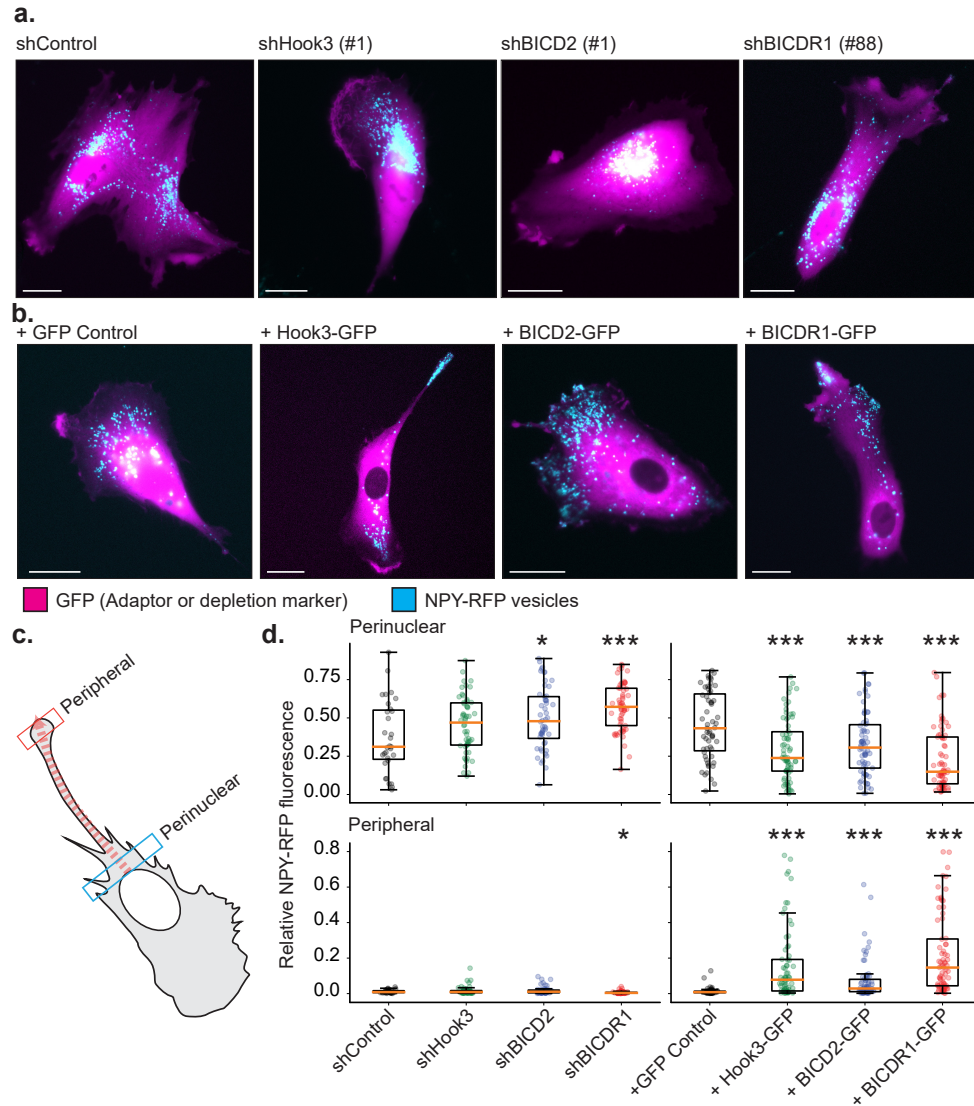
Figure 3.5: Effect of depletion and expression of Hook3, BICD2 and BICDR1 on NPY-RFP vesicle distribution | a. NPY-RFP expressing RPE1 cell line, treated with shRNAs against control (luciferase), Hook3, BICD2 and BICDR1. Magenta shows GFP signal which marks cells that have been transfected with the depletion plasmid, while cyan shows the NPY-RFP vesicles. **b.** NPY-RFP cells expressing Hook3-GFP, BICD2-GFP and BICDR1-GFP shown in magenta. **c.** Schematic of analysis of NPY-RFP distribution. **d.** Analysis of distribution of NPY-RFP vesicles when depleting or overexpressing each adaptor protein, where each point represents one cell. All scale bars are 20 μm. Statistical testing was from a KruskalWallis Htest followed by a Conover's posthoc test to evaluate pairwise interactions with a multiplecomparison correction applied using the Holm–Bonferroni method. * = p < 0.05, ** = p < 0.01, *** p < 0.001.

To quantify the effect of these adaptors on NPY-RFP vesicle distribution, we measured fluorescent signal of NPY-RFP vesicles in cells along a line between the edge of the nucleus and the furthest excursion of the cell, following the cell's main axis (see Figure 3.5c.). The lengths of cells differed, and so for the purpose of this analysis we normalised the length of the measured region between 0 and 1, and further sub-classified the region between 0.15-0.25 as being perinuclear, typically where microtubule minus-ends would be located, while 0.9-1.0 was defined as peripheral where microtubule plus-ends would more often be found. From this analysis, we confirmed that depleting adaptor proteins had a small effect in NPY-RFP vesicle localisation in the perinuclear region, while depletion of BICDR1 also showed a decrease in peripheral localisation of NPY-RFP vesicles (see Figure 3.5 d.). A much larger change was observed when over-expressing each adaptor. Hook3, BICD2 and BICDR1 all caused a significant decrease in perinuclear localisation of NPY-RFP vesicles, and a corresponding increase in the peripheral localisation (see Figure 3.5d.). Thus it appeared that all three adaptors were possible kinesin activators, as depletion of BICD2/BICDR1 causes a kinesin inactivation phenotype while over-expression of either Hook3, BICD2 or BICDR1 appears to cause a kinesin hyper-activation or dynein inhibition phenotype, driving vesicles to the periphery.

Importantly in these experiments, it is not clear which kinesin is being activated due to the complexity of the cell and the redundancy of kinesins. Each cargo being observed may have several different types of kinesin present, and so the effect cannot be ascribed exclusively to KIF1C. Kinesin depletion phenotypes are often mild and compensated for, meanwhile attempts to localise specific fluorescently-labelled kinesins to cargoes in a cellular context fail due to the small number of kinesins on each cargo not providing sufficient signal. For this reason, given that all the dynein adaptors we tested had some effect on kinesin-driven transport, we decided to purify the adaptor proteins and KIF1C to see if they interact directly *in vitro*.

Purification of full-length 6xHis-KIF1C-GFP from *Spodoptera frugiperda* (Sf9) insect cells was already established within our group, and involves a two-step purification, first utilising ion-exchange with Sulfopropyl (SP) cation exchange sepharose, and then affinity purification with Ni-NTA resin. The author further modified this protocol by increasing scale, as well as including 200 mM Trimethylamine N-oxide (TMAO) as a crowding reagent in the final elution for storage purposes, as it had been

61

reported to stabilise kinesins in the literature (see Figure 3.6) (Chase et al., 2017).

Full-length human BICDR1, Hook3 and BICD2 were cloned into pFast-Bac baculovirus transfer vectors with an N-terminal 8xHis-ZZ-LTLT tag (where ZZ refers to the IgG-binding protein A tag, and LTLT refers to a tandem TEV protease cleavage site), and C-terminal SNAPf enzymatic tag for covalent modification of the proteins. We first scouted the optimal binding and washing conditions for these constructs during Ni-NTA purification by incrementally increasing imidazole concentration and observing when the protein is eluted from the beads. We found that all of the 8xHis tagged adaptors behaved identically, where washing was tolerated up to around 80 mM imidazole, while elution typically occurred after 200 mM (see BICD2 as example Figure 3.7a.), therefore 60 mM was chosen as the washing concentration and 300 mM was chosen as the elution concentration. The ZZ tag was used as a second step purification of proteins eluted from Ni-NTA resin. Ni-NTA elutions were pooled and bound to IgG sepharose, at which point the protein could be labelled by adding the SNAPf substrate (typically BG-Alexa647), then the beads were washed and incubated with TEV protease overnight to elute the protein. Under these conditions we found that binding of the adaptors to the IgG sepharose was inefficient, but was sufficient to yield reasonable amounts of pure protein (again, BICD2 is shown as an example see Figure 3.7 b.).

After optimising purifications for KIF1C-GFP and Alexa-647 tagged dynein adaptors, we next sought to investigate their motility along microtubules using TIRF microscopy. Our lab had previously elaborated that KIF1C-GFP alone is a fast processive dimer in single molecule assays. To answer whether BICDR1, BICD2 and Hook3 are able to form an interaction with KIF1C-GFP, we incubated the two proteins together and then flowed them into a TIRF chamber. We found that BICD2 and BICDR1 very rarely appear to colocalise and co-transport with KIF1C, whereas Hook3 frequently co-localised with KIF1C (see Figure 3.8a-c.). Thus Hook3 is a bona fide interactor of KIF1C and can be co-transported along the microtubule by KIF1C, while BICDR1 and BICD2 do not interact efficiently with KIF1C and may require additional proteins that aren't available in this reconstituted system.
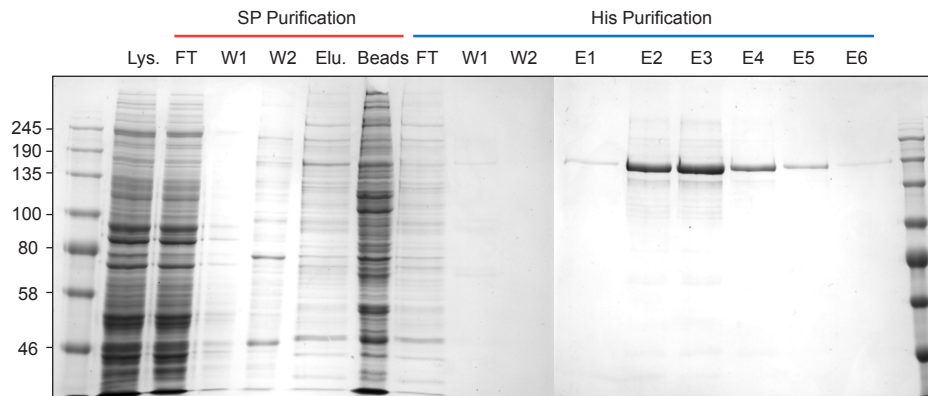
Figure 3.6: Two-step purification of KIF1C-GFP | a. Example purification of KIF1C-GFP from Sf9 cells. *FT:* flow-through/unbound fraction, *W:* wash, *E:* elution, *B:* beads.
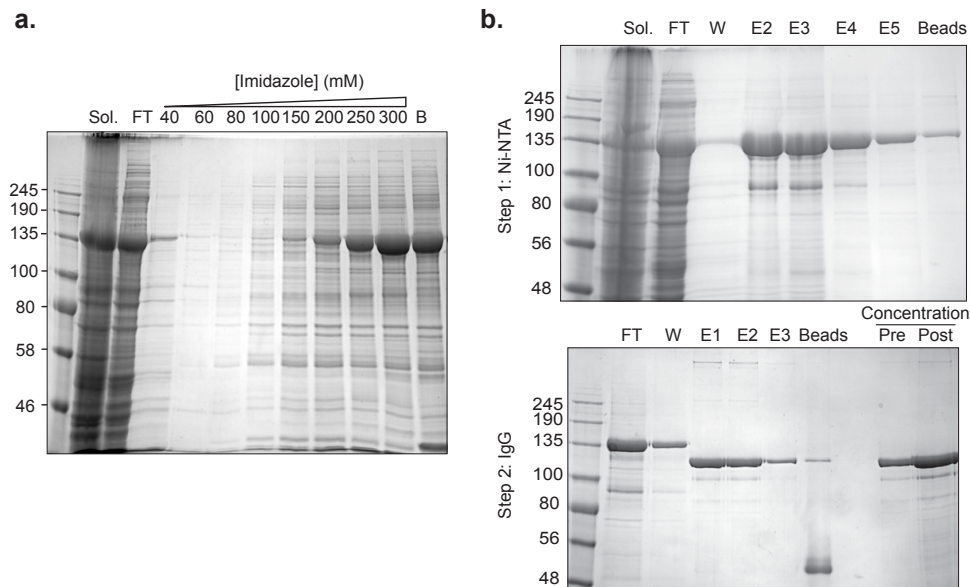
Figure 3.7: Two-step purification of dynein adaptor proteins | a. Example optimisation of 8xHis tag for 8xHis-ZZ-LTLT-BICD2-SNAPf where imidazole concentration is increased sequentially to find the optimal washing and elution conditions. The elution pattern was identical for Hook3 and BICDR1. **b.** Example of the two-step purification of BICD2 after deciding on optimal washing in Ni-NTA step as 60 mM imidazole and elution of 300 mM imidazole. Protein eluted from Ni-NTA was subsequently purified using IgG sepharose, and was cleaved off of beads using TEV protease. The protein was then concentrated. *FT:* flow-through/unbound fraction, *W:* wash, *E:* elution, *B:* beads.
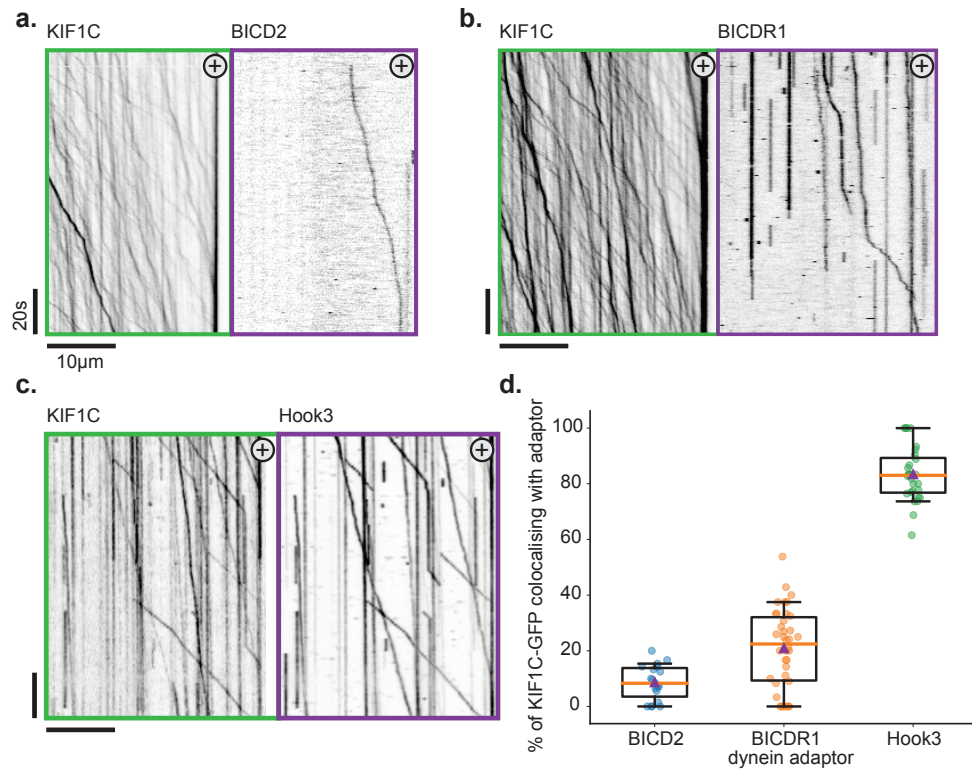
Figure 3.8: KIF1C co-transports with Hook3 but rarely with BICD2 and BICDR1 | TIRF microscopy of 4.5 nM KIF1C-GFP in the presence of 40 nM BICD2 (**a.**), 40 nM BICDR1 (**b.**) or 2nM KIF1C-GFP in the presence of 20 nM Hook3 (**c.**). Each adaptor protein is labelled to a similar proportion ($\geq$80%). The proportion of KIF1C-GFP motors that co-localised with dynein adaptor signal was quantified in **d.**, showing that Hook3 forms a strong interaction with KIF1C and is co-transported. The plus-end of the microtubule is indicated by a +. Scale bars are 20s (vertical) and 10s (horizontal) in all images.

3.4   Activation of KIF1C by Hook3

As Hook3 was such a strong interactor of KIF1C, we next asked whether this interaction had any effect on KIF1C's motility. For example, dynein adaptors increase both speed and processivity of dynein, while MAP7 interacts with kinesin-1 to increase its landing-rate, speed and processivity (Hooikaas et al., 2019; Urnavicius et al., 2018). Therefore we investigated all of these characteristics for KIF1C in the presence and absence of Hook3.

The presence of Hook3 did not significantly alter the speed or run length of KIF1C-GFP (see Figure 3.9 a-c.). However, the landing rate of KIF1C was more than doubled in the presence of Hook3 (from 0.125 ± 0.048 motors.μm^{-1}.min^{-1} to 0.266 ± 0.095 motors.μm^{-1}.min^{-1}; see Figure 3.9 d.), consistent with Hook3 releasing the autoinhibition of the motor protein and allowing it to engage the microtubule.

To confirm our understanding of the activation of KIF1C, we purified KIF1C-ΔS-GFP from Sf9 cells and compared its motility on microtubules with wildtype KIF1C. The landing rate of KIF1C-ΔS-GFP was increased 20-fold in comparison to wildtype showing it lacks the autoinhibition of the full-length motor protein, and also had increased speed compared to wildtype motor (see Figure 3.10 a-d.). Consistent with our stalk-dependent model of Hook3 interaction, KIF1C-ΔS-GFP no longer efficiently formed complexes with Hook3-647, as could be seen by a lack of Hook3-647 co-transport with KIF1C-ΔS-GFP (see Figure 3.10 e-f.).

3.4.1   Summary

We found that purified KIF1C motor and stalk domains interact with a K_d of 1 µM, and that this interaction prevents the motor gaining access to the microtubule, thus inhibiting it. From a BioID screen, we identified Hook3 and BICD2 as potential regulators of this process, and cellular evidence showed that Hook3, BICD2 and BICDR1 have effects on NPY-vesicle transport which could be due to kinesin activation. Using purified proteins *in vitro*, we found Hook3, but not BICD2 or BICDR1, efficiently interacts with KIF1C. Hook3 is able to relieve KIF1C's autoinhibiton and allows it to become activated. The stalk region of KIF1C is essential for this interaction as removal of this region negates the Hook3 interaction. Thus Hook3 may be the dynein adaptor which permits simultaneous interaction with KIF1C and dynein to allow bidirectional transport to occur.
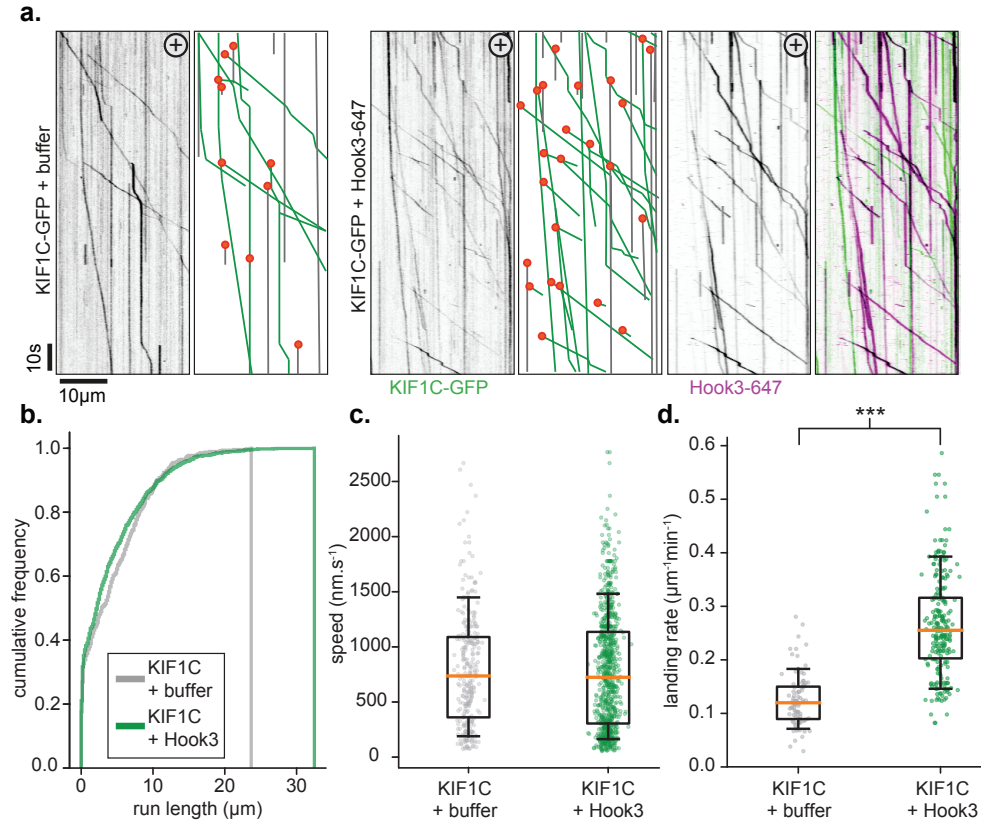
Figure 3.9: KIF1C is activated by the dynein adaptor Hook3 | a. Representative kymographs of 2 nM KIF1C-GFP in the presence of 20 nM Hook3-647 or buffer control, where landing motors are highlighted with orange circles, and their tracks are highlighted by green lines. **b.** Cumulative frequency of the run lengths of KIF1C-GFP in the presence or absence of Hook3 reveals the two classes of motor run similar distances. **c.** Box-plot of KIF1C-GFP speeds in the presence of Hook3-647 or buffer control, where each spot represents a single motor showing the speed is unaltered by the addition of Hook3. **d.** Box-plot of KIF1C-GFP landing frequency on microtubules in the presence of Hook3-647 or buffer control, where each dot represents one microtubule, showing that the landing rate increased in the presence of Hook3-647. *** indicates significant difference of 6.0×10^{-33} from two-tailed t-test
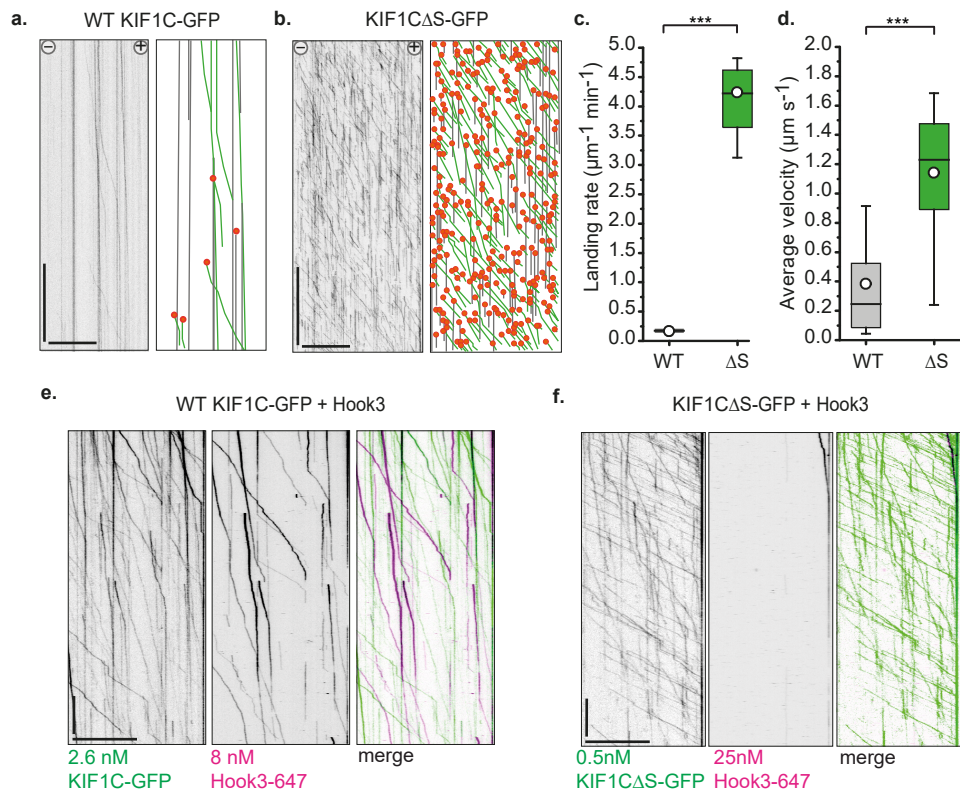
Figure 3.10: KIF1C-ΔS is hyperactive and no longer efficiently co-transports Hook3-647 | a-b. Representative kymographs of equal concentrations of of wildtype or ΔS KIF1C-GFP where landing events are indicated with orange circles, immotile tracks are indicated with a grey line, and motile tracks are indicated with a green line. **c.** Quantification of landing rate increase. **d.** Quantification of velocity increase. **e-f.** Representative kymographs of wildtype or ΔS KIF1C-GFP in the presence of Hook3-647, showing that KIF1C-ΔS-GFP rarely co-transports Hook3-647 molecules. Scale bars are 20 s in the vertical axis, 20 μm in the horizontal axis. *** represents p < 0.001 from a two-tailed t-test.

Chapter 4

KIF1C-driven bidirectional transport in cells

4.1 Inhibitable KIF1C

We next sought to test whether KIF1C and dynein's functionalities were interlinked within the cell, as although we had found Hook3 interacted strongly with KIF1C, it was uncertain whether it interacted with dynein at the same time. To test the short-term behaviour of KIF1C we developed an acutely inhibitable form of the full-length motor protein by addition of a DmrB domain to the N-terminus of the protein based on the principle developed by the Verhey lab for kinesin-1 and KIF1A (Engelke et al., 2016). The DmrB domain, based on the FKBP/FRB system, homodimerises in the presence of B/B homodimeriser (AP20187), thereby holding the two motor domains of the kinesin together (see Figure 4.1 a.). This had previously been shown to be successful in reducing KIF1A's functionality (Engelke et al., 2016). The Verhey lab had found that the number of amino acids between the homodimerisation domain and the N-terminus of the kinesin needed to be optimised to retain function of the kinesin while maximising inhibition upon addition of the dimerising drug (see Figure 4.1 b.).

In designing DmrB-KIF1C, we made constructs with 1, 2 or 3 amino acids deleted at the N-terminus of KIF1C (Δ1-3 respectively) with a C-terminal GFP tag. As KIF1C is a dimer, we reasoned that expression of DmrB-KIF1C could lead to heterodimers, and this could undermine the inhibition approach. To avoid this, these constructs were placed into pSuper plasmids which contained a shRNA targeting endogenous KIF1C but not the recombinant KIF1C
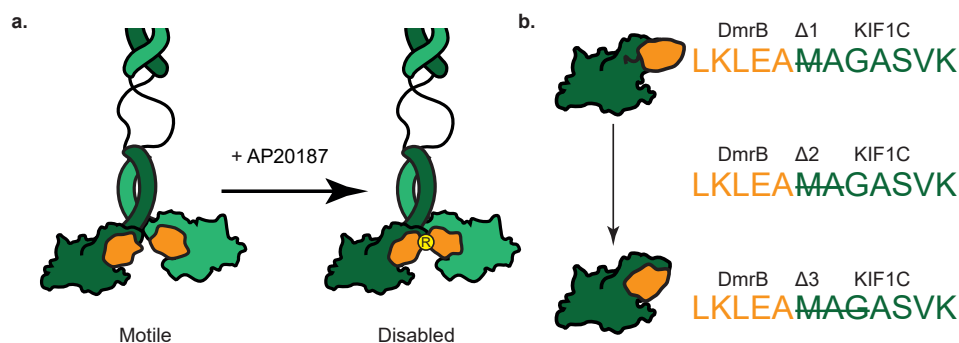
Figure 4.1: Schematic of DmrB acutely inhibitable KIF1C | a. Schematic showing how attachment of a DmrB homodimersation domain (orange) to the N-terminus of KIF1C can be used to inhibit the motors movement. Upon addition of AP20187, the DmrB domains homodimerise and constrict the movement of the kinesin motor domains. **b.** Linkage of DmrB to the N-terminus of KIF1C where sequential amino acids are removed to determine empirically which length leads to a maximally functional kinesin that is also sufficiently inhibited by dimerisation.

in our plasmid. Thus we could probe the activity of the recombinant KIF1C knowing that the transfected cells had a decreased level of wildtype KIF1C.

We first checked that these constructs localised as wildtype KIF1C should, accumulating at the periphery of cells primarily in tails, with occasionally a small amount of KIF1C-GFP visible at the centrosome. From microscopy images, as well as analysis shown later, it could be seen that while no construct exactly emulated wildtype KIF1C-GFP, Δ1 and Δ2 DmrB-KIF1C-GFP appeared to do so best (see Figure 4.2 a-d.).

To assay the inhibition of these KIF1Cs, AP20187 was added and cells were immediately imaged every minute for 18-20 minutes. DmrB-Δ2-KIF1C showed a clear pattern of inhibition. In the first few minutes, the intensity of the peripheral KIF1C would begin to decrease, and several minutes after this the signal of KIF1C at the centrosome would increase, suggesting that KIF1C was relocalised from the periphery to the centrosome (see Figure 4.3).

The inhibition was quantified by measuring the fold-intensity over background of the centrosomal and tail (or peripheral) portions of KIF1C, and comparing these values to those made after AP20187 had been added for 20 minutes (see Figure 4.4). From these data, it was confirmed that control cells do not appear to show any relocalisation of KIF1C to the centrosome or tail of cells upon the addition of AP20187. DmrB-Δ1-KIF1C-GFP did not show any signs of inhibition, while both Δ2 and Δ3 showed consistent inhibition by de-

a. KIF1C-GFP Control **b.** DmrB-Δ1-KIF1C-GFP **c.** DmrB-Δ2-KIF1C-GFP **d.** DmrB-Δ3-KIF1C-GFP
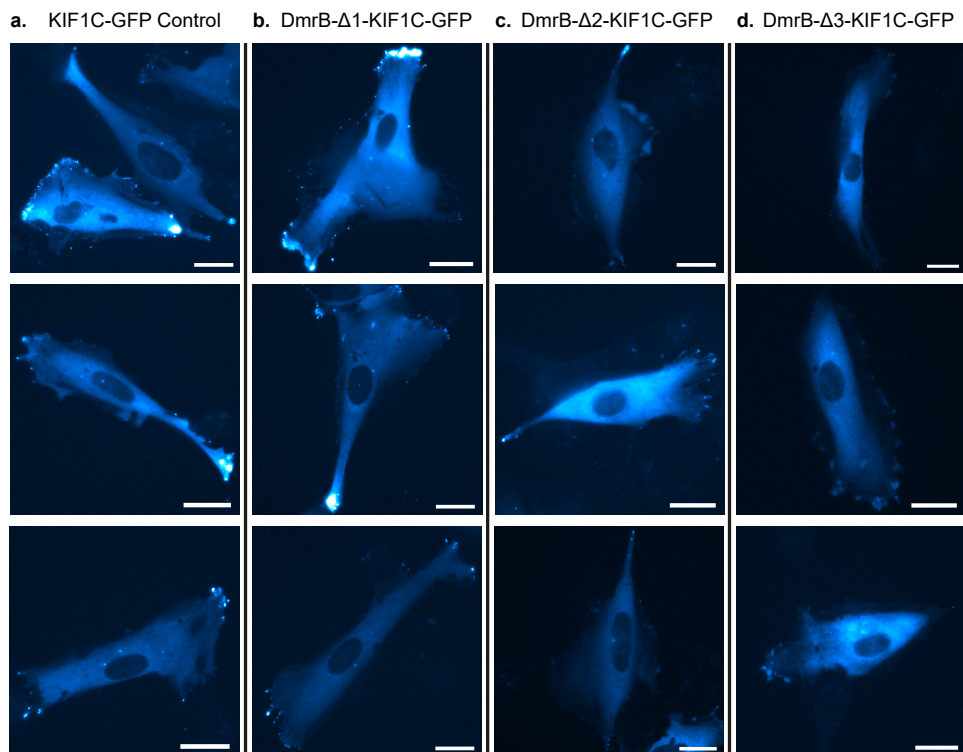
Figure 4.2: RPE1 cells transfected with different DmrB-KIF1Cs | The localisation of different DmrB-KIF1Cs is shown, where **a.** is a control KIF1C-GFP plasmid, and **b-d.** link DmrB to KIF1C by removing 1, 2 or 3 amino acids from the N-terminus of KIF1C. Scale bar is 20 μm.
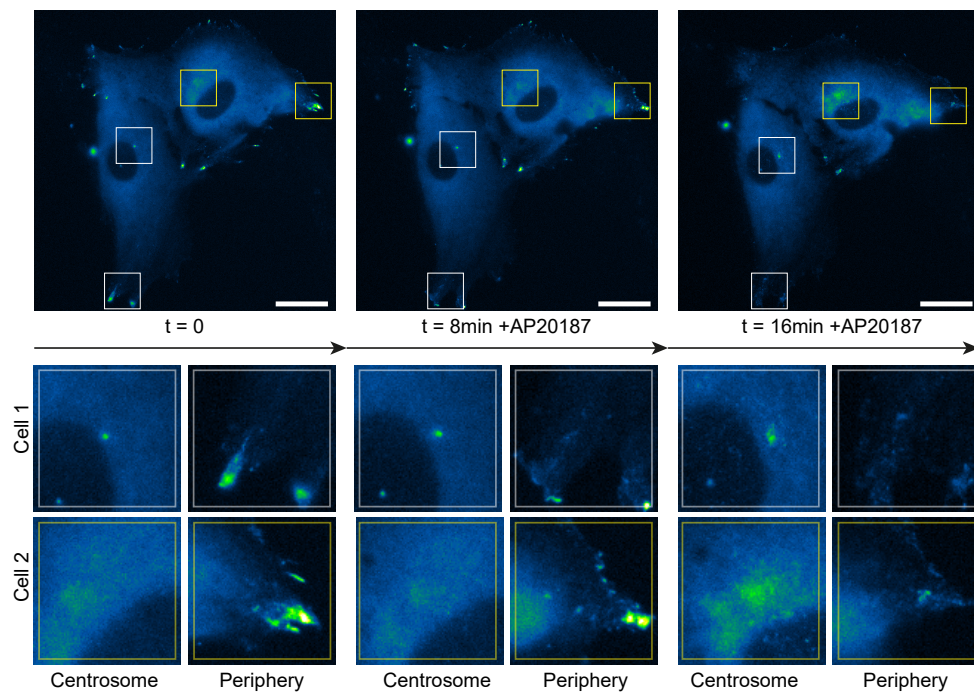
Figure 4.3: DmrB-Δ2-KIF1C-GFP inhibition and relocalisation | Two cells transfected with DmrB-Δ2-KIF1C-GFP are shown, with their centrosomal and peripheral regions enlarged. After addition of AP20187, KIF1C intensity can be seen to decrease at the periphery and start to increase at the centrosome, while after 16 minutes the majority of peripheral signal is relocalised to the centrosome. Scale bar is 20 μm.
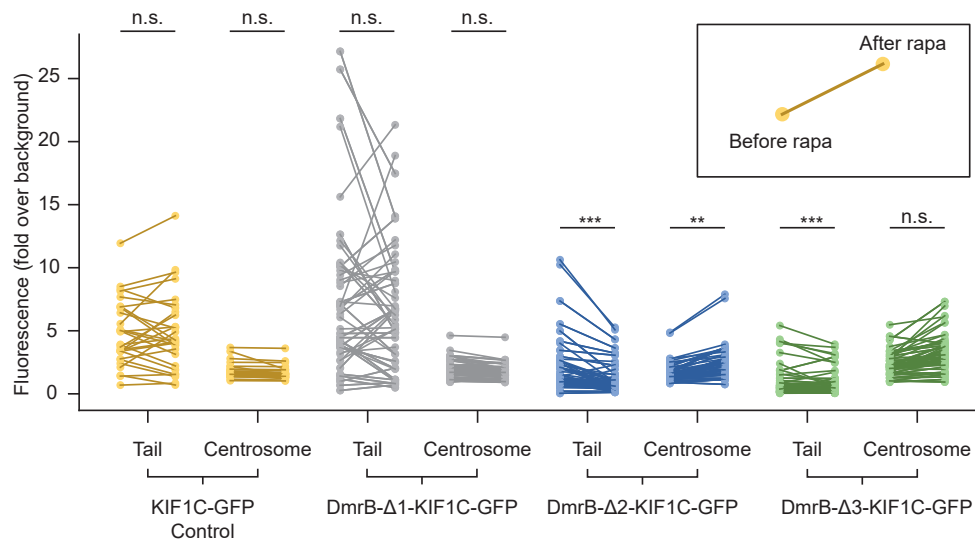
Figure 4.4: Quantification of DmrB-KIF1C-GFP relocalisation | Quantification of changes in centrosomal or tail accumulations of KIF1C-GFP in cells transfected with KIF1C-GFP or DmrB-Δ1, Δ2 or Δ3 KIF1C-GFP. The y axis shows fluorescence intensity in fold-difference as compared to locally calculated background. Each cell is shown as two dots linked by a line, where the left dot shows before AP20187 addition, and right shows after AP20187 addition. n.s. indicates $p > 0.05$, ** indicates $p \leq 0.01$, *** indicates $p \leq 0.00$ with a two-tailed T-test.

creased KIF1C signal in tails and increased KIF1C signal at the centrosome. During live recording of Δ2 inhibition, small punctate signals could be seen to move away from the tail and begin to appear near the nucleus. We interpreted this as KIF1C being transported from the periphery to the centrosome, and hypothesised that dynein most likely undertook this transport.

In summary, KIF1C does appear to be functionally interlinked with dynein on short timescales, and this motivates further investigation into the role of Hook3 in creating a co-complex of KIF1C and dynein. DmrB-Δ2-KIF1C is an attractive tool for investigating dynein and KIF1C interlinked transport within cellular systems, but optimal use of this tool likely requires CRISPR/Cas9-mediated knock-in of the DmrB domain on endogenous KIF1C.

4.2 Peroxisome sorting assay

Having identified Hook3 as the dynein adaptor which most strongly interacted with KIF1C, we next sought to understand more about how Hook3 works within cells. Do Hook3-driven cargoes undertake bidirectional transport? Do such cargoes rely on KIF1C as well as dynein within cells?

We adapted the peroxisome transport assay that had been used to target motors and dynein adaptors to primarily immotile peroxisomes (Kapitein et al., 2010). In our system, FRB was attached to full-length human Hook3, while FKBP was attached to the C-terminus of tdTomato, which had the N-terminal signal peptide of PEX3 (amino acids 1-42). Inside cells, Hook3-FRB would be able to undertake its normal activities, while Pex3-tdTomato-FKBP would be constitutively recruited to peroxisomes. Upon the addition of rapamycin, FRB and FKBP form a complex which recruits Hook3 to peroxisomes. We can then probe the motility of these peroxisomes to understand more about the motors recruited to them (see Figure 4.5 a.).

Differing from the existing approach, we constructed the two components of the assay system in a single reading frame, separated by a P2A self-cleaving peptide sequence (see Figure 4.5 b.). In this way expression of Hook3-FRB was in a 1:1 ratio with PEX3-tdTomato-FKBP, and given the dimeric state of Hook3, this meant there would be two-fold more Pex3-tdTomato-FKBP than Hook3 but the FRB:FKBP ratio would remain 1:1. This plasmid design also meant that 100% of the cells which contained the td-Tomato labelled peroxisomes would also contain Hook3-FRB, which was not fluorescently tagged. It was not known whether an N-terminal or C-terminal FRB domain attached to Hook3 would allow it to function better, and so two constructs were made with the FRB placed at either location.

Inside RPE1 cells, we found that the Pex3-tdTomato-FKBP construct brightly labelled peroxisomes as expected. In the absence of rapamycin, there was very little movement of peroxisomes confirming that the Hook3 and Pex3 components of the assay had been separated by co-translational cleavage of the P2A site. Upon addition of rapamycin, peroxisomes became active almost immediately, and in the case of Hook3-FRB, they showed rapid long-range transport with a bias towards the centrosome (see Figure 4.6 a.). Instances of bidirectional transport could be observed, even in areas of high microtubule polarity, although the polarity of individual microtubules could not be determined at the same time (see Figure 4.6 b.). Peroxisomes were
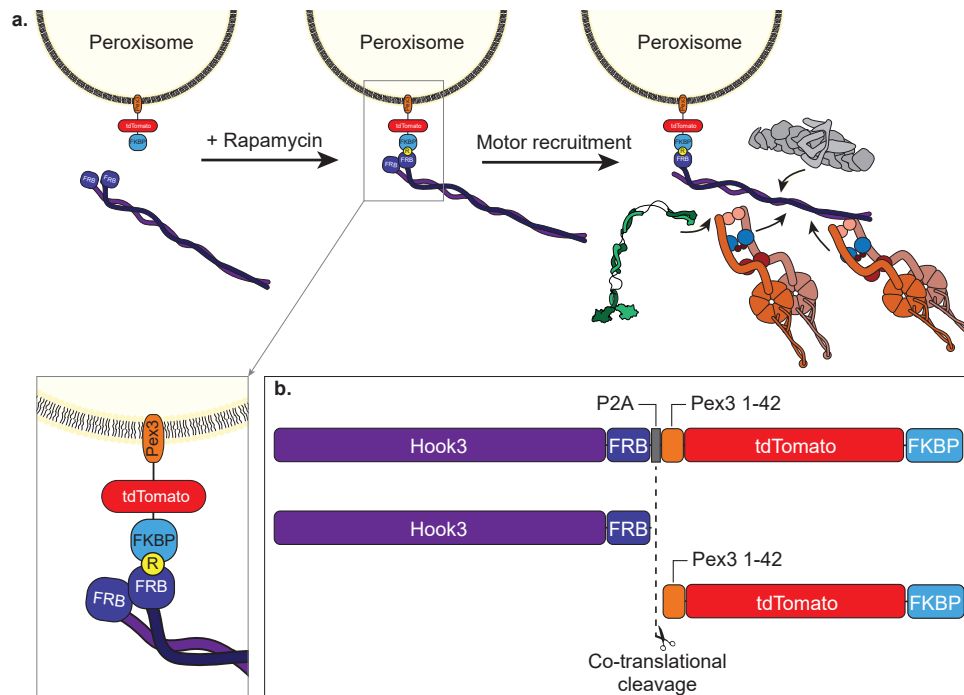
Figure 4.5: Schematic of Hook3 peroxisome recruitment assay | a. Schematic showing how a two-component assay system within cells can be used to recruit Hook3-FRB to peroxisomes. Pex3-tdTomato-FKBP is constitutively recruited to peroxisomes, fluorescently labelling them. Upon the addition of rapamycin, Hook3-FRB interacts with the FKBP on the peroxisomes, and brings with it (or recruits) motor components. The fluorescent peroxisomes become motile. **b.** Schematic of the construct design used to create the two-component assay within a single reading frame using the P2A self-cleaving peptide sequence.

tracked using TrackMate, and then analysed using a purpose built python package. The activation of peroxisome transport was quantified by calculating the mean-squared displacement over the timescales of tracking, and we found that the C-terminally tagged Hook3-FRB showed a huge increase in mean-squared displacement following activation with rapamycin, whereas N-terminally tagged FRB-Hook3 remained mostly diffusional but did show a small increase in mean-squared displacement coupled with a low frequency of motile events (see Figure 4.6 c.).

Peroxisomes showed both immotile diffusional activity, as well as long-range motor driven activities, and so these two types of motility needed to be separated. The effective diffusivity of peroxisomes before rapamycin addition was estimated using the mean-square displacement data by fitting a line to the short timescale behaviour of peroxisomes between 0 and 16 seconds, and was found to be around 0.02 $\mu m^2.s^{-1}$. Using this effective diffusivity, we implemented a method developed by Raphaël Jeanneret, Marco Polin and colleagues to separate diffusional and directed transport events (Jeanneret et al., 2016). This method considered consecutive particle trajectories to decide if they were above or below the threshold for Brownian motion based on the effective diffusivity we had measured. Applying this method to peroxisome tracks allowed automated and reasonably accurate separation of diffusion from directed transport, as shown for tracks from a Hook3-FRB expressing cell pre- and post- activation (see Figure 4.7 a-b.).

From the examples shown, it was clear that peroxisomes had a centrosome-directed bias, and so we wanted to capture polarity of transport within the analysis pipeline to investigate this. The absolute polarity of microtubules cannot be accurately determined, though RPE1 cells are known to have a radial array of microtubules emanating from the centrosome and pericentrosomally located Golgi apparatus, and so the direction of transport either away-from or towards the centrosome could be used as an approximation of whether motion was towards the plus- or minus- ends of microtubules. In order to do this, the python analysis package was extended to allow users to define the centre of the cell when the TrackMate data is first read (see Figure 4.7 c.). Then movements towards- and away-from centre were assigned based on whether the movement decreased or increased the distance of the peroxisome to the centre point. An example of the resultant peroxisome traces shows the overall centrosome-directed bias of peroxisomes and confirms that track directionality can be segregated in this way (see Figure 4.7 d.).

75

a. Hook3-FRB/Pex3-tdTomato-FKBP   Before rapamycin   With rapamycin

GFP-Tubulin Pex3-tdTomato-FKBP

0s   20s 0s   200s

b. With rapamycin

c.

Hook3-FRB before rapamycin
Hook3-FRB with rapamycin
FRB-Hook3 before rapamycin
FRB-Hook3 with rapamycin

Mean-squared displacement (μm^2)

Timescale of MSD calculation (s)
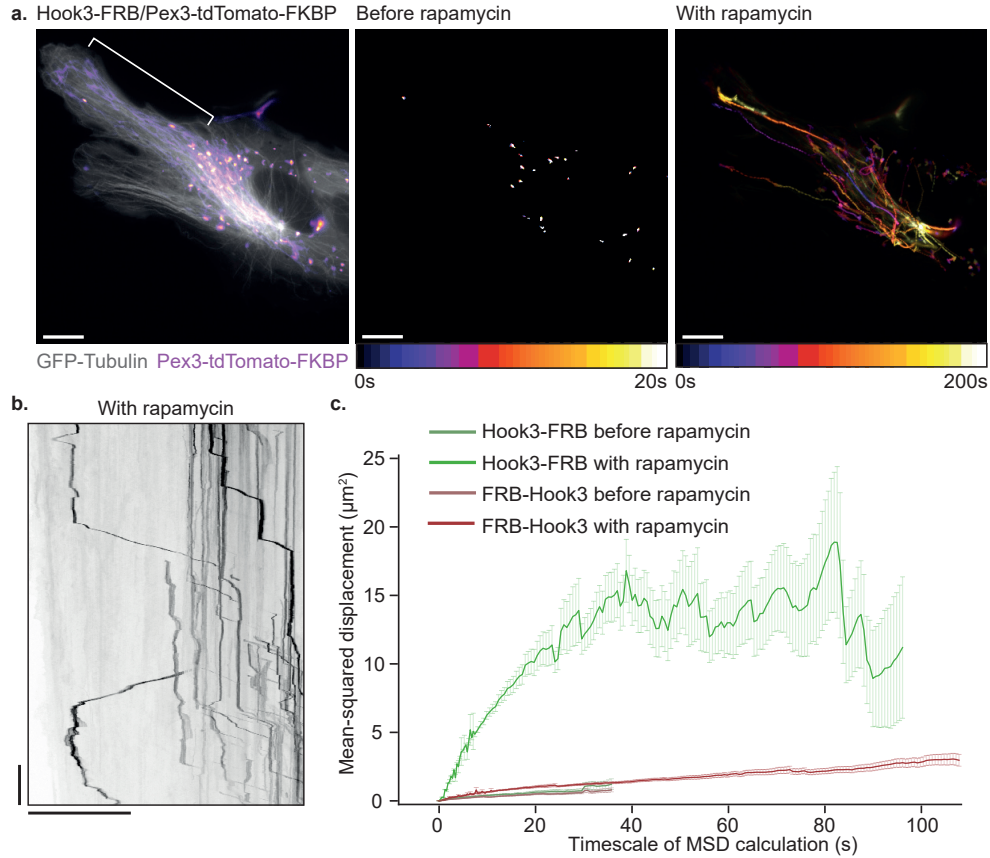
Figure 4.6: Activation of peroxisome transport by Hook3 inside cells |
a. An example cell labelled with GFP-tubulin and transfected with the Hook3-
FRB peroxisome assay plasmid is shown, where the Pex3-tdTomato-FKBP
component forms brightly labelled peroxisome dots. Temporally colour-coded
images show that before rapamycin, there peroxisomes mainly move with
Brownian motion, whereas upon addition of rapamycin, peroxisomes become
motile and undertake rapid and long ranged transport. **b.** A kymograph of the
indicated cellular protrusion from a., showing that in this region of highly or-
dered microtubules, peroxisomes undertake some limited bidirectional trans-
port. The scale bar shows 20 μm in the horizontal axis, and 20 s in the vertical
axis. **c.** Comparison of the mean-squared displacement of peroxisomes be-
fore and after activation, shown for the C-terminally tagged Hook3-FRB con-
struct in green, and the N-terminally tagged FRB-Hook3 construct in red. Line
shows mean of the mean-squared displacement binned over 0.4 s timescales
with standard error.

76
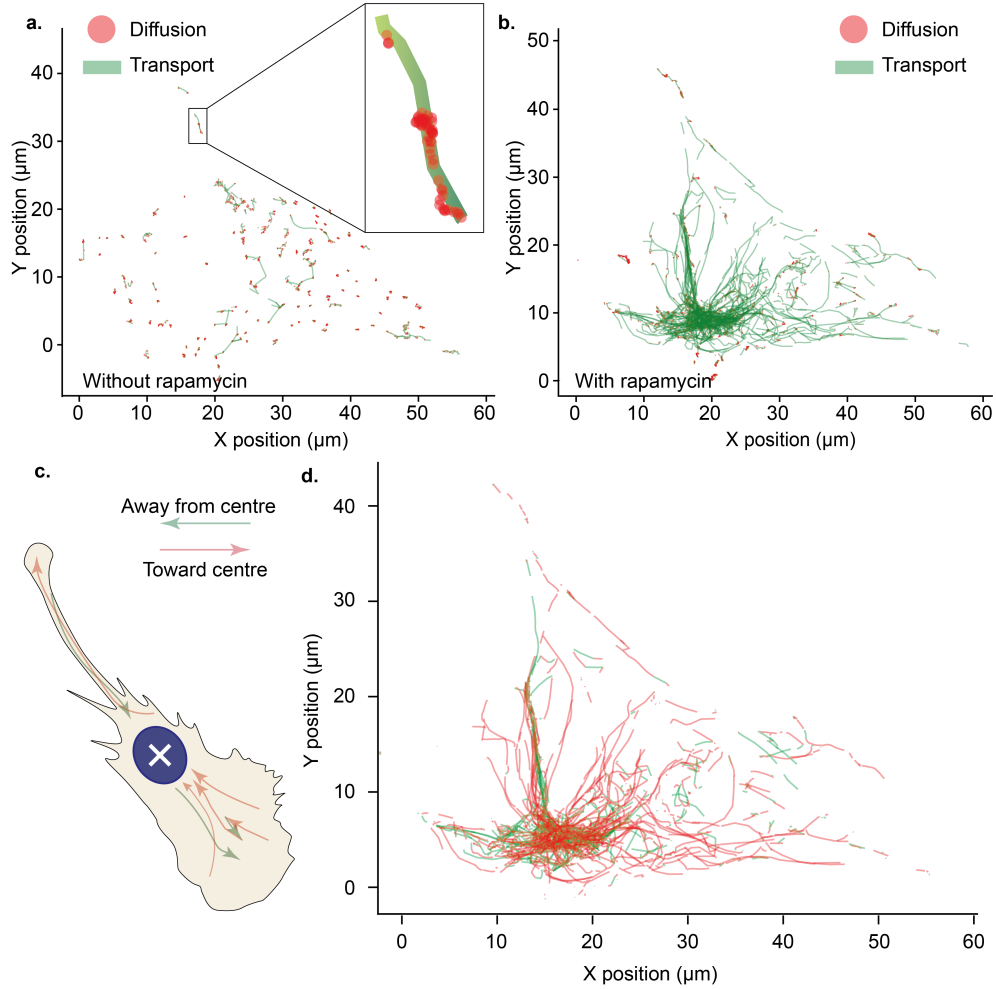
Figure 4.7: Segregating diffusional and directed events from peroxisome tracking | a. Tracks from an RPE1 cell expressing the Hook3-FRB peroxisome assay system, where diffusional and directed motion are separated and shown as red dots or green lines respectively. A zoomed track is shown. **b.** Tracks from the same cell after activation with rapamycin, showing the long-range directed transport with very little diffusional activity. **c.** A schematic cell showing how a reference centrepoint is used to determine whether tracks travel towards or away from the centre point. **d.** Tracks from the same cell where tracks which move towards the centre point are shown in red, while tracks which move away from the centre point are shown in green.
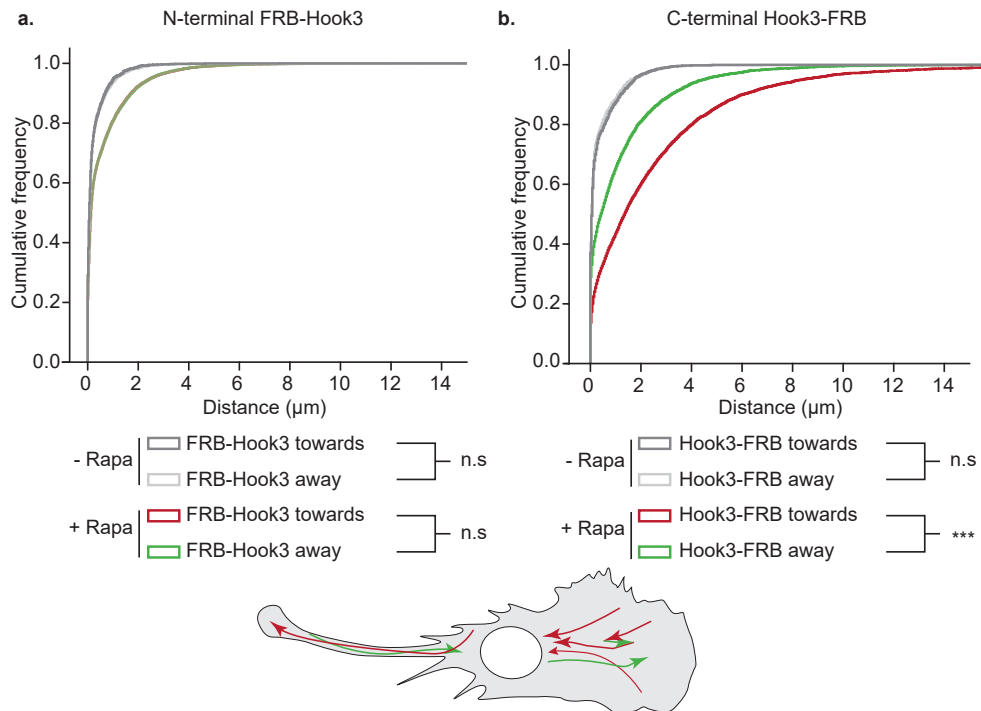
Figure 4.8: Transport direction bias of FRB-Hook3 and Hook3-FRB | a-b.
Directional track distances for FRB-Hook3 or Hook3-FRB driven peroxisome
transport before and after rapamycin addition, where before rapamycin data
are shown in grey and after rapamcyin data are shown in red/green based on
whether they move away from or towards the centre. n.s. indicates $p > 0.05$,
*** indicates $p \leq 0.001$.

The distance travelled towards- or away-from the centre was calcu-
lated for both FRB-Hook3 and Hook3-FRB driven peroxisome transport, be-
fore and after rapamycin addition. As expected, before rapamcyin addition
both constructs showed very small path lengths which had no directional
bias. After rapamycin addition, FRB-Hook3 showed equal transport both to-
wards and away-from the centrosome, while Hook3-FRB showed a large and
statistically significant centrosome-directed bias (see Figure 4.8 a-b.). From
these data it is also apparent how much less distance peroxisomes in the
FRB-Hook3 transfected cells move, confirming what was previously shown by
the mean-squared displacement calculations and suggesting that N-terminally
tagged Hook3 is not able to efficiently activate motors, and in particular minus
end-directed dynein.

Hook3-FRB appeared to favour activation of dynein given the bias in
transport towards the centrosome, and so we wondered if this balance could

be shifted by the depletion of KIF1C or dynein heavy chain. Cells were treated with small interfering RNA (siRNA) against KIF1C, dynein heavy chain or with a control oligonucleotide, and then later were transfected with the Hook3-FRB peroxisome assay plasmid. Transport was activated and quantified. siCtrl cells still showed predominantly towards-centre movements, and depleting dynein heavy chain lead to an increase in away-from centre movements presumably undertaken by KIF1C, though did not significantly change the towards-centre movements of peroxisomes (see Figure 4.9). Interestingly, depleting KIF1C resulted in a decrease in both directions of transport, suggesting that KIF1C and dynein are co-dependent. Overall the effects of depleting motors was small and so we wondered instead whether increasing the amount of KIF1C would re-balance peroxisome transport.

The peroxisome assay plasmid was co-transfected into RPE1 cells alongside KIF1C-GFP, and cells were imaged with two-colour sequential imaging. KIF1C accumulated in the tail of the cell as described previously (Siddiqui et al., 2019; Theisen et al., 2012), while peroxisomes appeared brightly labelled, and no significant colocalisation was seen between the two (see Figure 4.10 a.). In the abundance of KIF1C, rapamycin-activated Hook3-FRB tethered peroxisomes moved all around the cell with less bias towards the centrosome. Temporally colour-coded images show how all regions of the cell have active transport over the length of the recording (see Figure 4.10 b.). KIF1C-GFP was not visible as puncta on peroxisomes during transport, though this was not expected to be the case as the amount of KIF1C on cargoes is thought to be relatively small compared to the cytoplasmic pool and even natural cargoes of KIF1C do not show co-localisation in cells. From stills of the time-lapse over the length of the experiment, it was clear that while some amount of peroxisomes were accumulating at the centrosome, many remained in the cell body and tail (see Figure 4.10 c.). As cells were imaged in two-colours, the time resolution of these data were low and so TrackMate analysis could not be performed robustly without creating erroneous links between peroxisomes that could move up to 2-4 µm between images that were taken every 1.45 s. Therefore, the transport within the tail of the cell is shown as a kymograph (see Figure 4.10 d.), showing how peroxisomes performed both inward and outward directed transport in a reasonably balanced way.

In summary, we found that Hook3-FRB driven transport within the cell is bi-directional and in RPE1 cells this has a bias towards dynein-driven transport. Changing the levels of KIF1C within the cell had a distinct effect on the

directionality of transport, confirming that Hook3 isn't only functioning to link dynein to cargoes but also KIF1C. As we know that much of the KIF1C exists within the cell in its autoinhibited form, transfecting in additional KIF1C-GFP simulated having a larger pool of activatable KIF1C motors. Thus our data suggest that KIF1C expression levels are limiting in RPE1 cells and that modulation of activation can regulate the balance of transport within cells.
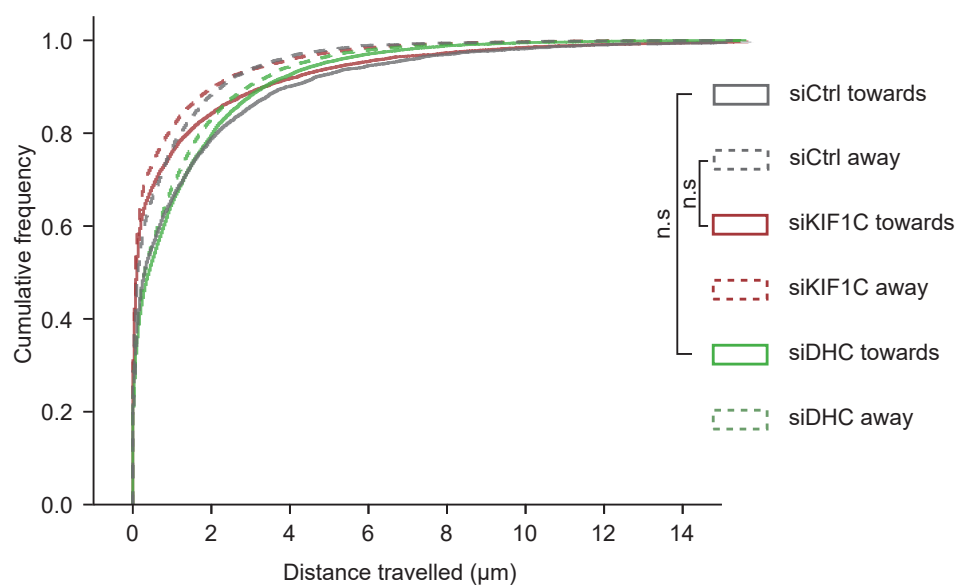
Figure 4.9: Depletion of KIF1C and dynein in peroxisome sorting assay |
Directional track distances of Hook3-FRB/Peroxisome transfected cells which
have been depleted of dynein heavy chain or KIF1C. n.s. indicates p > 0.05,
all other pairwise interactions have p values of <= 0.001.
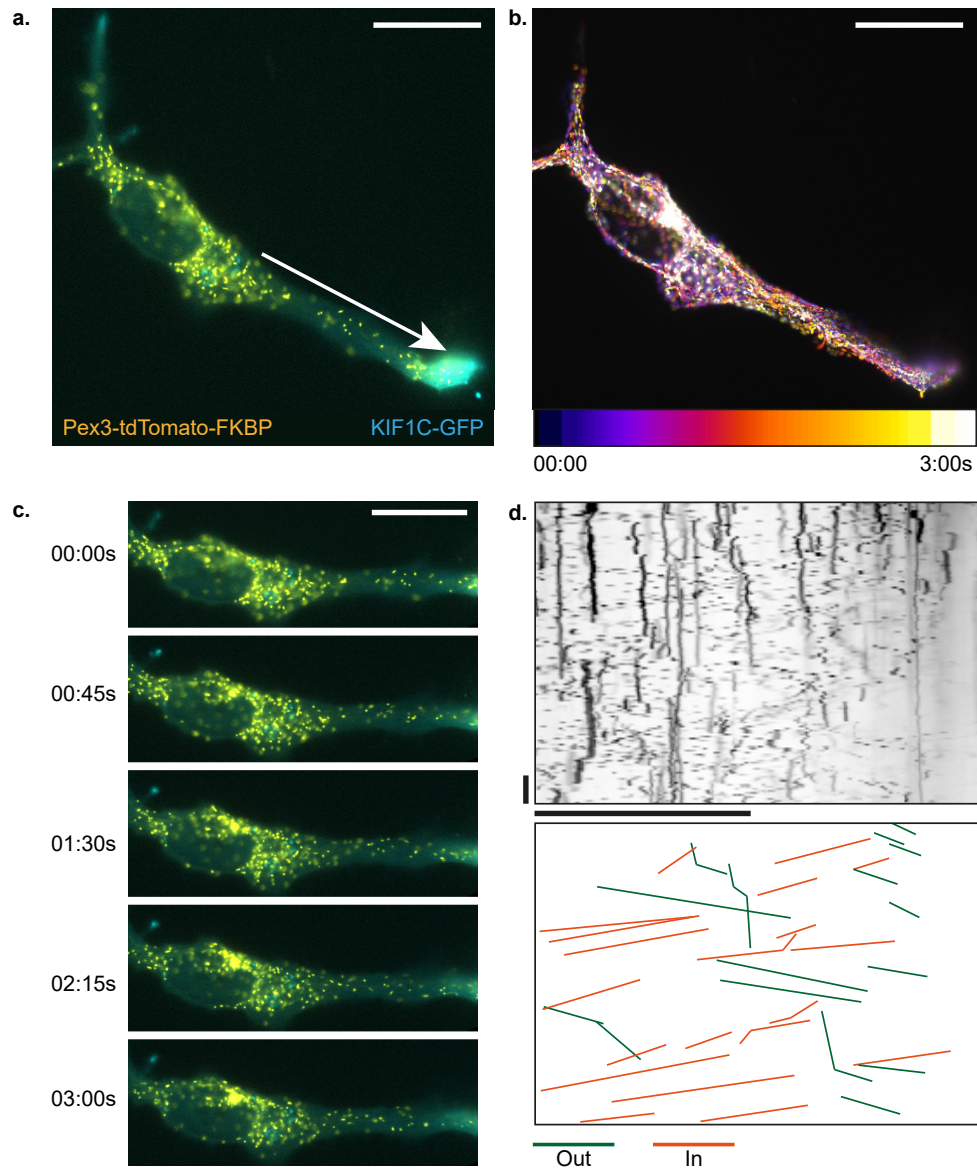
**Figure 4.10: Adjusting peroxisome transport with KIF1C overexpression
| a.** Example of an RPE1 cell co-transfected with Hook3-FRB/Peroxisome
assay (yellow) and KIF1C-GFP (cyan). **b.** Temporally colour-coded image
of the movement of peroxisomes after rapamycin addition. **c.** Montage over
time of peroxisome location within cells, showing that the tail region had ac-
tive peroxisome transport and that this was not depleted over the course of
the experiment. **d.** Kymograph with annotated tracks showing peroxisome
transport within the tail region of the cell (indicated in a.). All scale bars are
20 μm. The kymograph vertical scale bar is 20 s.

Chapter 5

A co-complex of dynein and KIF1C undertakes bidirectional transport in the presence of Hook3

5.1 Linking dynein and KIF1C by dynein adaptors

We found in the first chapter that KIF1C very rarely formed co-complexes with BICD2-SNAPf or BICDR1-SNAPf, whereas complex formation with Hook3-SNAPf was more efficient. Inside cells, acutely inhibited KIF1C appeared to re-localise in a way that suggested its linkage to dynein, and Hook3-FRB driven peroxisomes were bidirectional and dependent on both KIF1C and dynein. We next wondered if any of these adaptors might be capable of linking dynein to KIF1C in the presence of dynactin to create a bidirectional motor protein complex, and predicted from our experiments that Hook3 would be the most likely candidate. Full-length human recombinant dynein complex and porcine dynactin were purified at the MRC Laboratory of Molecular Biology through a collaboration with Andrew Carter's research group using established protocols, and these reagents were provided for the following experiments (Schlager et al., 2014; Urnavicius et al., 2015).

Dynein, dynactin, dynein-adaptor and KIF1C-GFP were mixed at a molecular ratio of 1:1:8:1 and their motility was observed on microtubules using a final concentration of 5 nM dynein, dynactin and KIF1C with 40 nM of dynein adaptor. We found that all of the full-length wild-type dynein adaptors

created in this study were able to activate dynein motility, and Hook3 readily made complexes of dynein and KIF1C together whereas BICDR1 and BICD2 only did so rarely (see Figure 5.1 a-c.). The landing rate of two colour co-complexes of KIF1C and dynein was nearly ten-fold more for Hook3 than for BICD2 or BICDR1, and around 50 % of dynein tracks also had KIF1C-GFP signal (see Figure 5.1 d-e.).

The amount of complexes that land on the microtubule may be limited by the accessibility of dynein and KIF1C's motor domains. For example, if BICD2 and BICDR1 preferentially create inhibited complexes of dynein and KIF1C, this would decrease the observation of these complexes on micro-tubules. For this reason, we attempted to measure the complex formation of these molecules directly adsorbed to glass surfaces, taking out microtubule landing ability as a factor.

Incubated protein mixtures were diluted in imaging buffer, flowed into plasma-cleaned but uncoated glass chambers, and allowed to adhere for a few seconds before unattached complexes were flushed away with the addi-tion of buffer. Done correctly this created glass surfaces uniformly covered in fluorescent proteins which could be imaged by total internal reflection flu-orescence (TIRF) microscopy (see Figure 5.2 a.). Fluorescent spots were detected by finding points of maximal brightness above the background, and the threshold for detection was altered manually per field-of-view to ensure the background was not detected as spots. These data were then analysed to find which spots appeared only in one channel, or which spots appeared in multiple channels, and in this way we could differentiate the individual flu-orescent components on their own, or the fluorescent components that had formed complexes.

We found that the majority of spots that we detected did not appear to be in complexes (see Figure 5.2 b.) and were instead motors or adaptors on their own. Protein complex mixtures containing Hook3 had the highest rate of forming spots which contained more than one wavelength signal, at 2.8% of spots, whereas BICDR1 and BICD2 very rarely formed co-localising spots, representing only 0.4% of particles.

Co-localising spots were sub-classified (see Figure 5.2 c.). Hook3 most often formed spots containing KIF1C, while BICD2 and BICDR1 did this two-fold less often, and this echoed our previous findings of KIF1C and dynein adaptor motility on microtubules. While BICDR1 and BICD2 formed multi-colour complexes seven-fold less often than Hook3, when those complexes
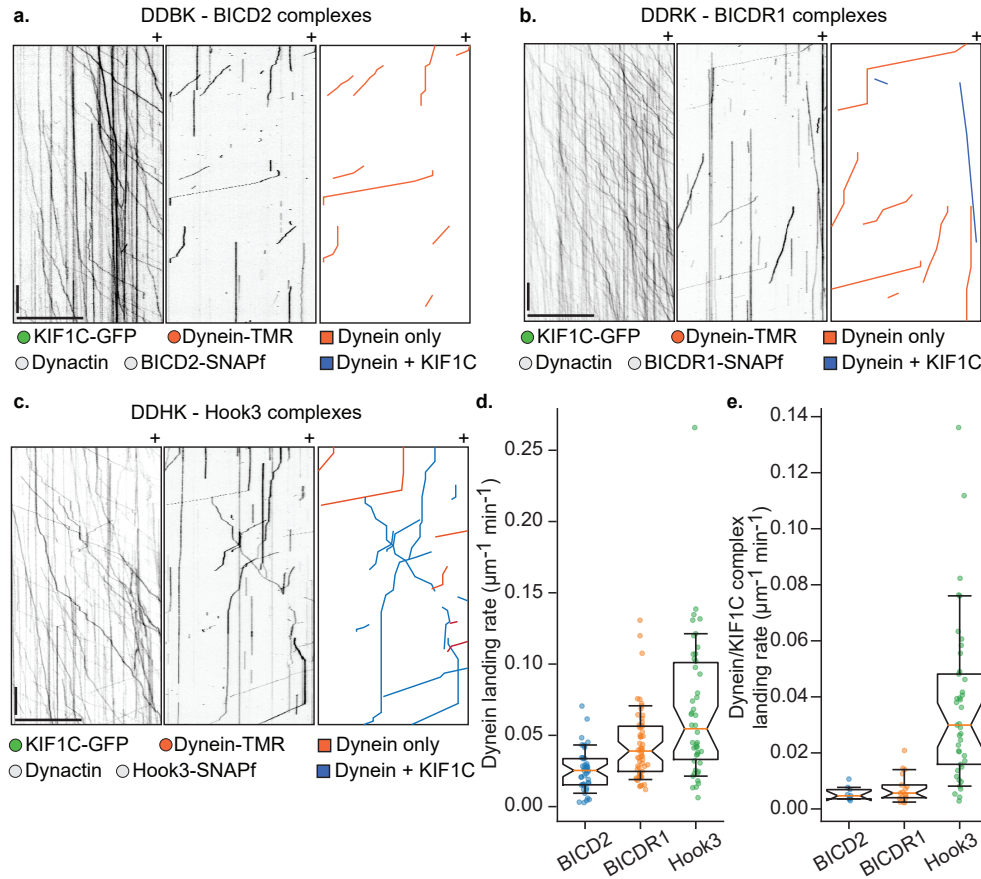
Figure 5.1: Motility of complexes of dynein, dynactin and KIF1C in the presence of different dynein adaptors | Complexes of dynein, dynactin and KIF1C-GFP formed with **a.** BICD2, **b.** BICDR1 or **c.** Hook3, where dynein molecules that appear without KIF1C-GFP molecules are labelled with orange lines, and those that appear with KIF1C-GFP are labelled with blue lines. **d.** Landing rate of all dynein molecules on the microtubule. **e.** Landing rate of co-complexes of KIF1C and dynein. Scale bar represents 20s and 20μm in the vertical and horizontal axes. Dots represent individual microtubules.
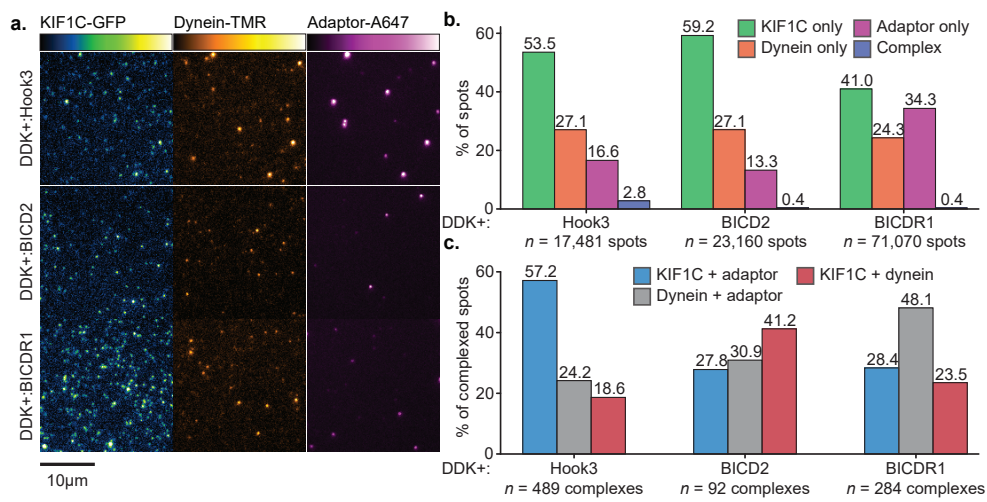
Figure 5.2: Complex formation of dynein and KIF1C with different dynein adaptors in solution | a. Glass surfaces were coated with the indicated protein complexes following incubation. Unstuck molecules were removed and then the single molecules that remained were imaged using TIRF microscopy. Example images for each complex are shown. Images of the same wavelength have their contrast scaled equally. Scale bar is 10 µm. **b.** Spots were detected and their location was used to determine if the spots existed in just one channel or multiple channels. The proportion of individual fluorescent components is shown, as well as those which had formed complexes. **c.** The complexed molecules were further sub-classified to find which signals were present, revealing that KIF1C and dynein both formed complexes with dynein adaptors, as well as with each other.

were sub-classified it was found that around 20-40% of them contained both KIF1C and dynein. However, as a fraction of all spot detections, dynein and KIF1C co-localising spots appear as 0.5 % of all spots for Hook3, 0.016 % for BICD2 and 0.009% for BICDR1, meaning that Hook3 formed co-complexes of dynein and KIF1C around 4-5x more often than BICD2 and BICDR1. This magnitude of change was consistent with the five-fold increase in landing rate of dynein and KIF1C co-complexes on microtubules in the presence of Hook3 compared to BICD2 or BICDR1, confirming that spot-counting and microtubule-landing measurements both sample the same complex formation process.

Taking the complex motility and spot-counting experiments together, we concluded that although complex formation of KIF1C and dynein in the presence of BICD2 and BICDR1 was possible, Hook3 was much more efficient at performing this role and was therefore the molecule of most interest in understanding bidirectional motility.

5.2 Improving Hook3-SNAPf purification and stability

We next sought to improve the purification of Hook3 as we had noticed that a significant portion of it passed over gel filtration within the void volume of the column, and step-wise photobleaching of Hook3-647 showed that some amount of the protein existed in populations larger than the dimeric protein we expected to find (see Figure 5.3 a-b.). In order to be confident in assigning run lengths, speeds and landing rates to KIF1C/dynein-TMR complexes, it was first necessary to ensure that the Hook3-SNAPf had undergone size-exclusion chromatography and was free from aggregates.

In the process of generating a purification protocol for Hook3-SNAPf, we had found that the pH of the purification buffers (either 7, 7.2 or 7.4) and the amount of sodium chloride (either 150mM or 300mM) had not made a clearly noticeable effect on how the Hook3 performed in single molecule experiments. A typical purification process for Hook3-SNAPf is described in Figure 5.4, and several steps of this procedure were of concern: step 5., an elongated incubation with IgG sepharose, step 7., the effect of SNAP-Alexa647 on the protein, and step 9., the stability of the protein overnight during TEV digestion. To understand more about the effects of these steps, a Ni-NTA purification of Hook3-SNAPf was performed and then gel filtration was used to determine the proportion of protein which appeared aggregated (see Figure
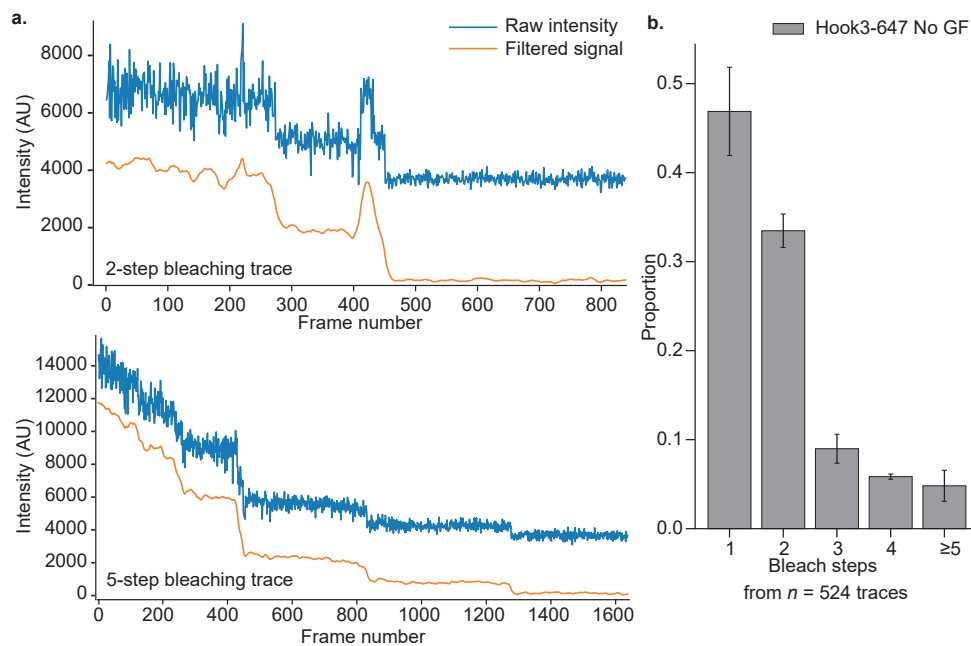
Figure 5.3: Bleach-step analysis of Hook3 prior to gel filtration | a. Bleach traces showing an example of a two-step bleaching event, as well as a much larger arrangement of molecules which bleached in approximately five steps. **b.** Proportion of spots displaying each number of bleach steps.

1. Cell pellets lysed
2. Lysate cleared by ultracentrifugation
3. Cleared lysate incubated with Ni-NTA beads
4. Ni-NTA beads washed and protein eluted from step 1 of purification
5. Ni-NTA eluate incubated with IgG Sepharose
6. IgG beads washed
7. IgG beads resuspended in SNAP-Alexa647 substrate to dye
8. IgG beads washed of dye and resuspended in buffer containing TEV protease
9. TEV digestion performed overnight at 4C with agitation
F. Finishing: Digested protein collected, concentrated and stored

Figure 5.4: Purification and labelling procedure of Hook3-SNAPf before optimization | Schematic timeline of a typical purification process of Hook3-SNAPf from *Spodoptera frugiperda* (Sf9) insect cell pellets, including labelling with SNAP-Alexa647 and digestion with TEV protease.

5.5 a-c.). Separate samples of the Hook3-SNAPf eluate were treated with different steps of the protein purification protocol and then run over the gel filtration column to check if the ratio of aggregated protein increased. Non-aggregated Hook3-SNAPf appeared in a peak around 11ml, consistent with it being a highly elongated coiled coil. All samples of Hook3 showed a proportion of protein in the void volume of the column, which was confirmed by the presence of the 647nm absorption pattern for Sample 2 which had been dyed, and could also be seen on gels (see Figure 5.6 a-c). The peak height of the void volume compared to that of the stable Hook3-SNAPf was highest for the sample which had been kept overnight at 4°C, though all conditions produced an amount of non-aggregated protein which passed over the column.
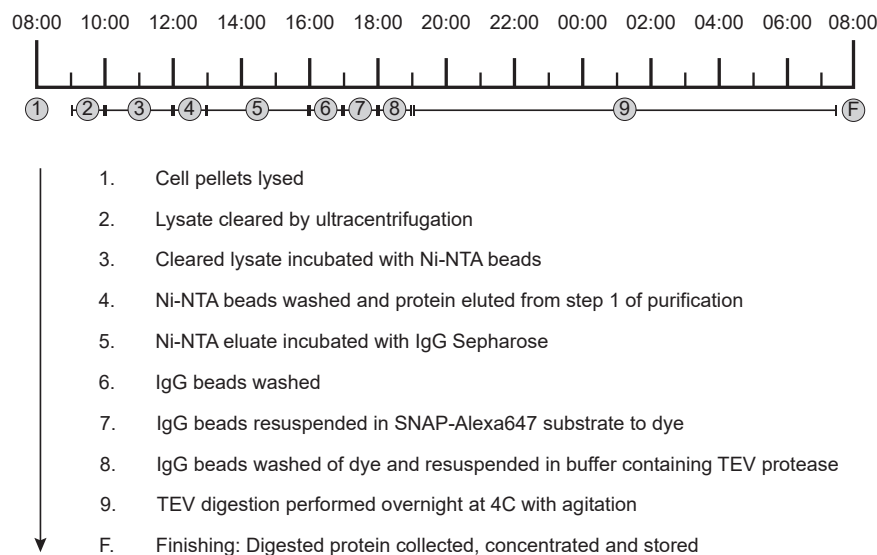
We next sought to determine if this proportion of non-aggregated protein was stable, or whether it tended towards aggregation after further handling steps (such as concentration and freezing). Therefore we took concentrated Hook3-SNAPf labelled with Alexa 647 from outside the void volume of Sample 2, froze it and ran a small portion over an analytical size Superose 6 increase 3.2/300 column to check whether a proportion of the previously stable protein appeared within the void volume of the column. Although the absorbance signal was low, by looking at absorption of the Alexa 647 dye it was determined that this Hook3 remained outside the void volume of the column (see Figure 5.6 d.).

From this optimisation we concluded that a proportion of Hook3-SNAPf remains aggregated, and this may occur during expression or early during the purification process. However, this proportion of aggregated protein is relatively static, as even keeping the protein overnight only slightly increased the proportion of protein that appeared as aggregates. Importantly, downstream processing of the gel filtered protein by concentration and freezing did not revert stable protein to its aggregated form.

Stepwise photobleaching of the gel-filtered Hook3-SNAPf showed that the amount of larger collections of molecules reduced, and the majority of spots bleached in either 1 or 2 steps (see Figure 5.7 a-b.). Complexes of KIF1C and dynein still formed in the presence of this new Hook3 source along with dynactin and undertook robust transport along the microtubule both towards the plus and minus ends (see Figure 5.7 c.). Thus we were reassured that the complexes we observed were formed through a genuine function of Hook3 and not by its aggregation.
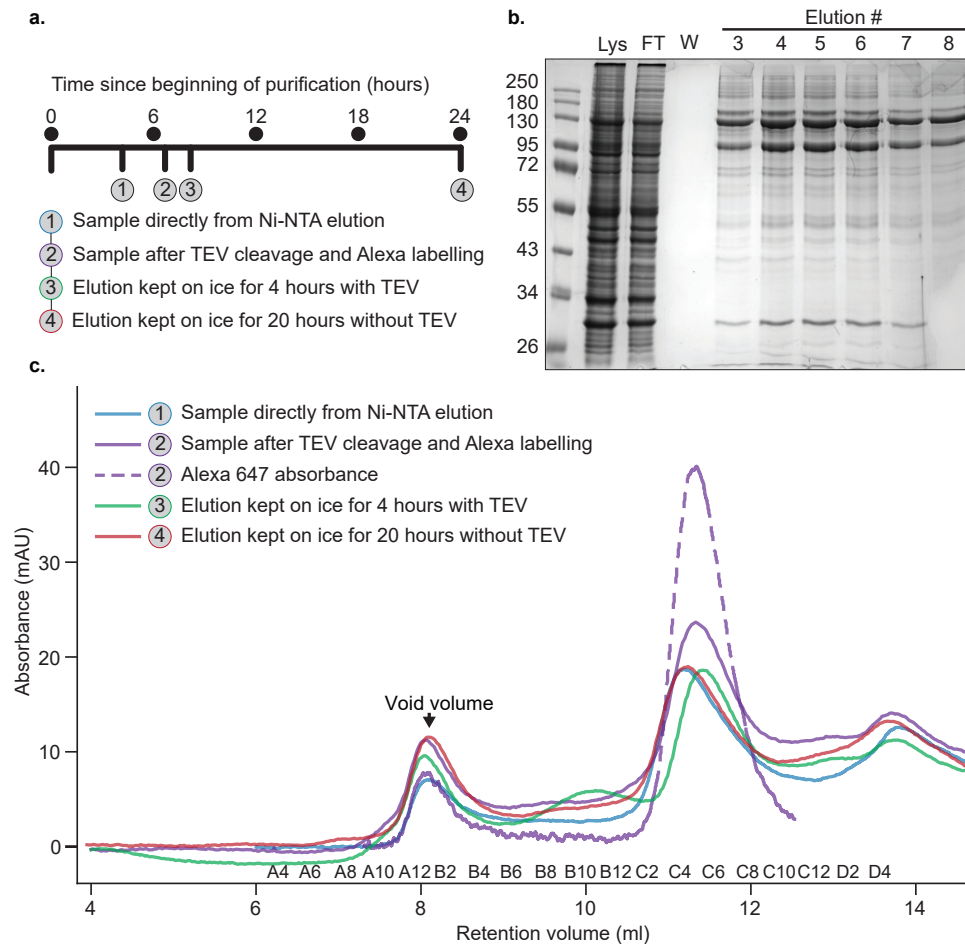
Figure 5.5: Stability testing of Hook3-SNAPf by gel filtration | a. Schematic timeline of the stability testing experiment, showing the samples which would be taken and submitted to gel filtration analyses. **b.** Coomassie-stained gel showing protein Hook3-SNAPf after a single-step Ni-NTA purification where Hook3-SNAPf appears at the 130KDa marker. **c.** Combined gel filtration traces of the indicated Hook3-SNAPf samples submitted to gel filtration over a Superose 6 increase 10/300 column.
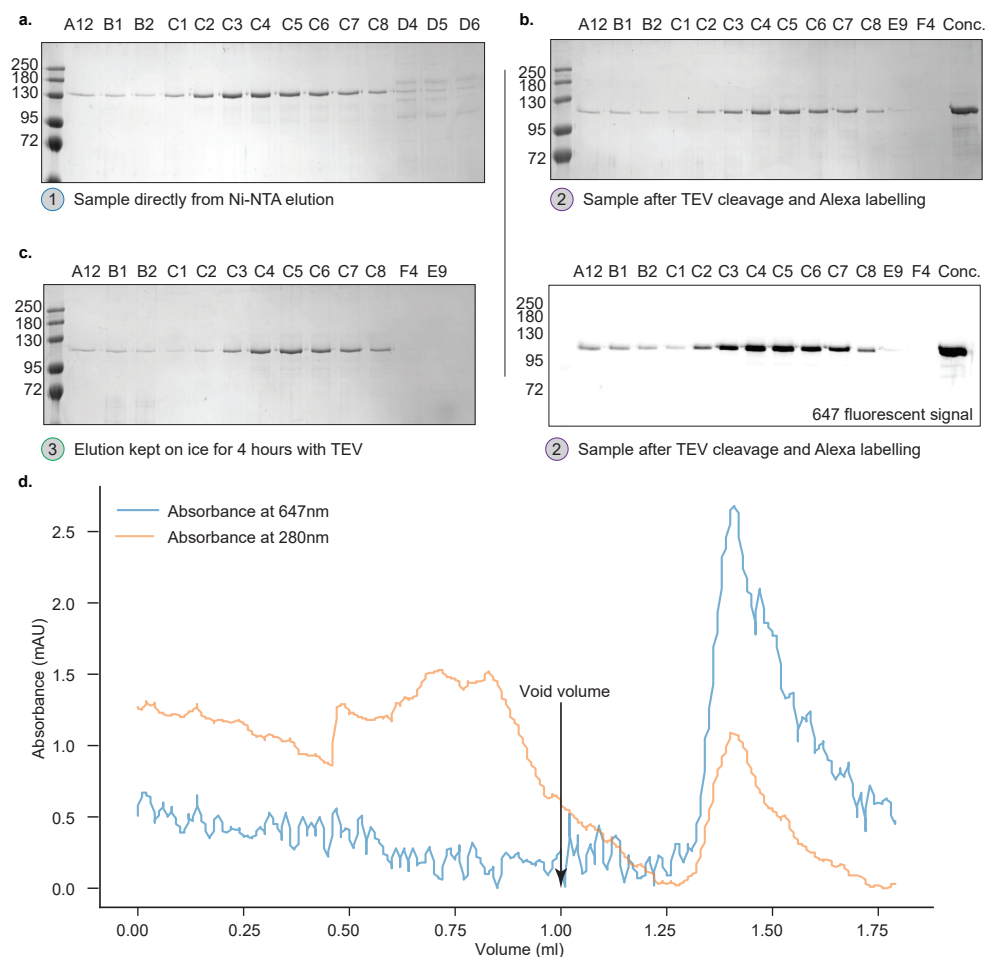
Figure 5.6: Gels showing Hook3-SNAPf after gel filtration stability testing | a-c. Samples of the indicated elution were taken from gel filtration experiments in Figure 5.5 and run on acrylamide gels. Hook3-SNAPf appears at the 130KDa marker before digestion with TEV protease, and between the 95 and 130KDa markers after digestion with TEV protease. As Sample 2 was labelled with Alexa647, the fluorescence of the labelled protein is also shown. **d.** Analytical run of a portion of concentrated Hook3-SNAPf Alexa-647 after freezing, showing that the protein still appears outside of the void volume.
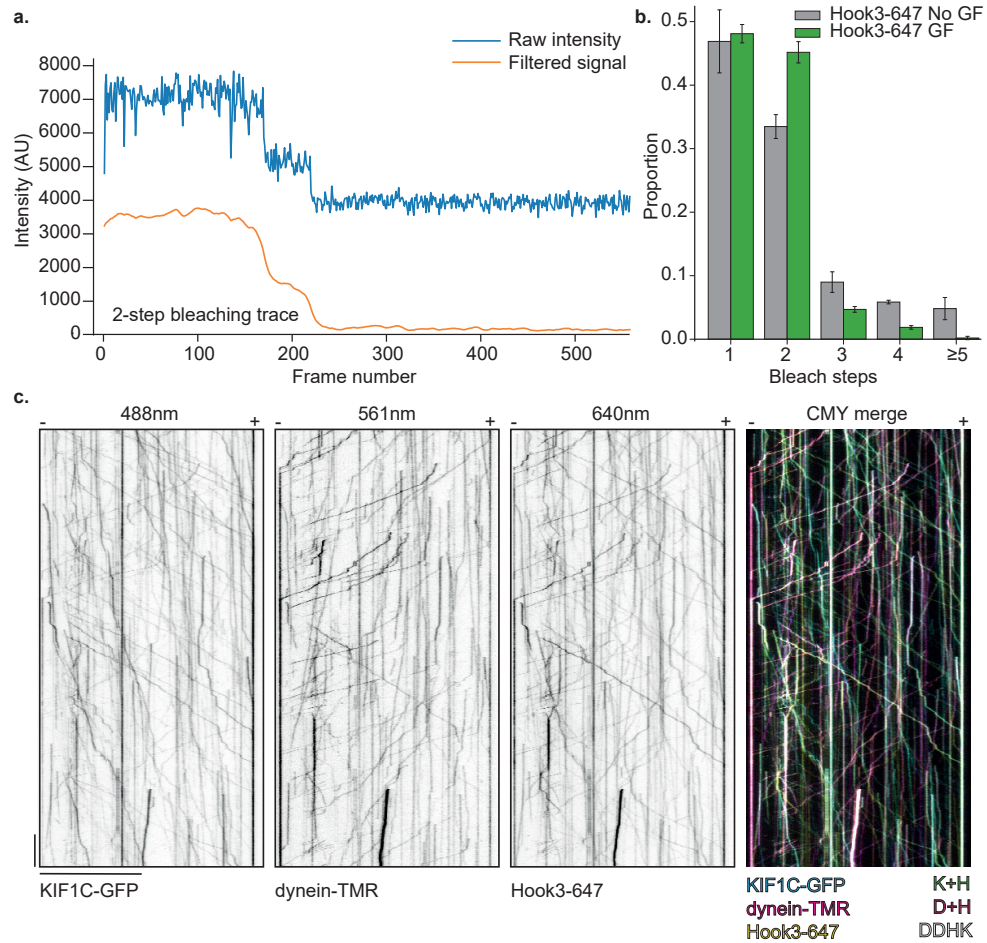
Figure 5.7: Hook3-647 bleach-step and single molecule motility after gel filtration | a. An example of a two-step bleaching event from gel-filtered Hook3-647. **b.** Proportion of bleach steps for spots for gel filtered Hook3-647 compared to non-filtered protein shown in 5.3. **c.** Example of motility of dynein-dynactin-Hook3-KIF1C (DDHK) complexes formed with gel-filtered Hook3-647 showing that KIF1C-GFP and dynein-TMR co-complexes are still possible.

5.3 Generating untagged Hook3 and Lis1 to create fully activated dynein and KIF1C complexes

Having validated that the DDHK complex was not formed due to aggregation of Hook3, we next sought to pick apart the intricate run characteristics of the complex to understand how it differed compared to its individual components. To do this we decided non-tagged Hook3 would be more suitable than Hook3-SNAPf, as others had shown that the whole C-terminal region of Hook3 contributes towards KIF1C binding (Kendrick et al., 2019), and we had evidence from our peroxisome assay described in Chapter 2 that an N-terminal tagged Hook3 was not fully active.

Untagged or minimally tagged versions of Hook3 turned out to be extremely difficult protein purification targets, and so the full range of constructs and methods that were attempted are summarised in Table 5.1. In trying to generate good quality untagged Hook3, we moved to a mammalian expression system in HEK293T suspension cells and expressed both mouse and human Hook3 genes with an N-terminal 8xHis-ZZ purification tag, as well as GFP on some constructs to aid tracking the protein throughout purification by its fluorescence. In all cases, expression levels and recovery of Hook3 was low despite working at relatively large scales (typically 400ml of HEK293T cells; $1x10^9$ cells). Hook3 that was tagged with a C-terminal GFP or SNAPf, or Hook3 that had no C-terminal tag, passed over gel filtration in a manner similar to Hook3-SNAPf purified from Sf9 insect cells, whereas we were not able to recover N-terminally tagged SNAPf-Hook3 from gel filtration.

In an attempt to recover more protein, we created Hook3 tagged with the TwinStrep tag which shares near covalent affinities for StrepTactin-XT beads, however expression of this construct in a HEK293 system suffered from the same limitations of expression efficiency and recovery as the 8xHis-ZZ tagged proteins, with the additional difficulty that proteins remained stuck to beads even in elongated incubations with 50mM d-Biotin.

Finally, we reverted back to a Sf9 insect-cell expression system as protein expression levels were much higher and thus we had more opportunity to capture and purify enough Hook3 for complex formation experiments. Hook3 tagged with an N-terminal 6xHis and C-terminal TwinStrep tag expressed at very high levels, though capture on Ni-NTA was very poor, suggesting that the N-terminal portion of the protein was not fully accessible, however the C-terminal TwinStrep tag was accessible and protein could be captured and pu-

Plasmid name	N-terminal tags	C-terminal tags	Fluorescent tag	Gene	Expression system	Summary
pKan-CMV-His-ZZ-LTLT-mmHook3-GFP	8x His followed by tandem protein A like domain	None	Ct GFP	Mouse	HEK293T Suspension	Single-step IgG sepharose purification followed by gel filtration. Low yield protein expression/purification, passes over gel filtration on a G4000 column in and outside of the void volume. Visible on protein gel but recoverable amount too low.
pKan-CMV-His-ZZ-LTLT-hsHook3-GFP	8x His followed by tandem protein A like domain	None	Ct GFP	Human	HEK293T Suspension	
pKan-CMV-His-ZZ-LTLT-mmHook3-SNAPf	8x His followed by tandem protein A like domain	None	Ct SNAPf	Mouse	HEK293T Suspension	Single-step IgG sepharose purification followed by gel filtration. Yield lower than for equivalent GFP constructs, no visible protein on gels after gel filtration but western blot confirmed similar distribution of Hook3 inside/outside the void volume similar to existing Insect-cell expressed Hook3-SNAPf.
pKan-CMV-His-ZZ-LTLT-hsHook3-SNAPf	8x His followed by tandem protein A like domain	None	Ct SNAPf	Human	HEK293T Suspension	
pKan-CMV-His-ZZ-LTLT-mmHook3	8x His followed by tandem protein A like domain	None	None	Mouse	HEK293T Suspension	No purification attempted.
pKan-CMV-His-ZZ-LTLT-hsHook3	8x His followed by tandem protein A like domain	None	None	Human	HEK293T Suspension	Single-step IgG sepharose purification followed by gel filtration on G4000 column. Small amount passed over the column. Scaling up the preparation from 500ml of original insect culture to 1 litre did not increase yield.
pKan-CMV-His-ZZ-LTLT-SNAPf-mmHook3	8x His followed by tandem protein A like domain	None	Nt SNAPf	Mouse	HEK293T Suspension	No purification attempted.
pKan-CMV-His-ZZ-LTLT-SNAPf-hsHook3	8x His followed by tandem protein A like domain	None	Nt SNAPf	Human	HEK293T Suspension	Single-step IgG sepharose purification followed by gel filtration on Superose 6 column. Large void volume peak, and no protein visible outside of the void on gels.
pKan-CMV-hsHook3-TwinStrep	None	TwinStrep tandem StrepII	None	Human	HEK293T Suspension	Single-step StrepTactin-XT bead purification. Recovery very low, with small amounts remaining stuck to beads in the presence of 50mM d-biotin.
pFastBacM13-6H-Hook3-TwinStrep	6x His	TwinStrep Tandem StrepII	None	Human	Sf9 Insect	Expression level very good. No/little binding to Ni-NTA beads. Good binding and purification on StrepTactin-XT beads, however only a small amount of protein bound. Protein eluted from single-step StrepTactin purification passed over gel filtration on a Superose 6 column similarly to Hook3-SNAPf. Attempts to replace initial Ni-NTA step with a Q column showed extremely high binding capacity and strength remaining on the beads until 500mM NaCl, however protein recovered from Q beads did not elute from Superose 6 gel filtration column in the correct place and was not competent in activating dynein/KIF1C complex formation.
pFastBacM13-HZL-Hook3	8x His followed by tandem protein A like domain	None	None	Human	Sf9 Insect	Expression level very good. No/little binding to Ni-NTA beads however good binding to IgG sepharose. Passed over gel filtration on Superose 6 colum but recovery was low.

Table 5.1: Summary of Hook3 constructs and purification optimisations

rified through this tag. The TwinStrep purification performed similarly as from mammalian cell preparations in that although it generated very pure protein, the recovery levels were low and the protein did not easily come off resins. In troubleshooting the purification of this protein, we also found that Hook3 bound very strongly to Q ion-exchange chromatography resins and that this could be used to capture the protein out of cell lysates. Hook3 remained bound to Q resins up to 500mM NaCl, but Hook3 eluted in this way passed over gel filtration differently to affinity-purified Hook3, and it was not able to activate dynein-dynactin complex formation *in vitro*.

Given the lack of success of TwinStrep purifications, we returned to an 8xHis-ZZ purification tag. After several attempts we generated Hook3 that would pass over a Superose 6 column, although in small amounts (see Figure 5.8 a-c.). Despite the poor yield, we took the gel filtered protein, concentrated it, and found that even though its concentration was low, it was still able to activate the formation of dynein-dynactin complexes although the complex formation was not as efficient as when Hook3 was added in excess (data shown in following section). Thus we had a source of gel-filtered and untagged Hook3 which could be used in single-molecule experiments.

Complex formation of dynein, dynactin and adaptor proteins in vitro is typically performed with large molar excess of dynein adaptor to aid efficiency (Urnavicius et al., 2017), though this was not possible with the limited amounts of full-length untagged Hook3 we could recover. Lis1 is known to aid the complex formation of dynein and dynactin with adaptor proteins at multiple stages (Baumbach et al., 2017; Htet et al., 2020). To improve complex formation with limited concentrations of untagged Hook3, we produced the dynein activating factor Lis1. We expressed Lis1 in Sf9 insect cells using an existing His8-ZZ tagged protein construct which was kindly provided by Andrew Carter (see Figure 5.9 a.), and then purified it using slight modifications to an established protein purification procedure (Baumbach et al., 2017). Lis1 was purified by IgG sepharose affinity, eluted by cleavage with TEV protease, and then gel filtered on a HiLoad 16/60 Superdex 200pg column (see Figure 5.9 b-d.). The final concentrated reagent was 13.87 mg/ml allowing complex formation and single-molecule assays to be performed in a background of high Lis1 concentration.

The activation effect of Lis1 upon addition to dynein-dynactin-Hook3 (DDH) complexes was tested in the presence or absence of full-length KIF1C-GFP. Complexes were formed by mixing 50 nM of each dynein, dynactin and

a.

1. Lyse

2. Clear by ultracentrifugation

3. Batch-bind to IgG sepharose for 2.5 hours.

4. Wash 300-400 ml

5. Resuspend beads in buffer with TEV protease

6. Incubate 60 minutes with TEV protease at 25°C.

7. Collect protein, hard-spin away any debris, and concentrate.

8. Inject into Superose 6 10/300 colum.

b.

Fractions

Elu. B Conc. 4 5 6 7 8 9 10 11 12 13 14

250 180 130 95 72 55 43 34 26

Void peak   Selected peak

c.

Figure 5.8: Purification of untagged Hook3 | a. Summary of the process used to purify 8xHis-ZZ-Hook3 from insect cells. **b.** A protein gel showing samples from the purification of untagged Hook3 from the point of elution from IgG sepharose beads by TEV cleavage. *B*-sample shows "beads" loaded onto the gel, to see the amount of Hook3 that remains bound to beads, while *Conc.* shows the protein after it had been clear spun and concentrated in a centrifugal ultrafiltration concentrator. **c.** Gel filtration trace of untagged Hook3 on a Superose 6 increase 10/30 column.
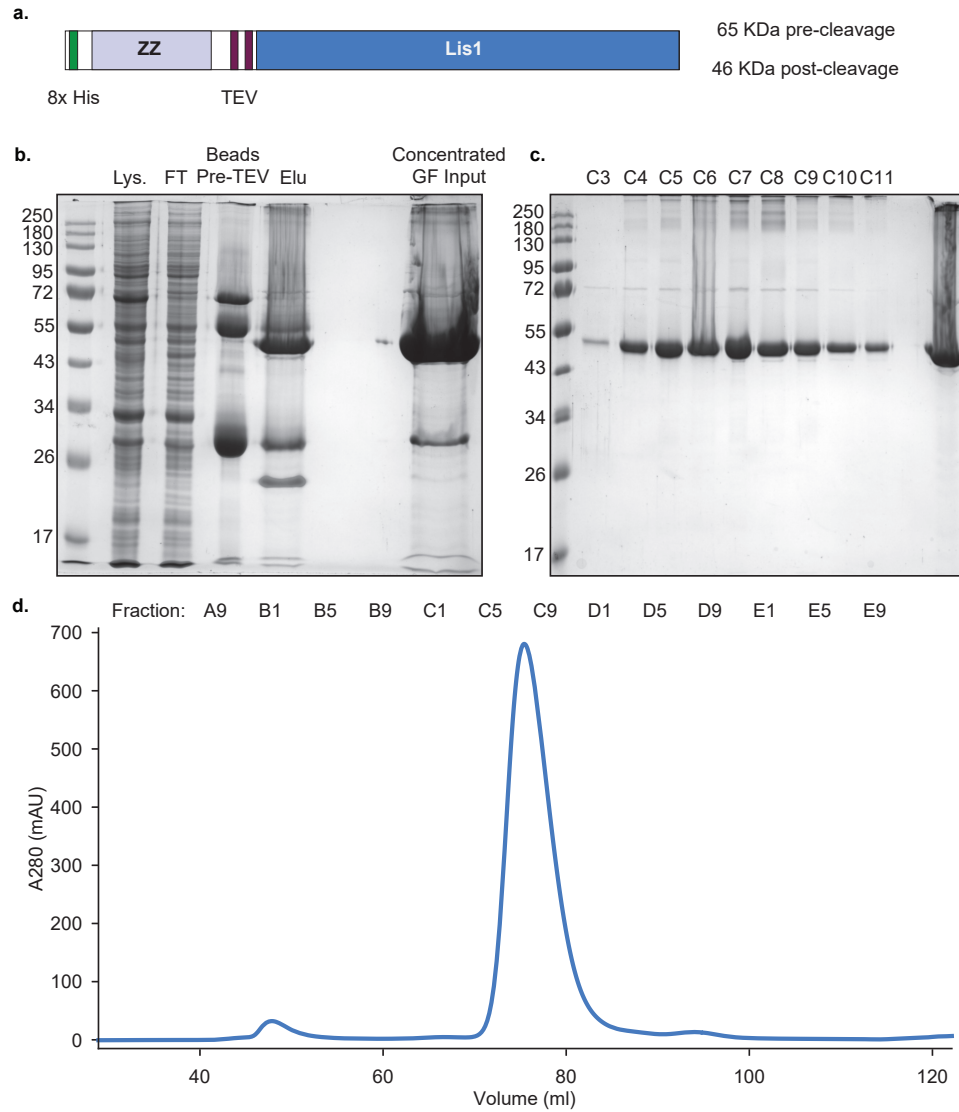
Figure 5.9: Purification of Lis1 | a. Schematic of the TEV-cleavable Lis1 construct used in this study. **b.** Protein gel showing the IgG sepharose purification of Lis1, where *Lys.* is cleared lysate after ultracentrifugation, *FT* is the flow-through, i.e. the lysate after interaction with affinity resin, and *Elu.* is the eluted protein after TEV protease cleavage. **c.** Protein gel showing fractions from the gel filtration of Lis1 using a Superdex 200pg 16/60 column. **d.** The absorbance trace of Lis1 passing over gel filtration, showing that Lis1 primarily forms a single peak centered on 75ml.

KIF1C-GFP or KIF1C buffer control in the presence of 250nM untagged Hook3 and 1250nM untagged Lis1. Complexes were incubated on ice for 45 minutes before being diluted 1:40 into single molecule assays to achieve a final concentration of 1.25nM dynein, dynactin and KIF1C with 6.25nM of Hook3 and 31.25nM of Lis1. Under these conditions, formation of DDH complexes in the absence of Lis1 was very rare (only 0.015 $\mu m^{-1}.s^{-1}$), but could be substantially increased nearly eight-fold by its addition (see Figure 5.10 a-b.). The creation of two-colour DDHK complexes was also improved by Lis1 addition (see Figure 5.10 c-d.). Quantification of landing rates showed that Lis1 increased the observation frequency of DDH by 750% while also increasing the observation frequency of two-colour DDHK complexes by 260% (see Figure 5.10 e.). The minus-end directed speeds of dynein also increased in the presence of Lis1 (see Figure 5.10 f.). Thus we verified that our Lis1 was able to replicate complex formation phenotypes described in the literature (Baumbach et al., 2017; Htet et al., 2020), and that using Lis1 would allow us to create DDH complexes with relatively low concentrations of untagged Hook3.
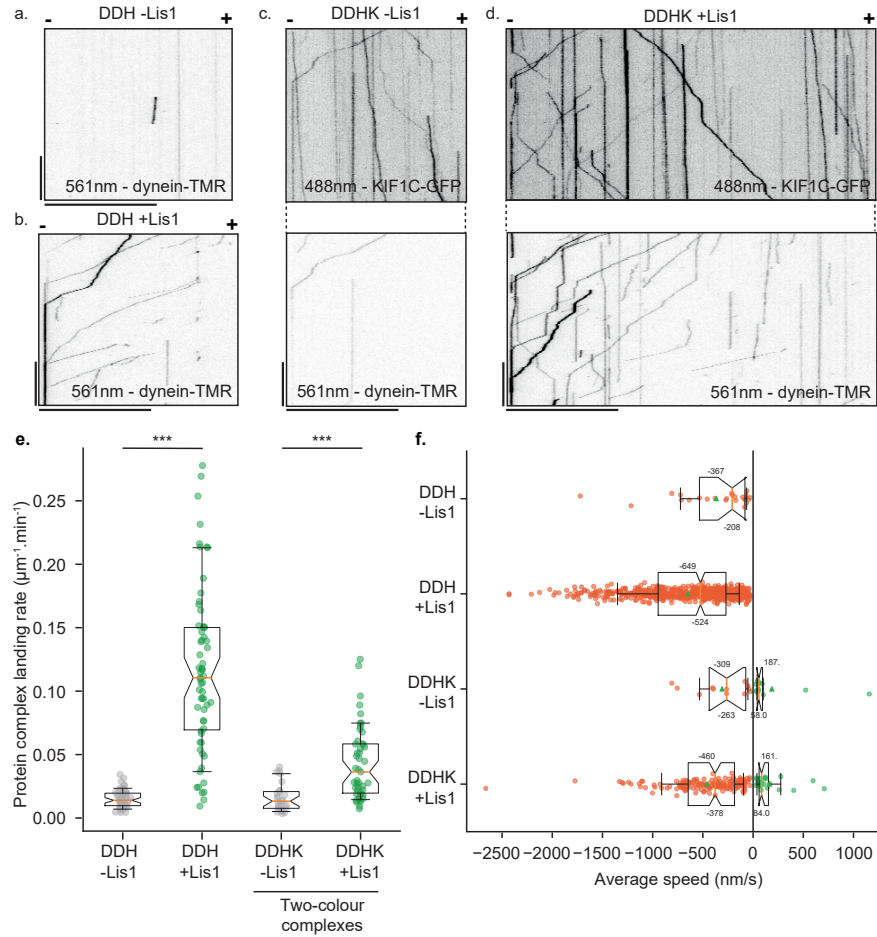
Figure 5.10: Effect of Lis1 on DDH complex formation | a-d. Kymographs of DDH in the presence and absence of Lis1 and KIF1C-GFP. **e.** Landing-rate of DDH or DDHK on to microtubules in the presence and absence of Lis1, where DDHK measurements only include two-colour complexes of dynein-TMR and KIF1C-GFP. Dots represent per-microtubule measurements, *** indicates p ≤ 0.001 **f.** Speeds of DDH and DDHK in the presence or absence of Lis1, showing that the average minus-end directed speed increases.

5.4   Transport of dynein and KIF1C co-complexes towards the minus-end

To fully understand the microtubule running characteristics of dynein and KIF1C co-complexes, we first considered transport only towards the minus-end of the microtubule. We sought to answer several key questions: Does linkage of KIF1C and dynein negatively impact the minus-end directed transport of complexes? Does KIF1C fight against the motion of dynein, or is the presence of KIF1C beneficial? Is KIF1C a passive passenger of dynein, or does it interact with the microtubule during minus-end directed runs?

To understand the role of the kinesin motor activity in this arrangement, we generated complexes of DDH in the presence of a short-region of KIF1C's stalk (KIF1C-stalk-GFP) or full-length KIF1C-GFP motors (KIF1C-FL-GFP; see Figure 5.11 a-c.). The KIF1C-stalk-GFP construct included the interaction site of Hook3 which we earlier mapped by BioID, and so we anticipated this would be sufficient to form complexes with DDH while missing the kinesin motor domain, and thus would be incapable of generating opposing force.

We found that dynein-dynactin complexes created with gel-filtered untagged Hook3 and Lis1 were robustly activated and undertook rapid transport on microtubules (see Figure 5.11 d.). Addition of KIF1C-stalk-GFP generated two-colour co-migrating complexes of dynein and KIF1C stalk on the microtubule, and these had a uniform minus-end directed motility (see Figure 5.11 e.). As previously observed with Alexa-647 tagged Hook3, untagged Hook3 was able to generate co-complexes of full-length KIF1C-GFP and dynein, and these complexes showed both plus- and minus-end directed motility (see Figure 5.11 f.). The tracks made by DDH, dynein-dynactin-Hook3-KIF1C-stalk (DDH-KS), and DDHK complexes were captured manually from kymographs by tracing the paths along their length (as shown in Figure 5.11 g.). Unless explicitly specified, all data pertaining to kinesin-dynein co-complexes in this section arise from traces where signal is present in both the 488 and 561 channels, as indicated by the green tracks in the example trace shown in Figure 5.11 g.

Analysis of the landing rate of motor complexes revealed that the formation of co-complexes of dynein with full-length KIF1C was less efficient than of dynein with KIF1C-stalk, while the landing rate of DDH-KS also appeared to be higher than DDH, indicating that KIF1C's stalk domain had an
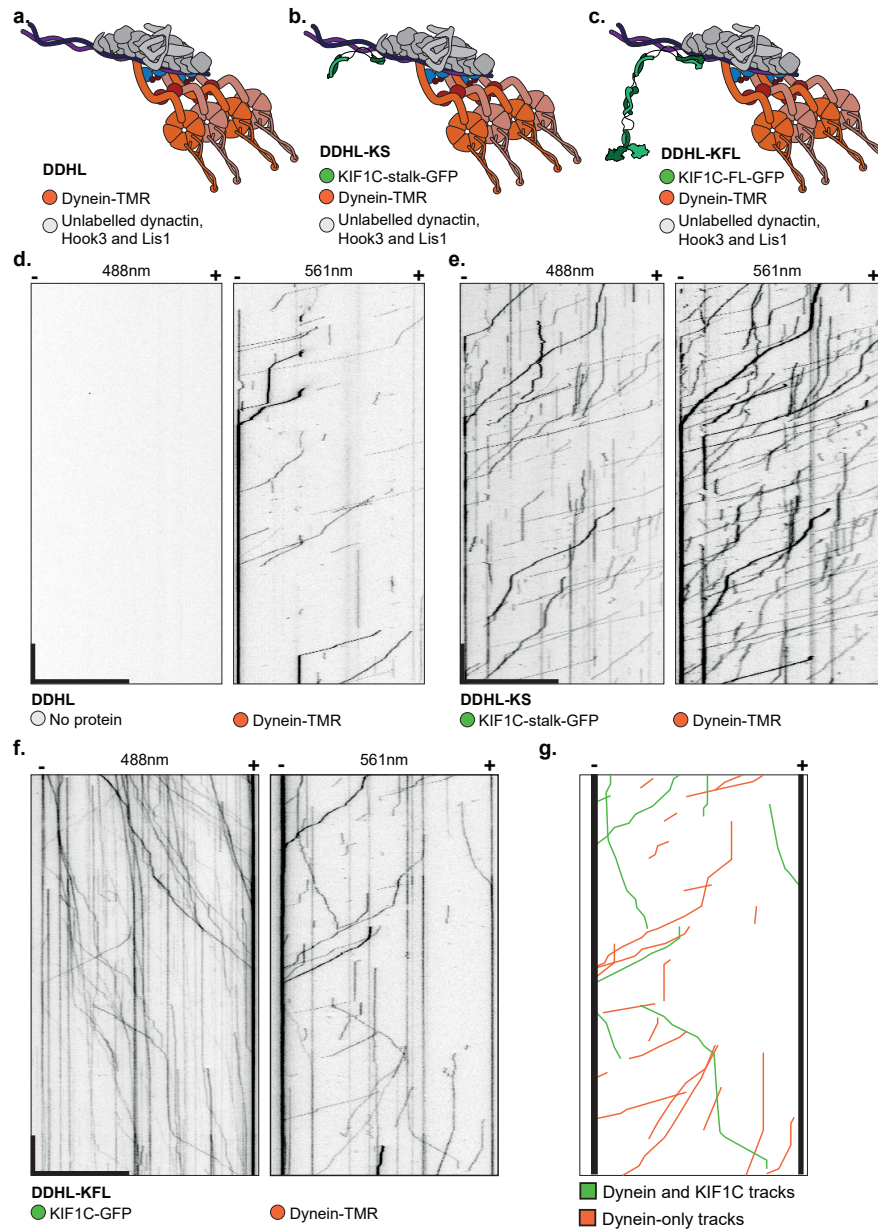
Figure 5.11: Kymographs of dynein-dynactin-Hook3 complexes in the presence of Lis1 and KIF1C-FL or KIF1C-stalk | a-c. Schematic diagrams of protein complexes formed in the following experiment, where **a.** is dynein-dynactin-Hook3-Lis1 (DDH), **b.** is DDH in the presence of KIF1C-stalk-GFP (DDH-KS), and **c.** is DDH in the presence of KIF1C-FL-GFP. **d-f.** Kymographs generated from microscopy recordings of the indicated complexes, where the scale bar represents 20s and 20µm in the vertical and horizontal axes. **g.** Annotated tracks from DDHK kymographs showing plus- and minus- directed motor complexes.

activating effect on the recruitment of dynein to the microtubule (see Figure 5.12 a.). Indeed, by considering all dynein-containing tracks on the microtubule instead of only those containing both dynein and KIF1C signals, we found that KIF1C-stalk elicits a 3.6x increase in dynein landing rate from 0.136 ± 0.067μm^{-1}min^{-1} to 0.497 ± 0.151μm^{-1}min^{-1}, whereas in KIF1C-FL experiments dynein molecules landed 1.5x more frequently, increasing to 0.209 ± 0.087μm^{-1}min (see Figure 5.12 b.). Landing rate typically increases when complexes or cargoes have more microtubule-binding domains, and so we expect that DDHK complexes would have more opportunity to engage with microtubules. On the contrary, our data show that the stalk domain of KIF1C is sufficient to increase the landing rate of dynein, and this effect does not require the KIF1C motor domain, therefore KIF1C-stalk most likely causes activation of dynein/dynactin at the level of complex formation, or by positioning dynein motors or dynactin's p150 to be more able to interact with the microtubule.

We also measured how long motor complexes were able to stay on the microtubule, or the so-called "dwell time". The presence of full-length KIF1C, but not KIF1C stalk, was able to increase the dwell time of motor complexes on the microtubule almost two-fold, showing that the motor domain of KIF1C does interact with the microtubule from within the DDHK complex and in doing so, provides additional microtubule-binding affinity (see Figure 5.12 c.).

The idea that motors undertake a tug-of-war is central to current theories of how kinesin and dynein are able to undertake bidirectional transport (Belyy et al., 2017; Hancock, 2014; Hendricks et al., 2010; Soppina et al., 2009). To understand whether KIF1C caused a negative impact on dynein's motility, we investigated the run speeds and run lengths of the motor complexes. We hypothesised that if KIF1C was opposing the transport of dynein, it would result in considerably shorter run lengths and run speeds on microtubules. We found that DDH and DDH-KS run speeds were not significantly different, while DDHK run speeds were significantly slower, decreasing from 759 ± 180nm/s for DDH to 639 ± 266nm/s for DDHK (see Figure 5.13 a. for individual-motor level, and c. for experimental-level).

In the presence of KIF1C stalk or full-length motor protein, the run length of DDH complexes, however, increased significantly, and this increase was largest for the full-length motor which went from an average run length of 7,591 ± 3,345 nm in control experiments to 10,622 ± 5,323 nm for DDHK (see Figure 5.13 b. for individual-motor level, and d. for experimental-level).

102
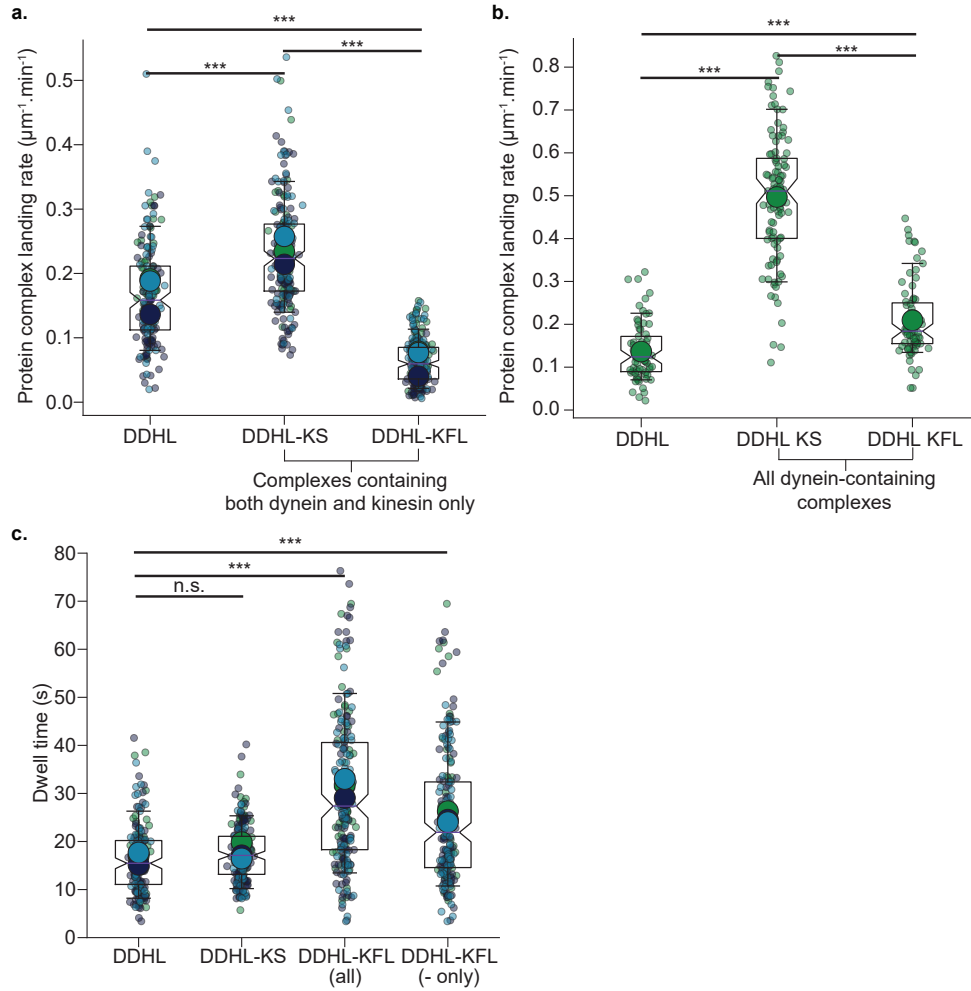
Figure 5.12: Landing rate and dwell-times of DDH complexes containing KIF1C-stalk and KIF1C-FL | a. Superplot showing landing-rates of DDH in the presence of KIF1C-stalk-GFP or KIF1C-FL-GFP, where transparent dots indicate single microtubules and large dots indicate experimental averages. For analysis of DDH-KS and DDHK, only complexes which contain signal in both the 488 and 561 channels are considered. **b.** Plot of a separate analysis of landing-rate where all dynein-containing complexes (any particle with signal in the 561 channel) have been included. **c.** Superplot showing dwell time of motor complexes on microtubules. n.s. indicates p > 0.05, * indicates p ≤ 0.05, ** indicates p ≤ 0.01 and *** indicates p ≤ 0.001.
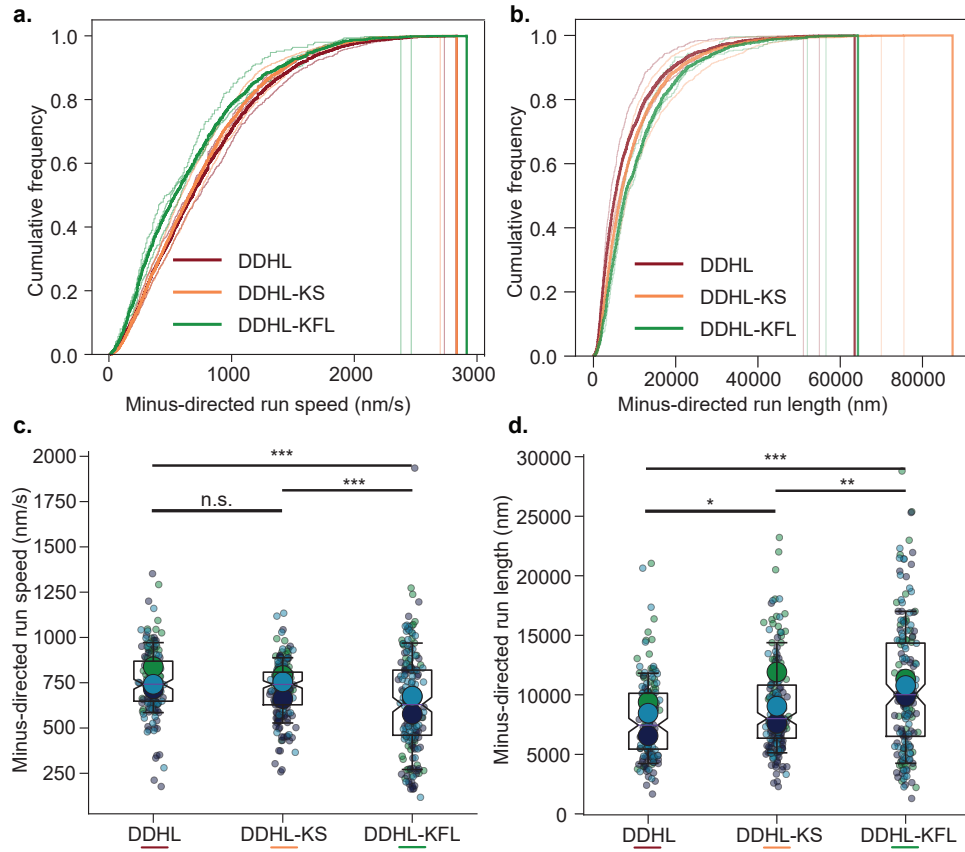
Figure 5.13: Run-speeds and run-lengths of DDH complexes with KIF1C-FL and KIF1C-stalk | Cumulative frequency plots of **a.** Minus-directed run speeds and **b.** minus-directed run lengths of DDH, DDH-KS and DDHK complexes at the individual motor level. The transparent lines indicate individual experiments, while the bold line is the average of multiple experiments. The vertical lines represent the maximal value for each experiment. **c-d.** show the run speeds and run lengths as superplots, where the transparent dots indicate per-microtubule average values, and the large dots indicate per-experiment average values. n.s. indicates p > 0.05, * indicates p ≤ 0.05, ** indicates p ≤ 0.01 and *** indicates p ≤ 0.001.

The increase in landing rate and run length of motor complexes in the presence of KIF1C and KIF1C stalk was intriguing, as it suggested one of two things. Either the presence of KIF1C stalk within DDH complexes rearranged the motors to be more capable of engaging with the microtubule, for example by acting similarly to Lis1 by relieving the autoinhibition of dynein, or instead the KIF1C stalk could be promoting the formation of dynein complexes containing two dynein dimers instead of one. To investigate this, we looked at the intensities of running motors on the microtubule.

Motor intensities could be measured in several ways, for example, Gaussian functions could simply be fit to spots within the TIRF microscopy recordings, however this would lose vital information we already have at the individual motor level such as run lengths, speeds and landing rates. For this reason we chose to integrate the analysis of motor intensities into our existing kymograph analysis pipeline. In order to do this, several reverse engineering steps were necessary. Firstly, regions of interest (ROIs) from which kymographs were originally generated needed to be mapped back to the original movies, and must be checked to see if they have been reflected during motor tracing as the minus-end is always set to the left-hand side of the kymograph during analysis so that minus- and plus- end direction motion can be separated. To test whether kymographs had been reflected, original microtubule ROIs were use to generate new kymographs from the TIRF recording, and compared with the kymograph from which the motor tracing analysis had been performed. The absolute value of the per-pixel intensity differences was calculated between the two kymographs, and the mean difference was used to determine whether the images had been manipulated. The mean intensity value of the subtracted images approached 0 if the images had not been changed, and was greater if they had been reflected.

To map motor traces back to the original microtubule position within images, we interpolated the line ROIs of the microtubule and of the motor trace at 0.5 pixel increments and mapped the X position of the motor traces back to their closest point along the microtubule in the original movie. Where kymographs had been reflected, the motor traces were also reflected horizontally so that their relative position in the original movie would be correct. The approximate (X, Y, T) positions of motors in the original movie was recorded and used to determine the point where intensity measurements should be taken.

In a subsequent step, all (X, Y, T) points were visited in all channels of the original microscopy recording and a 2D Gaussian function was fitted
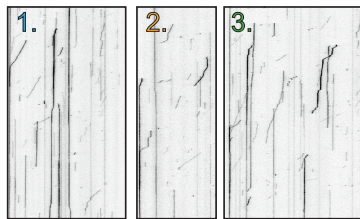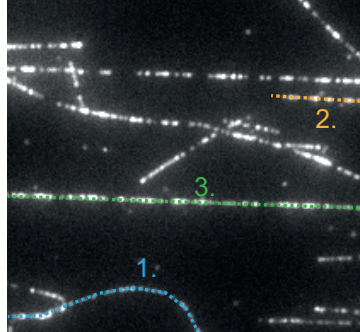
105

within a 5x5 pixel rectangle sub-region. The exact point, Gaussian width, local background and integrated spot intensity were recorded in a way that filenames could easily be mapped back to the motor traces. The success rate of fitting these spots varied as the manually segmented microtubule backbone and motor traces were not always running directly along the centre of the signal, and so downstream filtering of the Gaussian fits was required.

Within our Python motor analysis pipeline, Gaussian fits were paired up with their respective tracks, and the data were filtered for quality. We chose to discard any particle measurements where the Gaussian width was more than 400nm, as this could occur from having multiple spots within the same 5x5 pixel fit region and thus would skew intensity data. In addition, we calculated the signal-to-noise ratio as the integrated intensity of the spot divided by the local background calculation, and discarded any spots which did not have a signal-to-noise ratio of above 5. It should be noted that these background values already accounted for the offset of the camera which had a baseline of around 3000 AU, and so typical background values were in the region of 0-1000.

Using the newly generated motor fitting analysis pipeline, we fit 2D Gaussians to dynein signals within running DDH complexes, as well as complexes which also contained KIF1C-stalk and KIF1C-FL, in order to find out whether an increase in the number of dynein dimers might explain the increased landing rate and run length that had been observed. The average intensity values increased 1.2 or 1.5 fold in the presence of KIF1C stalk or full length motor respectively, indicating an increase in the average amount of dynein contained within complexes (see Figure5.15 a.). By comparing complex intensity values to their run lengths, we found that for all complexes the run length correlated to their dynein intensity and that these correlations were statistically significant, despite being of a small magnitude, with Pearson R values of 0.17, 0.11 and 0.11 for DDH, DDH-KS and DDHK respectively (see Figure 5.15 b). Therefore we concluded that an increase in the dynein occupancy within complexes in the presence of KIF1C or KIF1C-stalk contributes to the increased landing rates and run lengths observed, as well as partially explaining the longer dwell time of these complexes.
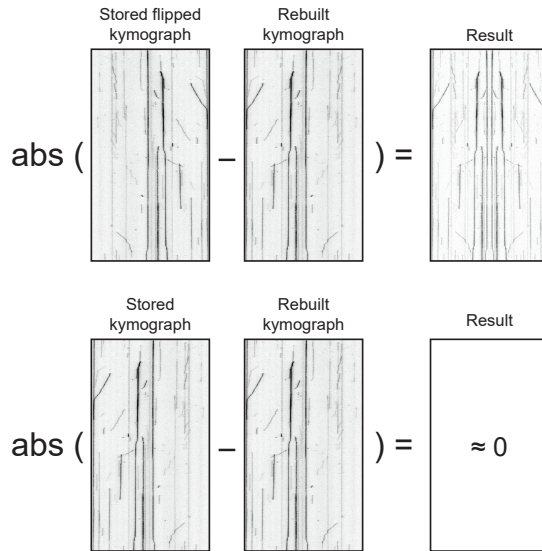
In summary, the presence of either full-length KIF1C or KIF1C stalk was able to increase the landing rate and run length of dynein within DDH complexes. The full length kinesin appeared to interact with the microtubule during transport, as evidenced by increased dwell times of complexes on the

1. Kymographs re-built from stored ROIs using the channel where motors were traced

2. Kymographs checked for horizontal flipping which may have occured during motor tracing

Stored flipped kymograph   Rebuilt kymograph   Result

abs (–) =

Stored kymograph   Rebuilt kymograph   Result

abs (–) = ≈ 0

* For representation only, not the actual kymographs collected from the image.

3. Motor traces corrected if flipped, and sampled every 0.5 pixels to find X position over time.
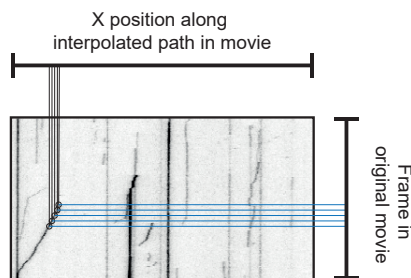
4. Original X, Y, T in movie determined by finding where the X value fits within the microtubule's interpolated path.

X position along interpolated path in movie

Gaussian function fit using a 5x5 pixel search area at the precise X, Y positions in the movie for each time point.

Frame in original movie
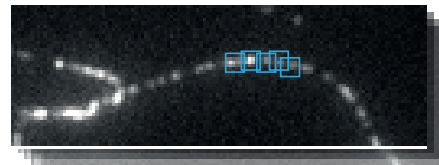
Figure 5.14: Fitting intensities to moving motors from kymograph traces | Schematic showing how annotated motor traces are converted into fitting spots within an original TIRF movie. First, a reference kymograph is generated and compared to the kymograph which was used when tracing motors, as the kymographs which are used to trace motor's tracks are flipped horizontally so that the minus-end of the microtubule always appears to the left side of the image. After determining if the kymograph has been flipped, the trace is interpolated every 0.5 pixels and the X and T values are found. These X and T values are mapped back to the microtubule's path in the original movie to find the X, Y and T positions in the movie where the spot that created the kymograph signal would appear. A 5x5 pixel square is used constrain the fitting of a 2D Gaussian to the fluorescent spot, and the fit parameters as well as the integrated intensity are recorded.

107
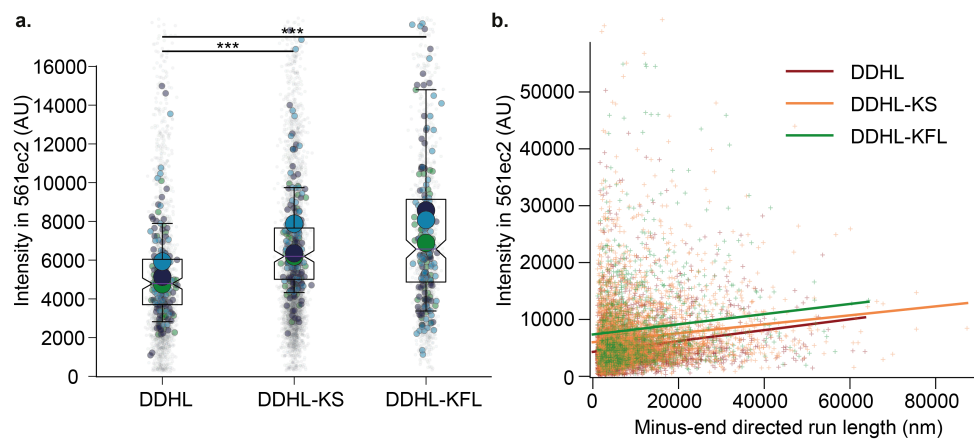
Figure 5.15: Intensity measurements of moving dynein complexes in the presence of KIF1C stalk and motor | a. Average integrated intensity measurements from 2D Gaussian fits to dynein-TMR signal within DDH complexes formed with KIF1C-stalk or KIF1C-FL. The smallest most transparent points indicate individual motor complex intensity values, while the larger dots indicate per-microtubule averages, and the largest dots show experimental averages. **b.** Plot of individual motors run lengths compared to their integrated intensity, with a polynomial fit showing that complex run length is weakly correlated to dynein-TMR brightness. Correlation coefficients were calculated with a Pearson R test and found to be 0.17, 0.11 and 0.11 for DDH, DDH-KS and DDHK respectively. Each correlation was found to be statistically significant with a two-tailed permutation test, each having a *p*-value of ≤ 8x10^{-5}. ******* indicates p $\leq$ 0.001.

microtubule, as well as a small decrease in the minus-directed run speeds of the complexes compared to controls. The presence of KIF1C allowed DDH complexes to achieve longer average run lengths overall despite slowing them down, as although the complexes were moving slower they remained on the microtubule for longer. Thus KIF1C has an overall positive effect on the transport of DDH towards the minus end of the microtubule, providing direct evidence for cooperation of opposite polarity motors.

5.5 Transport of dynein and KIF1C co-complexes towards the plus-end

We next sought to investigate whether dynein had a positive effect on the plus-end directed transport of KIF1C, or whether a tug-of-war occurred. To test this we generated complexes of DDHK and variations of this complex where dynein was removed (xDHL-KFL), dynein was replaced by a dynein-tail construct (DtDHL-KFL), or where both dynein and dynactin were not included at all (HK; see Figure 5.16 a-c.)

In all complexes where full-length dynein was omitted, KIF1C-GFP remained active and moved unidirectionally towards the plus-end of the microtubule (see Figure 5.16 a-c.), whereas experiments with DDHK remained bidirectional as previously shown.

Interestingly, KIF1C had a much higher landing rate in the presence of complexes formed with dynein tail domain or full-length dynein, increasing 2-3 fold from KIF1C-Hook3 controls. The absence of dynein tail decreased this effect but did not abolish it, suggesting that both the dynein tail and dynactin contribute to KIF1C activation (see Figure 5.17 a.). The presence of dynein or dynactin did not appear to have a significant effect on the dwell time of KIF1C, showing that the residency time of plus-end directed complexes on microtubules is primarily determined by KIF1C (see Figure 5.17 b.).

When considering the plus-end directed run lengths and run speeds at the single motor level and per-microtubule level, we found that DDHK complexes moved slower and undertook shorter runs than complexes where full-length dynein was absent (see Figure 5.18 a-d.), indicating that dynein exerts a negative effect on plus end directed transport by KIF1C.

The effect on landing rate could again be attributed to a change in the stoichiometry of the complex, and so the intensity of KIF1C was measured
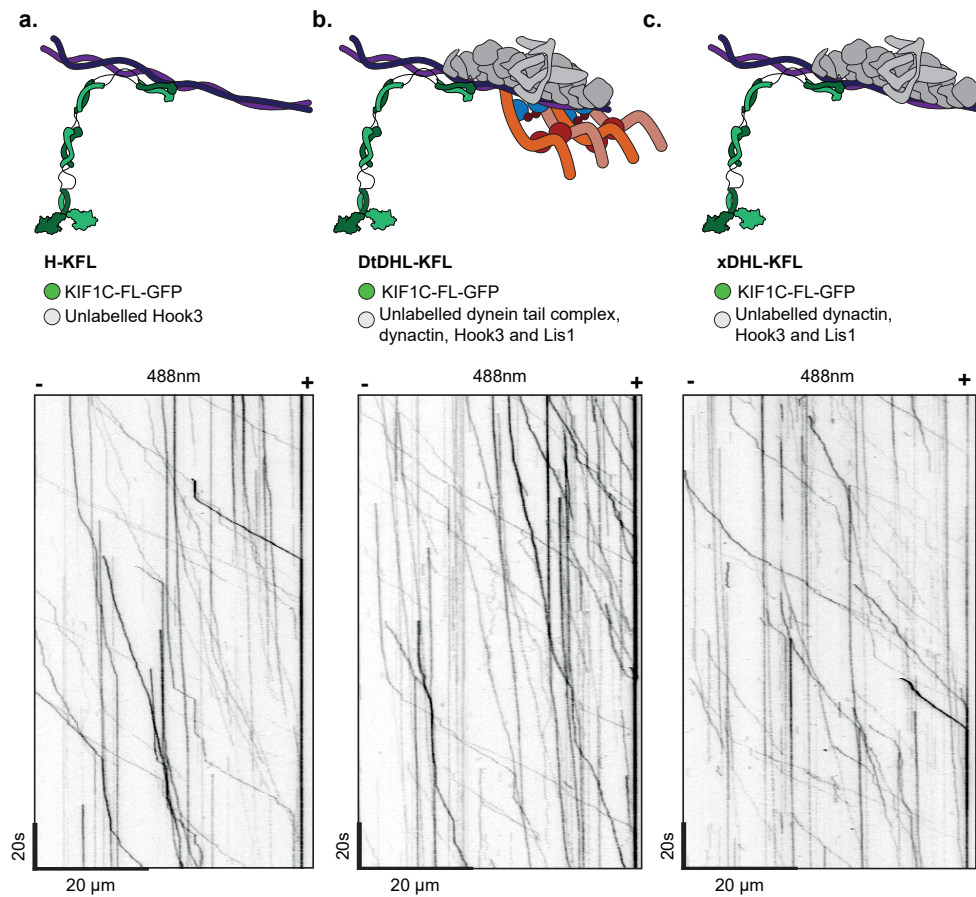
Figure 5.16: Plus-end directed complexes of KIF1C | a-c. Schematic diagrams of possible complexes formed in the following experiments, as well as kymographs generated from KIF1C-GFP, where **a.** is Hook3 and KIF1C only (HK), **b.** is Hook3, KIF1C and dynactin formed in the presence of dynein's tail domain (DtDHL-KFL), and **c.** is DDHK but formed in the absence of full-length dynein.
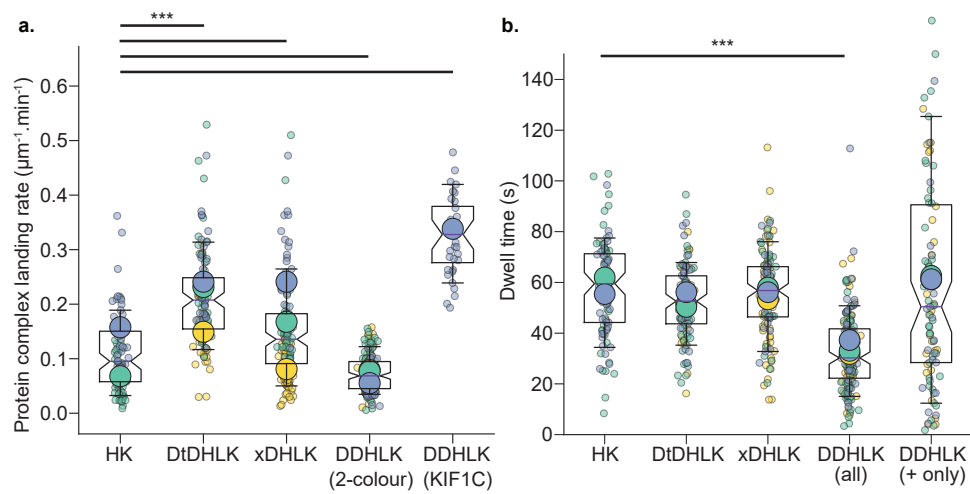
Figure 5.17: Landing rates and dwell times of plus-end directed dynein and KIF1C complexes | a. Superplot of landing rates of the indicated complexes. **b.** Superplot of dwell times of the indicated complexes. Each small transparent dot represents a single microtubule, whereas the larger dots represent experimental averages. The range of the whiskers presented in the box plot is between the 10th and 90th percentile of the data, while the upper and lower bounds of the box represent the 75th and 25th percentiles respectively. *** indicates $p \leq 0.001$.
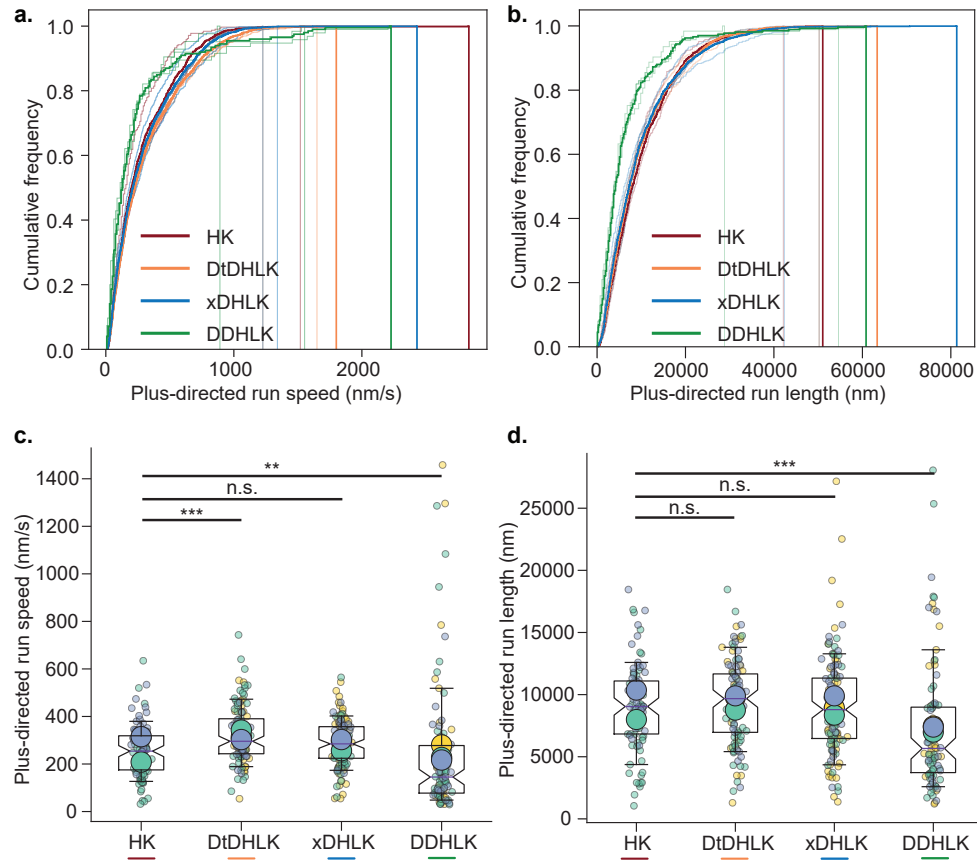
Figure 5.18: Run-speeds and run-lengths of DDHK complexes with dynein tail | a-b. Cumulative frequency plots at the individual motor level showing plus-end directed run-speeds and run-lengths of the indicated protein complexes. The protein complexes are iterations of dynein, dynactin, Hook3, Lis1 and KIF1C (DDHK) where dynein has either been removed (xDHLK) or replaced with dynein tail (DtDHLK). "HK" is a complex of KIF1C and Hook3 made in the absence of dynein, dynactin and Lis1. The vertical lines represent the maximal value measured for each dataset. **c-d.** Superplots of the same datasets, where small transparent dots represent average values for kymographs, while larger dots represent the experimental average. n.s. indicates $p > 0.05$, * indicates $p \leq 0.05$, ** indicates $p \leq 0.01$ and *** indicates $p \leq 0.001$.

using the same 2D Gaussian fitting process described previously. The average KIF1C intensity almost doubled within full complexes of DDH as well as in complexes made in the presence of dynein's tail domain, while in the absence of dynein (but presence of dynactin), there was a smaller but statistically significant increase in average intensity (see Figure 5.19 a.). This raised the possibility that DDHK complexes could contain two KIF1C dimers, just as they contain two dynein dimers, and that both dynein and dynactin seemed to be important in stabilising the interaction of the second KIF1C dimer. However, GFP fluorescence is also known to be context dependent, for example, binding of a nanobody to GFP increases its brightness nearly two-fold, and so we cannot be certain that rearrangement of the GFP within the complex increases its brightness (Schneider et al., 2021). In addition the dwell time of complexes which would appear to contain two KIF1C dimers did not increase as might be expected, and so the exact number of KIF1C molecules within the complex should be determined by a more suitable method such as stepwise photobleaching in future studies. The plus-end directed run lengths of DDHK showed a statistically significant correlation to KIF1C intensities, though the magnitude of this correlation was small (see Figure 5.19 b.). In addition, the intensity of KIF1C within complexes also correlated with the minus-end directed run lengths of DDHK complexes (see Figure 5.19 c.), reinforcing our previous findings that the presence of KIF1C improves the run characteristics of dynein.

Taken together, these data show that when transported towards the plus-end of the microtubule, dynein undertakes a tug-of-war with KIF1C that results in shorter run lengths and run speeds. The presence of dynein and dynactin does, however, increase the overall landing rate of plus end directed complexes onto microtubules. DDHK complexes may contain two KIF1C dimers, and the plus-end directed run length correlates with the intensity of KIF1C suggesting that two KIF1C dimers are more capable of opposing dynein, though a more quantitative analysis of KIF1Cs stoichiometry within the complex must be performed. Interestingly, the minus-end directed run length of DDHK complexes also correlated with KIF1C intensity, reinforcing the idea that KIF1C primary role in the complex is to increase the performance of dynein.
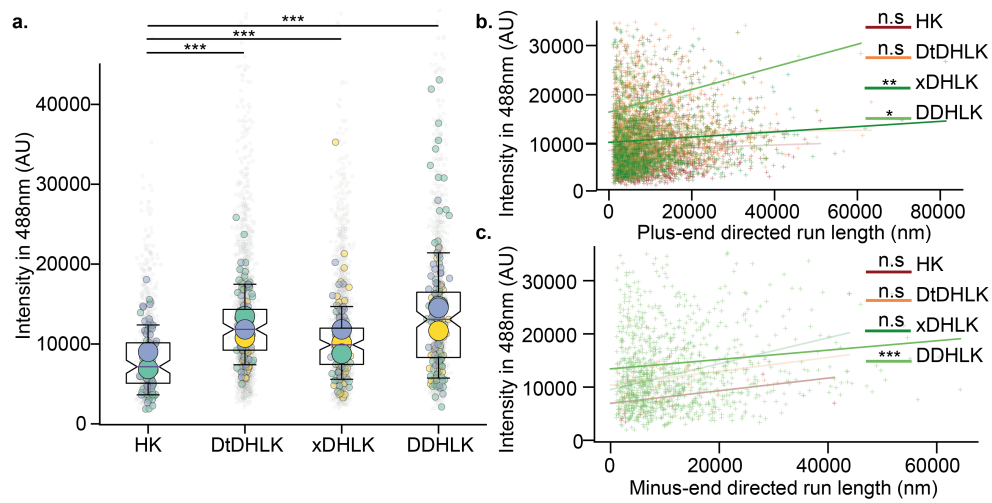
Figure 5.19: Intensity of KIF1C within dynein complexes | a. Superplot of running KIF1C motor intensities within the indicated complex mixtures, where the most prominent coloured spot shows an experimental average, the smaller spots show per-microtubule averages, and the feint small spots show average values for individual motors. **b.** Correlation of KIF1C intensity with complex run lengths towards the plus-end of microtubules. xDHK and DDHK show a statistically significant positive correlation with Pearson r-values of 0.07 and 0.15 respectively. **c.** Correlation of KIF1C intensity with complex run lengths towards the minus-end of microtubules. Only DDHK shows a statistically significant positive correlation, with a Pearson r-value of 0.21. n.s. indicates p > 0.05, * indicates p $\leq$ 0.05, ** indicates p $\leq$ 0.01 and *** indicates p $\leq$ 0.001.

5.6 Directionality of dynein and KIF1C co-complexes

Kymographs clearly showed that DDHK complexes had a minus-end directed bias. We quantified the proportion of tracks that are plus- or minus- end directed, static, or bidirectional using the criteria shown (see Figure 5.20 a-b.). A small proportion of motor complexes showed bidirectional motility, travelling over 1.5 µm towards both the plus- and minus- ends of the microtubule (see Figure 5.20 c-d.). To ensure that these directional changes were genuine, and did not occur from arrangement of the microtubules in anti-parallel bundles, an excess of KIF1C-GFP was flowed into the imaging chamber following imaging of DDHK complexes. The presence of large amounts of KIF1C-GFP travelling unidirectionally confirmed the microtubule polarity.

We observed from kymographs that DDHK complexes often seemed to pause in a manner similar to KIF1C's stop-start motility (refer back to Figures 5.11 and 5.16 for example kymographs). This was interesting as it appeared that dynein was inheriting some of the characteristics of KIF1C in its mode of motility. To understand this further, we subdivided motor tracks to determine how much time they spent undertaking plus or minus-end directed transport, and how long they spent paused (see Figure 5.21 a.). The unidirectional complexes, KIF1C-Hook3 (HK) and DDH, showed the expected biases in plus- and minus- end directed transport (see Figure 5.21 b-c.), though DDHK complexes spent on average 18% more time travelling towards the minus-end of the microtubule, echoing the previous findings of its increased dwell time and run lengths. Crucially, DDHK complexes spent much longer in a paused state than DDH, and were on average paused for a similar amount of time as KIF1C-Hook3. As entirely static motors were excluded from this analysis, and pausing at the plus- or minus- ends of microtubules is not captured in our analysis, this increase in pausing came from the stop-start motility which could be observed in kymographs.

The exact reasons for this stop-start motility can only be speculated on. Perhaps KIF1C is able to prevent dynein's detachment from the microtubule that would usually occur after a processive run. Perhaps these pauses are short moments where the two motors oppose each other in a tug-of-war. Whatever their origin, however, these pauses act to increase the dwell time of the complex overall and may in part explain why dynein is able to undertake overall longer run lengths in the presence of KIF1C as has been described earlier.

a. (Bar plot)

80%
16%
1.9% 2.1%

+   -   Static   Bi

% of DDHLK complexes

b. Directional classifications

Plus	Minus
0 minus-end runs and >1 plus-end run **or** Not bidirectional and plus-end run distance more than minus-end run distance	0 plus-end runs and >1 minus-end run **or** Not bidirectional and minus-end run distance more than plus-end run distance

Static	Bidirectional
Total distance < 1000 nm	Plus-end distance >1500nm **and** Minus-end distance >1500nm

c.
- 488nm + - 561nm + -   +
KIF1C-GFP   dynein-TMR   - Polarity check +

d.
- 488nm + - 561nm + -   +
KIF1C-GFP   dynein-TMR   - Polarity check +

Figure 5.20: Bidirectionality of DDHK complexes | a. Bar plot of proportions of motor complexes which showed either plus-end or minus-end directed motility, remained static, or were bidirectional. Bar height is the mean value of three experiments, and error is standard deviation between experimental repeats. **b.** The criteria applied to determine which class motor complexes belonged to. **c-d.** Example kymographs of bidirectional motor complexes, along with a "polarity check" where an excess of KIF1C-GFP was flowed into the imaging chambers after DDHK was imaged to check that bidirectional runs did not occur because of arrangement of the microtubule(s) (e.g. in anti-parallel bundles).
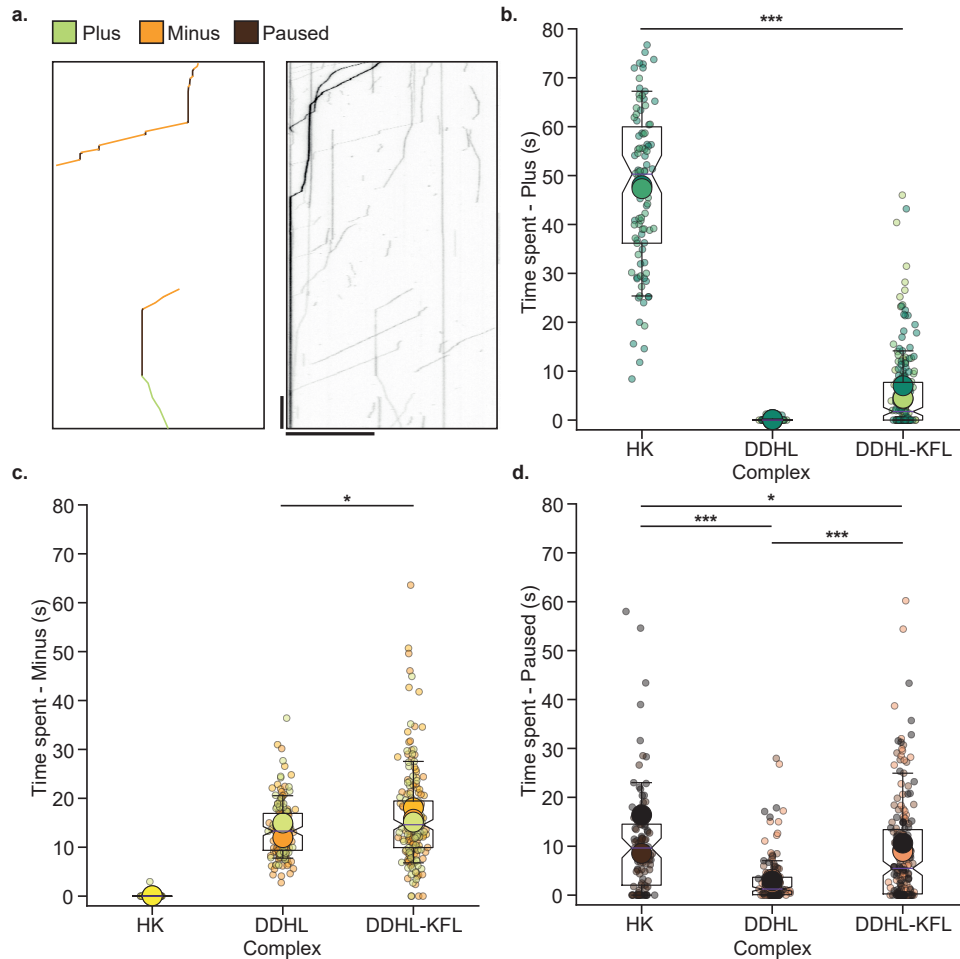
Figure 5.21: Sub-classification of motor complex motility and pausing events | a. Example kymograph and annotation showing what would be classified as plus-, minus- and paused motility. The example is the dynein-TMR channel of a DDHK chamber. The scale bar is 20μm and 20s in the horizontal and vertical axes respectively. **b-d.** A breakdown of HK, DDH and DDHK time spent moving towards the plus- and minus- ends of the microtubule, or spent pausing at a speed < 20nm/s. Note that wholly static tracks (total distance < 1000nm) are excluded from this analysis.

5.7 FHF complex

Research into Hook3-driven dynein motility *in vitro* has typically been limited to constructs containing the dynein-binding portion of Hook3 in the amino acid region 1-552, presumably as these simplify an already complex reconstitution, and perhaps in part due to the difficulties described here in purifying full-length Hook3 (Schroeder & Vale, 2016; Urnavicius et al., 2018). More recently, we and others have extended reconstitution to the full-length Hook3 dynein adaptor in this work and in published works (Kendrick et al., 2019; Siddiqui et al., 2019). However, an added layer of complexity exists. Inside the cell, the Hook dynein adaptors (Hook1, Hook2, and Hook3) are known to form a tripartite complex with Fused Toes (FTS) (also known as AKTIP) combined with FAM160A2 (previously named p107FHIP) (Xu et al., 2008), and this is known as the FAM160A2/Hook/FTS (FHF) complex. There is much still to be determined about how exactly the FHF complex works inside of cells, however, we sought to understand whether complex formation with dynein and KIF1C was still possible with fully formed FHF complex *in vitro*.

Our collaborators in Andrew Carter's lab were able to express, purify and label the FHF complex formed with Hook3, placing an Alexa-647 fluorophore to a SNAPf tag attached at the N-terminus of Hook3, and this was provided as a reagent for use in our single-molecule reconstitution. Importantly, our collaborators had found that purified FHF complex formed a monodisperse peak by gel filtration, and this peak contained all three components of the FHF complex. Furthermore, FHF formed a stable complex with KIF1C stalk domain that could be run over gel filtration to demonstrate that it contained all 4 proteins. Therefore we could use the Alexa-647 labelled FHF complex and be confident that the observed 647 signal was from FHF complexes and not from individual Hook3 molecules.

We first sought to reconstitute the KIF1C:Hook3 interaction using FHF-647. 90 nM of KIF1C-GFP was incubated with either 600 nM of FHF-647 or buffer control, and then diluted 1:40 into TIRF assays to achieve a final concentration of 2.25 nM KIF1C-GFP with 15 nM of FHF-647. Under these conditions we found that KIF1C-GFP was able to co-migrate with FHF (see Figure 5.22 a-b.). Similar to Hook3 alone, FHF-647 was able to increase the landing rate of KIF1C-GFP significantly, although the magnitude of this change was smaller, the mean landing rate increasing by 28% (see Figure 5.22 c.). Unlike Hook3 alone, FHF-647 appeared to have some effect on the

118
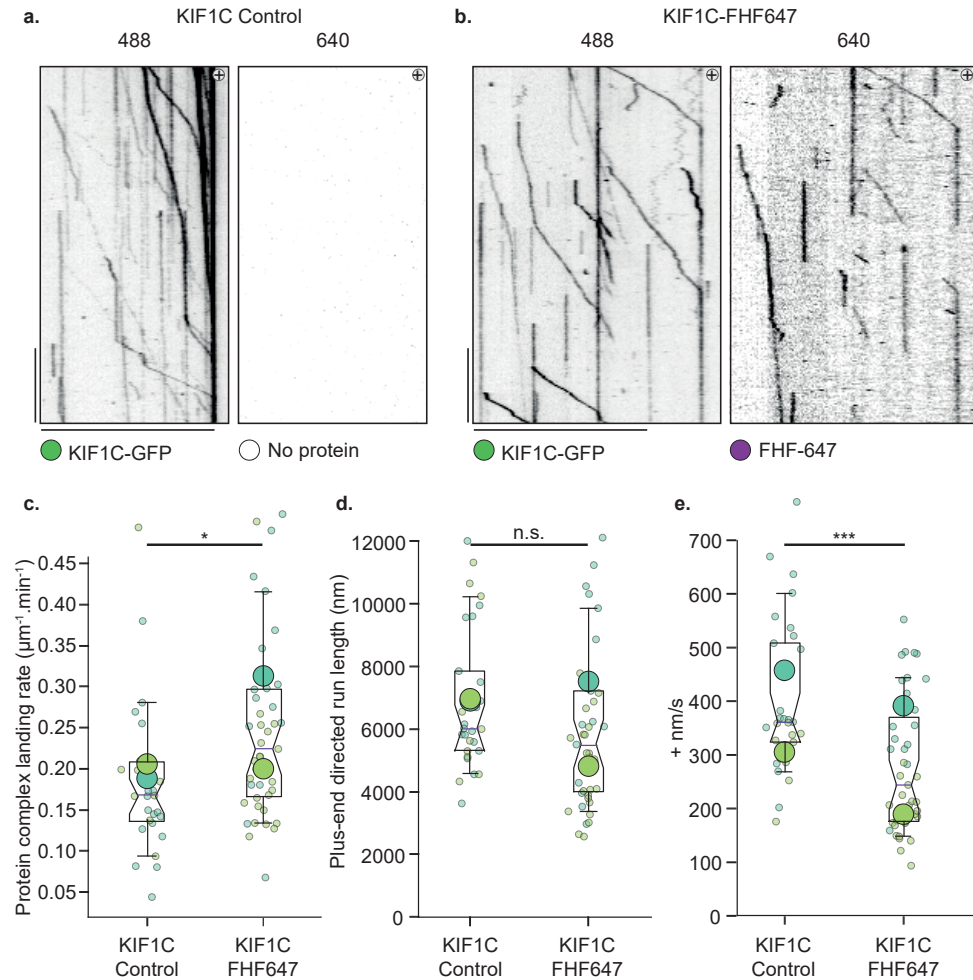
Figure 5.22: KIF1C motility with FHF complex | a-b. Kymographs of KIF1C-GFP in the presence of FHF-647 or buffer control. Scale bar represents 20s and 20μm in the vertical and horizontal axes. **c.** Quantification of the landing rate of KIF1C-GFP in the presence or absence of FHF-647. **d.** Quantification of the run length of KIF1C-GFP in the presence or absence of FHF-647. **e.** Quantification of the run speed of KIF1C-GFP in the presence or absence of FHF-647. In all cases, the small transparent dots are averages from individual microtubules while the larger dots are means of the technical replicate (i.e. per imaging chamber). n.s. indicates p > 0.05, * indicates p ≤ 0.05, ** indicates p ≤ 0.01 and *** indicates p ≤ 0.001.

run characteristics of KIF1C. Run lengths of KIF1C-GFP in the presence of FHF were not statistically significantly different (see Figure 5.22 d.). However, a statistically significant decrease in run speeds was observed for KIF1C in the presence of FHF (see Figure 5.22 e.). In these experiments, FHF appeared to slightly decrease the effectiveness of KIF1C's motility while also acting to slightly increase its activation and landing on the microtubule, however these data arise from just two experiments where the difference in experimental means was very large. More experiments are required to determine the exact effect of FHF on KIF1Cs run lengths and speed.

We found we were unable to form complexes of dynein, dynactin and FHF-647 when pre-incubating 100 nM of each dynein/dynactin with 1 µM FHF-647 and subsequently diluting 1:40 into TIRF assays, whereas Hook3-647 did so robustly at this concentration (data not shown). However, by the addition of 2.5 µM Lis1 during complex formation, and by diluting the complexes less into the TIRF assay (a dilution of 1:20), we were able form activated dynein complexes with FHF-647. This was interesting as it suggested to us that FHF's ability to form dynein complexes might be regulated by the components of the FHF complex in a way that it isn't when Hook3 alone is used.

Complexes of dynein, dynactin and FHF (100 nM, 100 nM and 1 µM) were formed in the presence of 2.5 µM Lis1 with the addition of 200 nM KIF1C-stalk-GFP or 90 nM KIF1C-GFP, and diluted 1:20 into TIRF assays. Fully activated dynein complexes could be seen in the absence or presence of KIF1C components (see Figure 5.23 a-c.), and KIF1C-stalk was clearly able to increase the amount of dynein molecules observed despite the number of co-migrating tracks being low (see Figure 5.23 b.). Co-complexes of full-length KIF1C and dynein were able to form, although at a comparatively low rate, and these most commonly travelled towards the plus-end of microtubules (see Figure 5.23 d.). In analysis of these tracks, 0% bidirectional tracks were observed, but this was due to the high number of KIF1C-GFP molecules on microtubules. As the amount of complex mixture put into imaging chambers needed to be doubled due to the relative inefficiency of observing dynein motors, this meant that despite not changing the ratio of KIF1C-GFP included in complex mixtures, overall KIF1C appeared at higher densities, and this did not allow assignment of bidirectional events with confidence.

To measure the landing rate of dynein, we first considered all tracks which had a dynein-TMR signal regardless of whether KIF1C-stalk or KIF1C signal was also present. Similar to dynein complexes formed with untagged
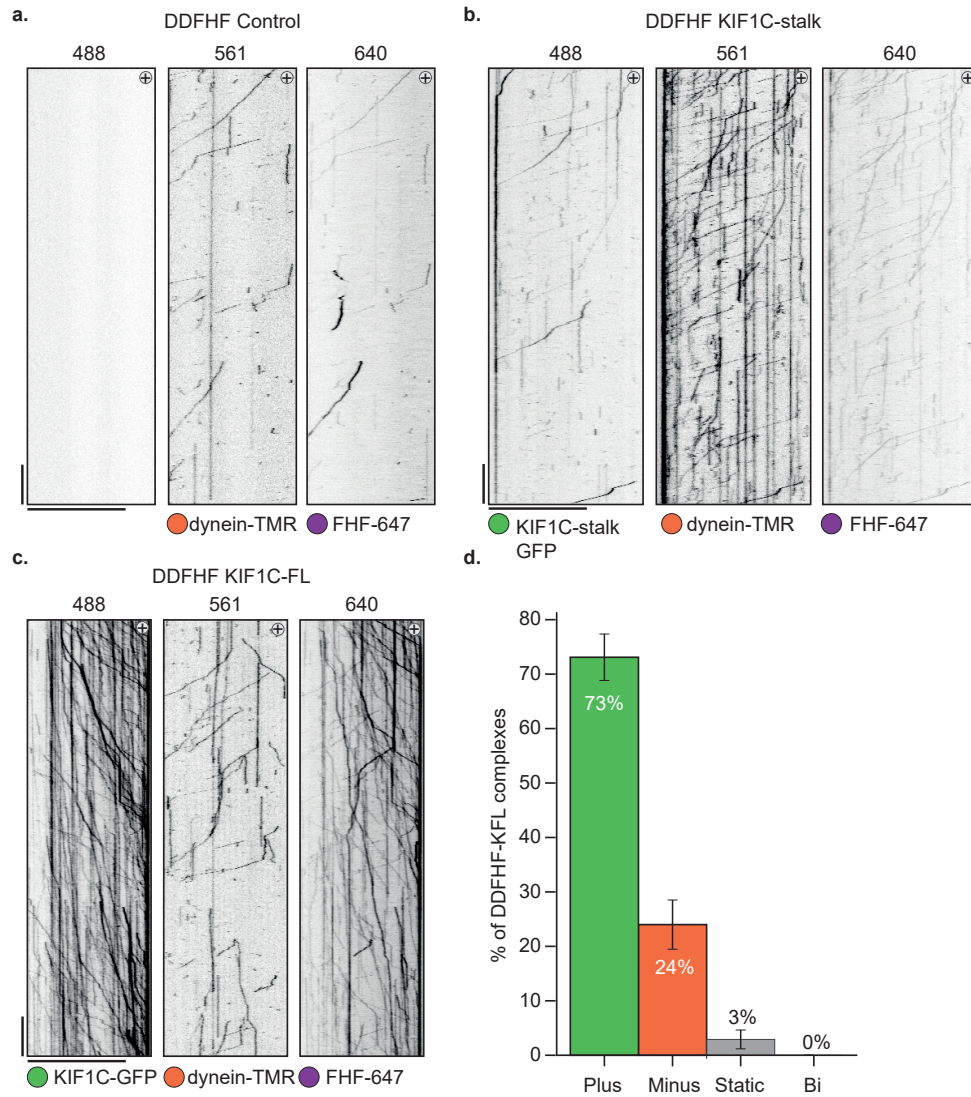
Figure 5.23: Dynein-KIF1C complexes formed with FHF | a-c. Kymographs showing dynein complexes at a final concentration of 5 nM dynein-TMR, 5 nM dynactin, 50 nM FHF-647, 125 nM Lis1 with the addition of 10 nM KIF1C-stalk-GFP or 4.5 nM KIF1C-GFP. **d.** Quantification of the directionality of DDFHF-KIF1C complexes shown as mean of imaging chambers +/- standard deviation between chambers.

Hook3, dynein-dynactin-FHF (DDFHF) complexes formed in the presence of KIF1C-stalk landed around five-fold more often, showing that KIF1C-stalk still had a strong effect on dynein activation when complexes were formed with FHF (see Figure 5.24 a.). Full-length KIF1C was also able to increase the landing rate of dynein almost three-fold (see Figure 5.24).

Interestingly, we observed from kymographs that although the landing rate of dynein had increased, only a small fraction of dyneins co-migrated with either KIF1C-stalk or KIF1C-GFP. The number of 1-colour vs. 2-colour particles was quantified and confirmed that indeed only a minority of dynein molecules co-migrated with KIF1C. This suggested that KIF1C's effect in activating dynein didn't necessarily require KIF1C to remain present, much like Lis1's effect on dynein does not require it to co-migrate with the dynein. Perhaps KIF1C and KIF1C stalk act in promoting the release of dynein from its autoinhibited form, or instead maybe KIF1C acts to help prepare FHF molecules for binding with dynein in some way which we can not directly probe here. Similar to dynein-KIF1C co-complexes formed with Hook3, dynein-dynactin-FHF-KIF1C (DDFHFK) complexes had significantly larger dwell times on microtubules (see Figure 5.24 c.) suggesting that once complexes are formed, KIF1C continues to provide an additional microtubule interaction from within the complex.

Unlike complexes made with Hook3 alone, DDFHFK complexes had a lower run length towards the minus-end of the microtubule, while also having a lower run speed (see Figure 5.25 a-b.). These complexes also had lower run speeds and lengths when travelling towards the plus-end of the microtubule (see Figure 5.25 c-d.). Thus it seems the exact motility of FHF-made complexes may differ to those made with Hook3 alone, but collecting of larger datasets and use of untagged FHF is required to be certain.

In summary, FHF did allow the formation of complexes of dynein and dynactin, although this remained comparatively inefficient even at high concentrations of FHF and required addition of Lis1 to become fully functional. Nevertheless, complex formation was boosted by the presence of KIF1C-stalk and KIF1C-FL by orders of magnitude very similar to that of dynein-dynactin complexes formed with Hook3. The activation of dynein complex formation and landing did not seem to require KIF1C-stalk or KIF1C-FL to remain bound to the complex, and so it appears these molecules might exert their activation effect by affecting dynein's complex assembly efficiency, perhaps priming FHF to be able to bind to dynein and dynactin, or by aid-
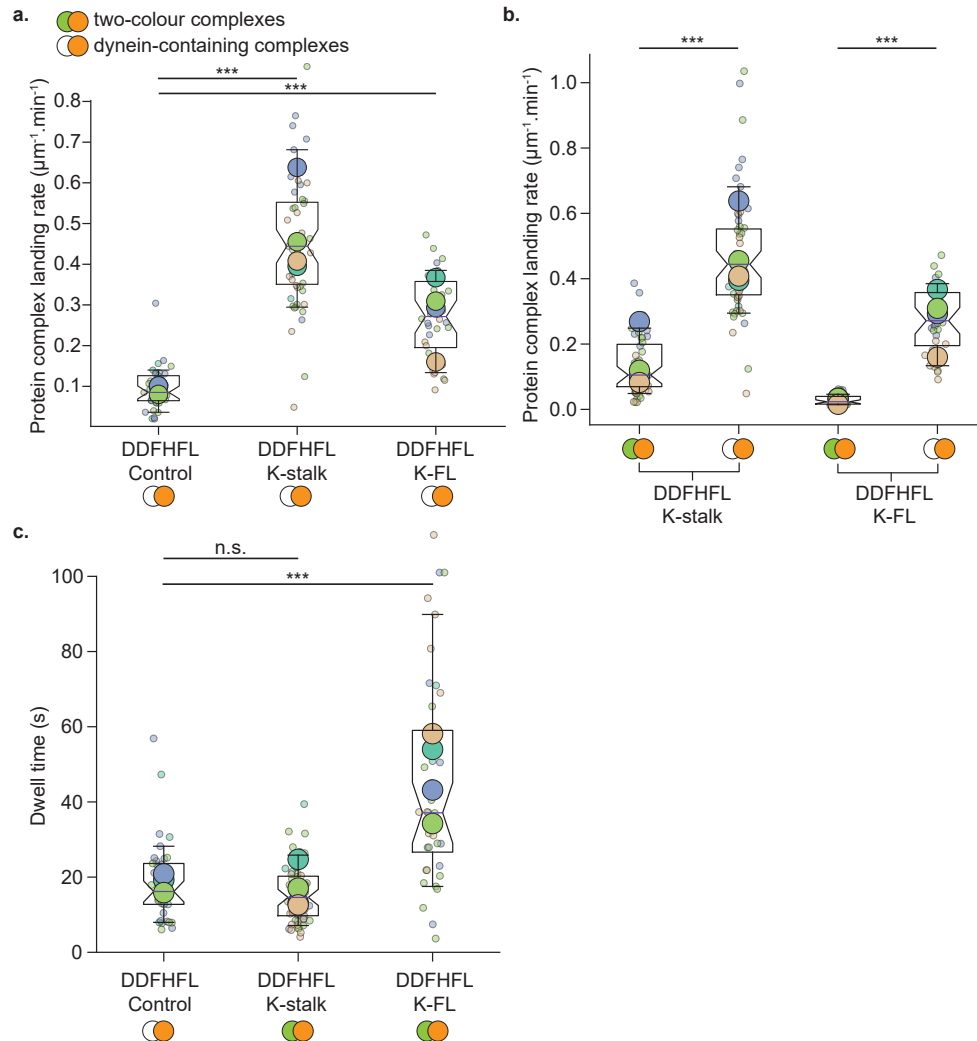
Figure 5.24: Landing rates and dwell times of DDFHF complexes | a. Landing rate measurements of dynein-TMR in the indicated complexes. Note that for this analysis, all dynein molecules are counted, not just those which show a corresponding KIF1C-stalk or KIF1C-GFP signal. **b.** Landing rate of two-colour complexes where KIF1C-stalk or KIF1C-GFP co-migrating signal is also visible, compared to the landing rate where only dynein-TMR signal is considered. **c.** Dwell time of complexes. n.s. indicates p > 0.05, * indicates p $\leq$ 0.05, ** indicates p $\leq$ 0.01 and *** indicates p $\leq$ 0.001.
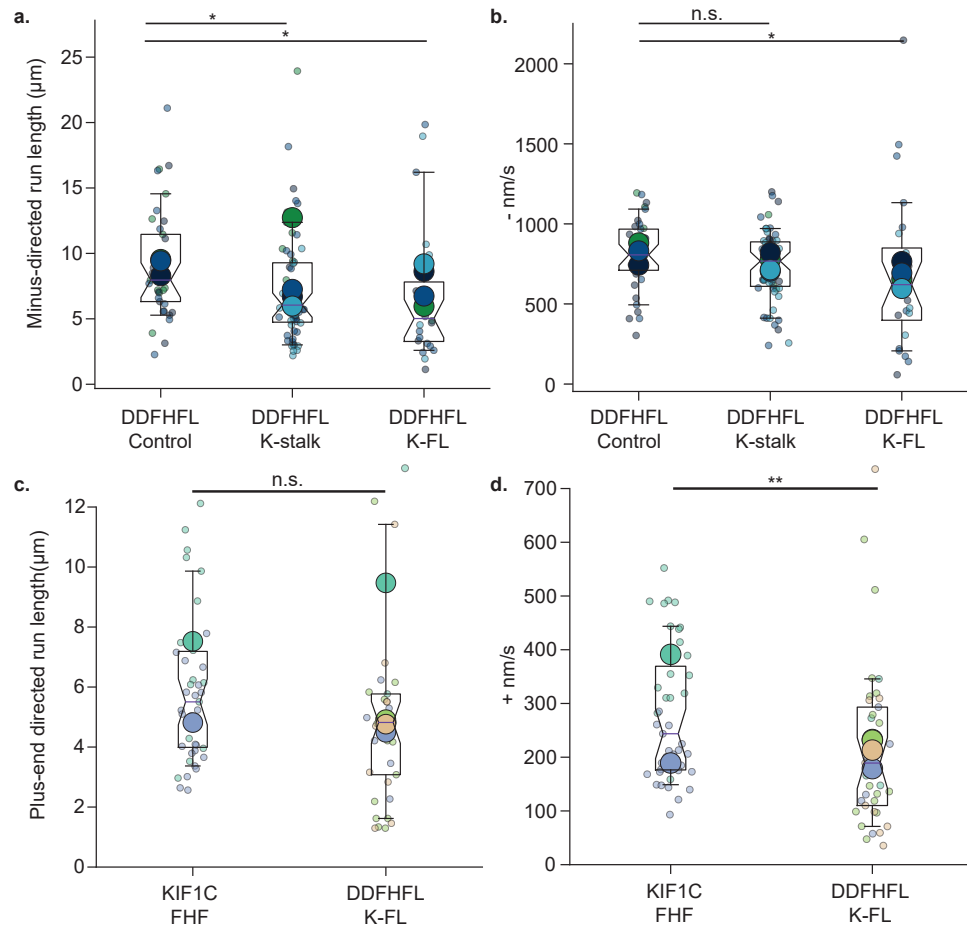
Figure 5.25: Run speeds and lengths of DDFHF complexes | a. Minus-end directed run lengths of the indicated DDFHF complexes. **b.** Minus-end directed run speeds of indicated DDFHF complexes. **c.** Plus-end directed run lengths of DDFHF-KFL complexes compared to KIF1C-FHF. **d.** Plus-end directed run speeds of DDFHF-KFL complexes compared to KIF1C-FHF. In all graphs, the small transparent dots are per-microtubule averages, while the large dots are technical replicate averages. n.s. indicates p > 0.05, * indicates p ≤ 0.05, ** indicates p ≤ 0.01 and *** indicates p ≤ 0.001.

ing the recruitment of a second dynein motor. When KIF1C remained stably bound to DDFHF complexes, it increased the dwell time of the complex, however unlike Hook3 complexes the presence of KIF1C or KIF1C stalk did not increase the overall run lengths of dynein. By far the biggest effect FHF exerted was in determining the directionality of two-colour complexes of dynein and KIF1C. FHF formed 73% plus-end directed complexes, compared to only 16% plus-end complexes formed with Hook3, and thus it appears that FHF likely exerts some selectivity over the directionality of motor complexes. FHF is a promising candidate to explain how overall directionality of these complexes is achieved.

Chapter 6

Discussion

6.1 KIF1C is a autoinhibited dimeric motor activated by the dynein adaptor Hook3

From this study and related work in our lab, we found that KIF1C is an autoinhibited dimer, and its autoinhibition can be relieved when it becomes activated by the dynein adaptor protein Hook3 binding to KIF1C's stalk. Independently, Kendrick et al. confirmed that HEK293-expressed KIF1C is a dimer (Kendrick et al., 2019). Interestingly, this related study found no significant increase in the landing rate of KIF1C in the presence of Hook3. Kinesin activity is known to vary based on temperature and salt concentrations (Kushwaha & Peterman, 2020; Thorn et al., 2000), and the intramolecular contacts made by KIF1C are suggested to be electrostatic and so buffer dependent differences on autoinhibition may be observed (Siddiqui et al., 2019). HEK293 and *Spodoptera frugiperda* (Sf9) cells have subtly different post-translational modifications, and so perhaps KIF1C from human cells is modified differently and this might suggest a post-translationally regulated autoinhibition mechanism which has not been thoroughly investigated yet. In addition, Kendrick et al. produce KIF1C with a C-terminal SNAPf tag that has been reacted with a tetramethylrhodamine (TMR) dye. Perhaps the nature of the TMR dye, containing large bulky hydrophobic groups, is incompatible with KIF1C's autoinhibitory mechanism whereby its stalk is folded to interact with the motor domain, whereas GFP may be better tolerated in this arrangement. Similarly, Kendrick et al. tagged Hook3 on the N-terminus, while here Hook3 was tagged at the C-terminus, and data from peroxisome transport assays show that FRB-Hook3 is not as capable as Hook3-FRB at recruiting motors, in par-

126

ticular dynein, as shown by five-fold decreased movement distances.

The dyes and fluorescent proteins used in single-molecule reconstitution studies can have an effect on the protein's behaviour, and so for non-motor components like Hook3 we were able to perform re-constitutions with unlabelled protein, and indeed in some instances microtubules without fluorescent labels were used. However, as the motor components KIF1C and dynein needed to be seen co-migrating, they could not be unlabelled, and this is a limitation of total internal reflection fluorescence (TIRF) microscopy based reconstitution methods. This being said, new site-specific labelling techniques are becoming more readily available, making it possible to introduce unnatural amino acids into proteins in order to label them (K. J. Lee et al., 2019). This is an attractive technology for TIRF microscopy based reconstitution systems, as it offers the possibility to produce recombinant proteins where the fluorophore has a minimal effect on the structure and function of the protein. However, in order to generate a strategy for site-specific labelling it is helpful to have knowledge of the structure of the protein or subregion that should be tagged. While dynein is rigorously structurally interrogated, KIF1C has yet to be.

In developing this project we had predicted that Bicaudal D-related protein 1 (BICDR1) would be the dynein adaptor which most likely linked KIF1C to dynein, and this was because *in vivo* it had been implicated in Rab6-positive secretory vesicle transport in a KIF1C-dependent manner (Schlager et al., 2010). In our BioID experiments we were unable to find peptides for BICDR1, and consulting published RNA sequencing data confirmed that BICDR1 is not highly expressed in RPE1 cells. Indeed BICDR1 expression is found to be highest in tissues of the kidney, testis, brain and spinal chord, meanwhile KIF1C RNA levels are highest in tissues of the brain and muscle (Schlager et al., 2010; Uhlén et al., 2015). Perhaps the KIF1C-BICDR1 interaction is only significant in those tissues where they're both expressed at high levels, for example, in brain tissues (i.e. neurones) where KIF1C is known to be an important transporter (Schlager et al., 2010). In our hands, overexpression of either Hook3, BICD2 or BICDR1 had strong phenotypes on the peripheral accumulation of Neuropeptide-Y (NPY)-containing vesicles, and this suggested that they could hyperactivate kinesin-driven transport. However when we tested this directly *in vitro*, only Hook3 interacted efficiently with KIF1C while BICDR1 only occasionally co-migrated with KIF1C. The interaction of BICDR1 and KIF1C might be dependent on factors that not available in our reconstitu-

tion experiment, for example they are both shown to bind Rab6a, and perhaps this allows the formation of a ternary complex linked to vesicle transport (P. L. Lee et al., 2015; Schlager et al., 2010). Indeed, activation mechanisms of full-length kinesin-1 have been shown to require breaking of intramolecular interactions, and addition of intermolecular interactions through the binding of cargo adaptors and MAP7 (Chiba et al., 2021; A. E. Twelvetrees et al., 2019). As BICDR1 has been shown to bind to the proline-rich domain of KIF1C at its very C-terminus (Schlager et al., 2010), and not to the stalk of KIF1C like Hook3, then perhaps a separate molecule is required to first release KIF1C's autoinhibition by binding to the stalk region, and only then BICDR1 is able to interact fully with the activated kinesin at its C-terminal proline rich domain, in turn linking it to cargo. Therefore we cannot discount that BICDR1 may bind to KIF1C in a method distinct to Hook3, and this is still an exciting topic for research that may reveal a different mechanism of KIF1C regulation for BICDR1-cargo transport.

KIF1C is likely not alone in binding to dynein adaptors, and perhaps the effects of BICD2 and BICDR1 on intracellular transport could also be because they activate a different kinesin member. Indeed, Redwine et al. showed by extensive BioID protein-protein interaction analysis that the N and C-terminals of the dynein adaptors Bicaudal D homolog 1 (BICD1), Bicaudal D homolog 2 (BICD2), Ninein (NIN), Ninein-like (NINL), Hook1 and Hook3 show enrichment of nearly twenty different kinesins from diverse families (Redwine et al., 2017). Therefore just as dynein adaptors determine the specificity of dynein cargo transport, perhaps they also determine which kinesin might be recruited either to undertake bidirectional transport as a complex, or to alternate use of the adaptor protein. Such kinesin to adaptor interactions warrant further investigation and reconstitution.

6.2 Intracellular Hook3-driven transport is rapid and bidirectional

Inside cells, we found that recruiting Hook3-FRB to peroxisomes resulted in rapid long-range transport which showed occasional bi-directional motion. An equivalent experiment in HeLa cells concluded that Hook3 primarily drove peroxisomes to the centrosome in a unidirectional manner, though in this work the distribution of peroxisomes at fixed points before and after activa-

tion was considered, but not the motion of individual peroxisomes over the course of activation (Olenick et al., 2016). In agreement, we found that the majority of Hook3-FRB driven transport was centrosome directed, though addition of KIF1C rebalanced this and demonstrated the productive engagement of KIF1C with Hook3 (and dynein). We hypothesise that in the mesenchymal cell types used in these experiments, KIF1C might be expressed at lower levels, whereas in professional secretory cells such as neurons where the need for long-range processive transport is much greater, KIF1C is expressed at higher levels, and this is certainly true in transcriptomics data for neuron-rich tissues of the spinal chord (Uhlén et al., 2015).

Whether these peroxisomes recruit single motors or multi-motor assemblies is unknown. At their smallest, peroxisomes are between 100-200 nm in diameter, but range in size up to 1 µm (Grabenbauer et al., 2000). Simulations for kinesin-1 in liposome membranes found that motor occupancy increases with the size of cargoes: given a vesicle that travels 10 µm, the motor occupancy is predicted to be around 35 for an 100 nm cargo, and 800 for a 500 nm cargo (Jiang et al., 2019). However, more motors on the cargo does not directly result in more motors interacting with the microtubule, indeed the model predicts that the number of motors engaged with the microtubule remains between 1-3 even when cargoes contain many hundreds of motors, and conclude it is the binding kinetics of the motors, rather than their number, that dictates processive motility (Jiang et al., 2019). In the context of dynein, which is a much larger molecular assembly than kinesin-1, it is reasonable to hypothesise that for small spherical cargoes only 1-2 motor complexes engage with the microtubule. Peroxisomes do however undergo a process of fission and fusion and so some peroxisomes in our assays were more tubular than spherical. In such an arrangement it is possible that teams of motors would be able to access the microtubule simultaneously. Thus the peroxisome transport we observe is likely a mixture between single-motor and multi-motor driven transport, though electron microscopy of the recruited motors on purified cargoes could confirm this and elaborate the approximate arrangement of the motors.

To gain more physiological insight into Hook3-driven transport in cells, a more natural system could be used. Firstly the cell types used could be changed to more physiologically relevant ones. We began to do this in work that is not presented here, using a human-derived immortalised neuronal precursor cell type called LUHMES which can be differentiated into neurons with neurites in excess of 1 mm in length (Scholz et al., 2011). These cells can-

not be readily transfected and so the use of lentivirus is necessary, and in addition, anecdotally the developers of the cell line had found that larger constructs were less able to be integrated by lentivirus. We were able to integrate the Hook3-FRB/Peroxisome construct into these cells at extremely low efficiency and in the limited number of cells we found, examples of long-range undirectional (and occasionally bidirectional) peroxisome transport could be seen along neurites. Determining the polarity of these neurites (and therefore their microtubules) based on the signal of peroxisomes alone is difficult, and so addition of a marker that gives insight into neurite polarity, such as EB3, is necessary. Thus to understand Hook3-driven transport in a system with defined axon-like microtubule architectures, and where there is a need for extremely long-range transport, studying the neurites of LUHMES cells appears to be an attractive option, but developing stable cell lines in the LUHMES EB3-GFP background to mark microtubule polarity will be required.

Secondly, we had seen from our experiments that overexpression of Hook3 had a strong phenotype on NPY-containing vesicle transport, and this hints to underlying hyperactivation of kinesins, but this could also be explained by a dynein inhibition effect arising from the abundance of dynein adaptor activating transport to the centrosome and in effect sequestering it. Thus in the cells where the Hook3-FRB/Peroxisome assay plasmid has been expressed, there is likely some underlying hyperactivation of motors which may make the system more artificial. Regardless of the cell type, expressing Hook3 at more endogenous levels is important to understanding the natural behaviour of Hook3-driven transport. This would be best achieved using a CRISPR/Cas9-mediated knock-in of the Hook3-FRB/peroxisome plasmid, though the challenges of doing this especially in a neuronal cell type are large. More realistically, depletion of endogenous Hook3 and replacement with Hook3-FRB/peroxisome plasmid under a weak promoter could be a viable option to express Hook3 at amounts closer to the endogenous levels.

The peroxisome targeting system is a powerful way to investigate intracellular transport driven by key molecular players, as it does not require the researcher to know in detail every protein that need be recruited with their protein of interest. The assay has been used to systematically determine which kinesins show axon and dendrite preference (Lipka et al., 2016), has been used to determine how different kinesins oppose dynein driven transport (Ally et al., 2009), and has been used to show how dynein driven peroxisomes pause at microtubule intersections (Kapitein et al., 2010). In our study, by tar-

geting full-length Hook3 to peroxisomes we could be certain that the transport we observed was a direct effect of Hook3 and not because of other motors or adaptors which happen to exist on the cargo, which may be true for other more motile cargoes. While the exact contribution of FAM160A2/Hook/FTS (FHF) complex versus individual Hook3 molecules is not known in cells, our assay allowed us to circumvent this complexity and conclude very simply that Hook3-driven peroxisome transport is bidirectional, and that KIF1C-GFP overexpression has a large effect in altering its transport, providing a tangible system in which to investigate dynein/KIF1C bidirectionality inside cells.

We extended an existing acute motor inhibition method using DmrB's homodimerisation to investigate how inhibition of KIF1C-GFP leads to its re-localisation (Engelke et al., 2016). Consistent with Engelke et al.'s work on KIF1A(1-393), we found that full-length KIF1C was amenable to acute inhi-bition with DmrB. The essential difference in our approaches was the use of a full-length KIF1C motor, which contains the stalk domain which binds to Hook3. In doing so the localisation of KIF1C could be seen over the course of inhibition, and we saw that KIF1C-GFP relocalised from the periphery towards the centrosome.

This approach gave us confidence that KIF1C and dynein were inter-linked on short timescales, and confirmed what longer timescale experiments such as depletion of motors had suggested. But the exact mechanism by which KIF1C is brought back to the centrosome is not clear. Our later find-ings of a reconstituted complex between KIF1C and dynein in the presence of Hook3 could suggest that inside cells KIF1C is holding dynein at the cell's periphery and upon KIF1C inhibition, dynein is able to relocalise KIF1C. An alternative explanation is that the increase in centrosomal KIF1C is caused by inhibited KIF1C not leaving the centrosome, where it is prepared for cargo transport, and so accumulates while inhibited KIF1C in the tail diffuses away over time. However, our assay showed packets of KIF1C which seemed to move from the tail towards the centrosome. A powerful way to discern these two mechanisms would be by inhibiting dynein driven transport, and seeing that KIF1C-GFP is no longer returned to the centrosome. Ciliobrevin D is typ-ically used for dynein inhibition studies (Roossien et al., 2015), though newer more specific dynein inhibitors such as Dynarrestin and Dynapyrozole have recently become commercially available (Höing et al., 2018; Steinman et al., 2017). Similarly, DmrB-inhibitable KIF1C constructs could be made with dele-tion of the region that has been shown to bind to Hook3 (Kendrick et al., 2019;

Siddiqui et al., 2019), and this would allow us to confirm that this KIF1C-retrieval upon inhibition is dependent on Hook3 linking it to dynein. While there is much still to discover, inhibitable full-length KIF1C adds an interesting and powerful tool in understanding bidirectional transport.

6.3 Complexes of KIF1C and dynein reconstitute motor codependence

We found that complexes of KIF1C and dynein could be formed by dynactin with BICDR1, BICD2 and Hook3, although only Hook3 was able to do this efficiently. Dynein-dynactin-Hook3-KIF1C (DDHK) complexes went both towards the plus- and minus- ends of microtubules and occasionally changed direction along their length. Interestingly the strong evidence from cells that had shown BICDR1 was a KIF1C interactor did not appear to be true with purified molecules, where BICDR1 only occasionally migrated with KIF1C and rarely formed co-complexes of KIF1C and dynein (Schlager et al., 2010). As previously discussed, BICDR1 might require other proteins such as Rab6a which was not available in this reconstituted system, and these other proteins could be responsible for allowing efficient complex formation of KIF1C and dynein in the presence of BICDR1.

As we had found an N-terminal FRB on Hook3 appeared to decrease its functionality in peroxisome sorting, we did the majority of our DDHK complex reconstitution with untagged Hook3 in the presence of Lis1. After initial reconstitution of DDHK, and during the time in which we invested in generating gel-filtered Hook3 to overcome aggregation issues, a preprint (and later a paper) were published by Kendrick et al. (2019). Their reported findings were broadly similar in that they found a complex of KIF1C and dynein could form in the presence of Hook3, and they found that this complex had slightly slower run speeds towards the minus- and plus- ends than the individual components. However, a comprehensive and quantitative understanding of DDHK's run-lengths and directional switching behaviour was not presented owing to a relatively small number of complexes observed.

We were able to reconstitute an aspect of motor co-dependence for the first time. The presence of KIF1C increased dynein's landing rate onto microtubules, increased its dwell time on microtubules, and despite decreasing its speed slightly, also increase the minus end directed run length. We

developed a method to map manually segmented motor tracks back to spot intensities, and found that dynein's intensity was greater in complexes where KIF1C or KIF1C's stalk were present, suggesting that KIF1C acts to push the equilibrium of dynein complex formation towards the two-dynein mode. The increase in dwell time of complexes on microtubules and the slightly reduced speed confirmed that KIF1C is not a passive passenger of dynein, but interacts with the microtubule even if the complex moves towards the minus-end. Interestingly, although KIF1C's stalk increased the landing rate of dynein five-fold, only around 50% of the dyneins that landed had a KIF1C-stalk-GFP signal present. This could suggest that only 50% of the KIF1C dimers had active GFP fluorescence, but this is unlikely given it is estimated 80% of GFP molecules are active (Ulbrich & Isacoff, 2007), and the dimeric nature of these KIF1C components means probabilistically 96% of dimers have at least one fluorescently active GFP molecule. Therefore it seemed that KIF1C was not necessarily required to stay with the complex in order to increase the activation of dynein molecules, though the reason for this is unclear. One idea is that KIF1C could direct a change in the conformation of FHF or Hook3 that makes its interaction with dynactin favour one that permits recruitment of the second dynein (see Figure 6.1), and this could be investigated by a structural reconstitution of the DDHK complex.

Unlike dynein, KIF1C-driven transport did not benefit from the presence of the oppositely directed motor in our reconstitution experiment. Presence of dynein caused shorter run lengths and slower run speeds if compared to Hook3-KIF1C alone. However the landing-rate of KIF1C was vastly increased in the presence of either dynein tail, dynactin or full-length dynein. Hook3 alone was able to increase KIF1C's landing rate around two-fold, whereas Hook3 in the presence of dynein, dynactin and Lis1 increased KIF1C's landing rate nearly four-fold, suggesting that it is not only the Hook3 component which activates KIF1C. Perhaps the p150(Glued) domain of dynactin, which has its own microtubule binding activity, enables higher landing rates when in complex with KIF1C. Or perhaps as complexes are turned over in solution, this converts some of the pool of autoinhibited KIF1C molecules to their active form.

Whether the decreased speed of KIF1C transport signifies a true tug-of-war is unclear. Belyy et al. found that linking dynein-dynactin-BICD2 to kinesin-1 through use of DNA origami resulted in a tug-of-war (Belyy et al., 2017). In their experiment, the kinesin was still able to run towards the plus-

133

end of the microtubule but with a 20-fold speed reduction (Belyy et al., 2017). However, we found KIF1C's median velocity only decreased around two-fold, which is a much smaller magnitude of change compared to the tethered kinesin-1/dynein experiment suggesting that this may not be an equivalent tug-of-war state. In order to distinguish the KIF1C directed motion in our assays from the kinesin-1/dynein tug-of-war, the DNA origami experiment described by Belyy et al. could be repeated with KIF1C and Hook3 to see if this arrangement of the motors leads to much lower KIF1C speeds. From our data we know that while KIF1C is transporting dynein towards the plus-end of the microtubule, there is at least some moments tug-of-war occurring. This is interesting as it would suggest that the DDHK complex mainly benefits dynein, while KIF1C derives less benefit except landing on the microtubule more frequently. Perhaps dynein's ability to counteract KIF1C is modulated inside the cell by a factor or post-translational regulation mechanism which isn't included in our reconstitution, so that when KIF1C is in control of the complex's motion, dynein's activity can be reduced.

From our kymographs, and from analysis of time that motor complexes spent pausing, we found that complexes of dynein and KIF1C pause much more often than dynein would ordinarily. One hypothesis is that during minus-end directed transport when dynein comes to the end of it's processive run and would ordinarily detach from the microtubule, the presence of the super-processive KIF1C keeps the complex tethered to the microtubule until dynein can re-engage and continue its run. This may explain how complexes are able to undertake overall longer run lengths than DDH alone. Similarly, the increase in dwell time of the DDHK complex suggests that KIF1C is in contact with the microtubule, and perhaps the motor can enter a low affinity weakly attached state maybe by use of its charged K-loop (Soppina & Verhey, 2014), or by residues in loops 2, 8 and 11 and the alpha-6 site that increase kinesin-3 motor's processivity (Scarabelli et al., 2015). Such a weakly attached state could prevent complexes detaching from the microtubule when dynein finishes a processive run without applying too much opposing force. Swapping the motor domain of KIF1C with that of kinesin-1, replacing the charged K-loop of KIF1C, or mutating amino acids in the aforementioned regions would be an interesting way to understand how force balance and processivity of the kinesin alters the plus-end directed runs of DDHK complexes.

One key aspect of KIF1C and dynein co-complexes which is difficult to probe is the order of complex formation, as well as complex turnover which

134

might occur in solution. Given that the majority of complexes do not undertake directional switching, this could suggest that the directionality of complexes is predetermined during formation rather than on the microtubule itself. Perhaps if dynein interacts with Hook3 first, then KIF1C joins the complex later, this sets the molecules in a conformation that prefers dynein-driven transport, and the reverse would be true if KIF1C interacts with Hook3 first. This idea could be tested by varying the order in which complexes are assembled, by for example pre-mixing Hook3 with KIF1C and then only later adding dynactin and dynein.

We found that very few complexes (around 2%) were able to undertake bidirectional transport. As direction swapping was not described by Kendrick et al., we took steps to ensure that these directional switches were not an artifact of our experimental system by verifying the polarity of each micro-tubule by analysing the motility of an excess of KIF1C-GFP flown in at the end of each experiment, and found that these bidirectional events were gen-uine. Regardless, the observed directional switches were much rarer than we expected based on observations in cells. The number of bidirectional motor complexes we observe could be limited by our measurement technique, as we could not accurately assign motor behaviour at the plus- or minus- end of the microtubule where accumulations of motors were seen. It is possible that a bidirectional complex could reach the end of the microtubule, pause for some time, and then reverse, but due to the presence of other motors at microtubule ends we cannot be certain that the complex we saw reaching the microtubule end is the same one that later leaves it. Thus microtubule ends could be a signal for complexes to reverse, and an analysis of complex motility at much lower concentrations would be necessary to confirm this.

There are a number of other possible factors that could trigger a di-rectional switch in DDHK complexes. Cells contain a hugely more complex microtubule network than an *in vitro* reconstitution system, containing obsta-cles such as other cargoes, microtubules, and cellular components such as organelles. Kinesin-1 mainly remains on one protofilament during transport, and this means its ability to side-step obstacles is limited, while dynein has the ability to switch between protofilaments (Ferro et al., 2019; Wang et al., 1995). It's unknown whether KIF1C acts like kinesin-1 in remaining only on one protofilament during transport, however if it does then being in complex with dynein presents the advantage that upon meeting an obstacle, the motors can reverse and reapproach the obstacle on a different protofilament. Sim-ilarly it is now becoming clearer that microtubules become damaged along
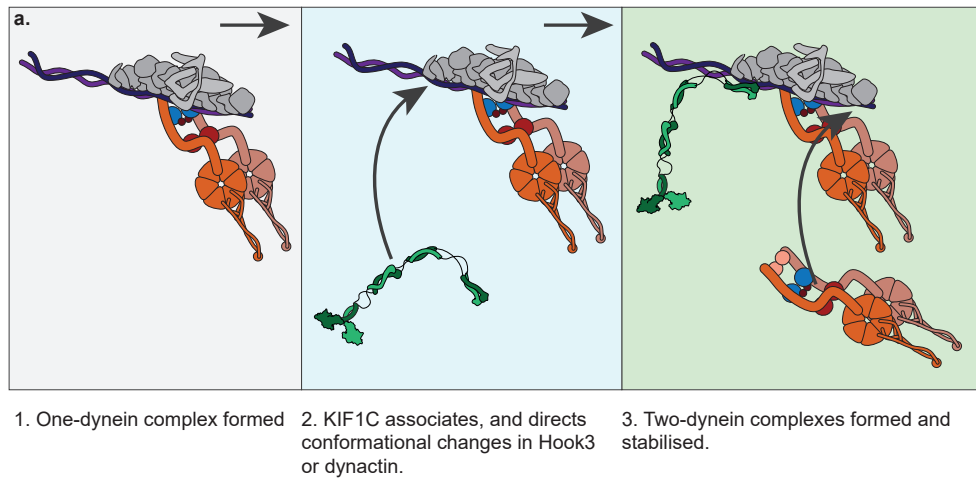
1. One-dynein complex formed
2. KIF1C associates, and directs conformational changes in Hook3 or dynactin.
3. Two-dynein complexes formed and stabilised.

Figure 6.1: KIF1C helps to recruit two-dyneins to DDHK complexes | a. In the presence of KIF1C-stalk or KIF1C, the intensity of dynein-TMR within DDHK increased by 1.2 or 1.5 fold respectively, and this increased the landing rate of dynein. The increase in landing rate was not dependent on whether the complexes still had KIF1C attached when they landed. Thus we hypothesise that KIF1C or KIF1C stalk binding to Hook3/dynactin is sufficient to bring about conformational changes that either aid the recruitment of a second dynein dimer, or stabilise it during attachment.

their lattices through their lifetime, and are repaired by incorporation of new tubulin along the lattice (Aher et al., 2020; Aumeier et al., 2016; Triclin et al., 2021). Unrepaired sites, or regions where repair machinery is assembled, may present another obstacle that requires a bidirectional complex to reverse away from the point of damage and then either switch to a different protofilament, or change microtubule entirely. Finally, the differential sensitivity of dynein and kinesin to microtubule associated proteins (MAPs) and post-translational modifications on the microtubule path may cause motors to be unable to walk processively along some regions of microtubules (Monroy et al., 2018; Monroy et al., 2020; Sirajuddin et al., 2014), but the co-complexes of KIF1C and dynein may be more able to navigate this.

Finally, we did preliminary work in reconstituting a complex of dynein and KIF1C using Hook3 within FHF complex. We found that complex formation with this reagent was quite inefficient, however this could be improved with Lis1, and this could be in part because Hook3 within this complex is labelled with an N-terminal SNAPf tag. However, FHF very efficiently formed complexes with KIF1C alone, and dynein-dynactin-FHF-KIF1C (DDFHFK) complexes often travelled towards the plus-end of the microtubule, so this could

hint at a possible preference of FHF for KIF1C motility instead of dynein. Inside the cell, FHF could offer a way to regulate the availability of Hook3 for motors. While the interaction of p107FHIP/FAM160A2 has not yet been mapped in detail, the interaction of Fused Toes (FTS) with Hook3 has been mapped by yeast two-hybrid to the C-terminal region of Hook3 between amino acids 542-718, and this is also where KIF1C's interaction has been mapped to (Kendrick et al., 2019; Siddiqui et al., 2019; Xu et al., 2008). FTS could be a regulator of KIF1C's interaction with Hook3 and so too with the DDFHF complex. Perhaps FTS or a yet unidentified factor is able to selectively reveal or obscure the binding site of KIF1C on Hook3, or once bound, perhaps this factor directs some conformational changes in the Hook3/dynactin that make it favour either a plus- or minus- end directed motility. Such a regulator would be able to control the balance of intracellular transport undertaken by Hook3 cargoes and may avoid dynein opposing KIF1C transport. The full complexity of this system will not be understood until the interactions of p107FHIP/FAM160A2 and FTS with Hook3 have been mapped, and any regulatory mechanism has been revealed.

With this in mind, we arrive at a hypothetical model for the behaviour of KIF1C and dynein co-complexes. When the complex is formed with Hook3 alone, KIF1C is able to promote the formation of two-dynein complexes and this could be by arranging one-dynein complexes in a way that they can most optimally accept a second dynein (see Figure 6.1). If KIF1C remains in the complex it is able to promote landing of the complexes on to the microtubule and increases the time that the complexes remain on the microtubule. Towards the minus-end of the microtubule, KIF1C acts as a processivity factor, by forming a weak attachment to the microtubule that rescues detachment events of dynein. The presence of KIF1C makes dynein more processive, allowing it to undertake even longer runs towards the minus-ends of microtubules. When the DDHK complex travels towards the plus-end of the microtubule, dynein remains active and appears to supply some opposing force against KIF1C, but this does not prevent processive plus-end directed transport. Regulation by an additional factor, or by post-translational modification, may be required to inhibit dynein transport while KIF1C is running. Complexes formed with FHF display a different proportion of plus- and minus- end directed transport, and this suggests that FHF may have a degree of control over the complex's directionality, though a mechanism for this is not yet known. Bidirectional events may be responses to obstacles such as MAPs,

other cargoes, defects, crossovers or microtubule ends, although this still re-
mains to be investigated. This model has been summarised in Figure 6.2.

We predict that KIF1C, Hook3 and dynein form just one of many bidi-
rectional complexes in the cell, and linking the activities of kinesin and dynein
could be a common solution to avoiding an outright tug-of-war of motors and
allow the coordinated switching of directionality in response to obstacles and
other signals.

a. Plus-end directed DDHK transport

Plus-end

Minus-end

Dyneins supply ocassional minus-end directed force
that reduces the velocity of KIF1C, but overall direction can be maintained.

b. Minus-end directed DDHK transport

Plus-end

Minus-end

KIF1C applies very little opposing motility,
but acts to increase microtubule affinity and therefore
the landing rate and run length of dynein.

c. Bidirectional DDHK motility

1. Oncoming traffic?

2. Lattice damage?

3. MAP occupancy?

Plus-end

Minus-end

Local microtubule factors such as MAPs, damage to the lattice,
oncoming traffic, or cellular obstacles cause complexes
to reverse and reapproach.

Figure 6.2: Dynein benefits from the presence of KIF1C, but not vice versa | a. Plus-end directed DDHK complexes are slower and run less far than KIF1C alone, and so we conclude that dynein does apply some opposing force during plus-end directed transport, however **b.** towards the minus-end, dynein is able to undertake longer runs in the presence of KIF1C, and KIF1C also increases the time complexes spend on the microtubule. This suggests KIF1C is able to act as a processivity factor, perhaps offering a low affinity tether to the microtubule. **c.** Directional switching of complexes is rare, and we predict that various obstacles along the microtubule could be responsible for inducing direction changes.

139

Bibliography

Aher, A., Rai, D., Schaedel, L., Gaillard, J., John, K., Liu, Q., Altelaar, M., Blanchoin, L., Thery, M., & Akhmanova, A. (2020). CLASP Mediates Microtubule Repair by Restricting Lattice Damage and Regulating Tubulin Incorporation. *Current Biology*, *30*(11), 2175–2183. https://doi.org/10.1016/j.cub.2020.03.070

Ally, S., Larson, A. G., Barlan, K., Rice, S. E., & Gelfand, V. I. (2009). Opposite-polarity motors activate one another to trigger cargo transport in live cells. *Journal of Cell Biology*, *187*(7), 1071–1082. https://doi.org/10.1083/jcb.200908075

Alushin, G. M., Lander, G. C., Kellogg, E. H., Zhang, R., Baker, D., & Nogales, E. (2014). High-Resolution microtubule structures reveal the structural transitions in $\alpha\beta$-tubulin upon GTP hydrolysis. *Cell*, *157*(5), 1117–1129. https://doi.org/10.1016/j.cell.2014.03.053

Atkins, M., Gasmi, L., Bercier, V., Revenu, C., Del Bene, F., Hazan, J., & Fassier, C. (2019). FIGNL1 associates with KIF1Bβ and BICD1 to restrict dynein transport velocity during axon navigation. *Journal of Cell Biology*, *218*(10), 3290–3306. https://doi.org/10.1083/JCB.201805128

Auckland, P., & McAinsh, A. D. (2015). Building an integrated model of chromosome congression. *Journal of Cell Science*, *128*(18), 3363–3374. https://doi.org/10.1242/jcs.169367

Aumeier, C., Schaedel, L., Gaillard, J., John, K., Blanchoin, L., & Théry, M. (2016). Self-repair promotes microtubule rescue. *Nature Cell Biology*, *18*(10), 1054–1064. https://doi.org/10.1038/ncb3406

Bálint, Š., Verdeny Vilanova, I., Sandoval Álvarez, Á., & Lakadamyali, M. (2013). Correlative live-cell and superresolution microscopy reveals cargo transport dynamics at microtubule intersections. *Proceedings*

of the National Academy of Sciences of the United States of America, *110*(9), 3375–80. https://doi.org/10.1073/pnas.1219206110

Barkus, R. V., Klyachko, O., Horiuchi, D., Dickson, B. J., & Saxton, W. M. (2008). Identification of an axonal kinesin-3 motor for fast anterograde vesicle transport that facilitates retrograde transport of neuropeptides. *Molecular Biology of the Cell*, *19*(1), 274–283. https://doi.org/10.1091/mbc.E07-03-0261

Baumann, S., Komissarov, A., Gili, M., Ruprecht, V., Wieser, S., & Maurer, S. P. (2020). A reconstituted mammalian APC-kinesin complex selectively transports defined packages of axonal mRNAs. *Science Advances*, *6*(11), eaaz1588. https://doi.org/10.1126/sciadv.aaz1588

Baumbach, J., Murthy, A., McClintock, M. A., Dix, C. I., Zalyte, R., Hoang, H. T., & Bullock, S. L. (2017). Lissencephaly-1 is a context-dependent regulator of the human dynein complex. *eLife*. https://doi.org/10.7554/eLife.21768

Belyy, V., Schlager, M. A., Foster, H., Reimer, A. E., Carter, A. P., Yildiz, A., & Avenue, F. C. (2017). The mammalian dynein/dynactin complex is a strong opponent to kinesin in a tug-of-war competition. *18*(9), 1018–1024. https://doi.org/10.1038/ncb3393.The

Black, M. M., Slaughter, T., Moshiach, S., Obrocka, M., & Fischer, I. (1996). Tau is enriched on dynamic microtubules in the distal region of growing axons. *Journal of Neuroscience*, *16*(11), 3601–3619. https://doi.org/10.1523/jneurosci.16-11-03601.1996

Blasius, T. L., Reed, N., Slepchenko, B. M., & Verhey, K. J. (2013). Recycling of Kinesin-1 Motors by Diffusion after Transport. *PLoS ONE*, *8*(9), 45–49. https://doi.org/10.1371/journal.pone.0076081

Breuzard, G., Hubert, P., Nouar, R., De Bessa, T., Devred, F., Barbier, P., Sturgis, J. N., & Peyrot, V. (2013). Molecular mechanisms of Tau binding to microtubules and its role in microtubule dynamics in live cells. *Journal of Cell Science*, *126*(13), 2810–2819. https://doi.org/10.1242/jcs.120832

Britto, M., Goulet, A., Rizvi, S., von Loeffelholz, O., Moores, C. A., & Cross, R. A. (2016). Schizosaccharomyces pombe kinesin-5 switches direction using a steric blocking mechanism. *Proceedings of the National Academy of Sciences of the United States of America*, *113*(47), E7483–E7489. https://doi.org/10.1073/pnas.1611581113

141

Budaitis, B. G., Jariwala, S., Rao, L., Yue, Y., Sept, D., Verhey, K. J., & Gennerich, A. (2021). Pathogenic mutations in the kinesin-3 motor KIF1A diminish force generation and movement through allosteric mechanisms. *The Journal of cell biology*, *220*(4). https://doi.org/10.1083/jcb.202004227

Budaitis, B. G., Jariwala, S., Reinemann, D. N., Schimert, K. I., Scarabelli, G., Grant, B. J., Sept, D., Lang, M. J., & Verhey, K. J. (2019). Neck linker docking is critical for kinesin-1 force generation in cells but at a cost to motor speed and processivity. *eLife*, *8*. https://doi.org/10.7554/eLife.44146

Bulinski, J. C., & Borisy, G. G. (1980). Microtubule-associated proteins from cultured HeLa cells. *Journal of Biological Chemistry*, *255*(23), 11570–11576. https://doi.org/10.1016/s0021-9258(19)70328-7

Bullock, S. L., & Ish-Horowicz, D. (2001). Conserved signals and machinery for RNA transport in Drosophila oogenesis and embryogenesis. *Nature*, *414*(6864), 611–616. https://doi.org/10.1038/414611a

Carter, N. J., & Cross, R. A. (2005). Mechanics of the kinesin step. *Nature*, *435*(7040), 308–12. https://doi.org/10.1038/nature03528

Chakraborty, M., Toleikis, A., Siddiqui, N., Cross, R. A., & Straube, A. (2020). Activation of cytoplasmic dynein through microtubule crossbridging. https://doi.org/10.1101/2020.04.13.038950

Chase, K., Doval, F., & Vershinin, M. (2017). Enhanced stability of kinesin-1 as a function of temperature. *Biochemical and Biophysical Research Communications*, *493*(3), 1318–1321. https://doi.org/10.1016/j.bbrc.2017.09.172

Chiba, K., Ori-Mckenney, K. M., Niwa, S., & Mckenney, R. J. (2021). Reconstitution of Kinesin-1 Activation. *bioRxiv*, 2021.03.12.434960. https://doi.org/10.1101/2021.03.12.434960

Chiba, K., Takahashi, H., Chen, M., Obinata, H., Arai, S., Hashimoto, K., Oda, T., McKenney, R. J., & Niwa, S. (2019). Disease-associated mutations hyperactivate KIF1A motility and anterograde axonal transport of synaptic vesicle precursors. *Proceedings of the National Academy of Sciences of the United States of America*, *116*(37), 18429–18434. https://doi.org/10.1073/pnas.1905690116

Chowdhury, S., Ketcham, S. A., Schroer, T. A., & Lander, G. C. (2015). Structural organization of the dynein-dynactin complex bound to mi-

crotubules. *Nature Structural and Molecular Biology*, *22*(4), 345–347. https://doi.org/10.1038/nsmb.2996

Conway, L., & Ross, J. L. (2014). Kinesin Motor Transport is Altered by Macromolecular Crowding and Transiently Associated Microtubule-Associated Proteins. *ArXiv e-prints*, 1–3.

Crevel, I. M., Nyitrai, M., Alonso, M. C., Weiss, S., Geeves, M. Á., & Cross, R. A. (2004). What kinesin does at roadblocks: The coordination mechanism for molecular walking. *EMBO Journal*, *23*(1), 23–32. https://doi.org/10.1038/sj.emboj.7600042

del Castillo, U., Winding, M., Lu, W., & Gelfand, V. I. (2015). Interplay between kinesin-1 and cortical dynein during axonal outgrowth and microtubule organization in Drosophila neurons. *eLife*, *4*(NOVEMBER2015). https://doi.org/10.7554/eLife.10140

Derr, N. D., Goodman, B. S., Jungmann, R., Leschziner, A. E., Shih, W. M., & Reck-Peterson, S. L. (2012). Tug-of-war in motor protein ensembles revealed with a programmable DNA origami scaffold. *Science*, *338*(6107), 662–665. https://doi.org/10.1126/science.1226734

DeSantis, M. E., Cianfrocco, M. A., Htet, Z. M., Tran, P. T., Reck-Peterson, S. L., & Leschziner, A. E. (2017). Lis1 Has Two Opposing Modes of Regulating Cytoplasmic Dynein. *Cell*, *170*(6), 1197–1208. https://doi.org/10.1016/j.cell.2017.08.037

Dor, T., Cinnamon, Y., Raymond, L., Shaag, A., Bouslam, N., Bouhouche, A., Gaussen, M., Meyer, V., Durr, A., Brice, A., Benomar, A., Stevanin, G., Schuelke, M., & Edvardson, S. (2014). KIF1C mutations in two families with hereditary spastic paraparesis and cerebellar dysfunction. *Journal of medical genetics*, *51*(2), 137–42. https://doi.org/10.1136/jmedgenet-2013-102012

Dorner, C., Ciossek, T., Müller, S., Møller, N. P. H., Ullrich, A., & Lammers, R. (1998). Characterization of KIF1C, a new kinesin-like protein involved in vesicle transport from the Golgi apparatus to the endoplasmic reticulum. *Journal of Biological Chemistry*, *273*(32), 20267–20275. https://doi.org/10.1074/jbc.273.32.20267

Dorner, C., Ullrich, A., Häring, H. U., & Lammers, R. (1999). The kinesin-like motor protein KIF1C occurs in intact cells as a dimer and associates with proteins of the 14-3-3 family. *Journal of Biological Chemistry*, *274*(47), 33654–33660. https://doi.org/10.1074/jbc.274.47.33654

Drerup, C. M., Lusk, S., & Nechiporuk, A. (2016). Kif1B interacts with KBP to promote axon elongation by localizing a microtubule regulator to growth cones. *Journal of Neuroscience*, *36*(26), 7014–7026. https://doi.org/10.1523/JNEUROSCI.0054-16.2016

Duellberg, C., Trokter, M., Jha, R., Sen, I., Steinmetz, M. O., & Surrey, T. (2014). Reconstitution of a hierarchical +TIP interaction network controlling microtubule end tracking of dynein. *Nature Cell Biology*, *16*(8), 804–811. https://doi.org/10.1038/ncb2999

Efimova, N., Grimaldi, A., Bachmann, A., Frye, K., Zhu, X., Feoktistov, A., Straube, A., & Kaverina, I. (2014). Podosome-regulating kinesin KIF1C translocates to the cell periphery in a CLASP-dependent manner. *Journal of Cell Science*, *127*(24), 5179–5188. https://doi.org/10.1242/jcs.149633

Engelke, M. F., Winding, M., Yue, Y., Shastry, S., Teloni, F., Reddy, S., Blasius, T. L., Soppina, P., Hancock, W. O., Gelfand, V. I., & Verhey, K. J. (2016). Engineered kinesin motor proteins amenable to small-molecule inhibition. *Nature Communications*, *7*, 1–12. https://doi.org/10.1038/ncomms11159

Fehling, S. K., Noda, T., Maisner, A., Lamp, B., Conzelmann, K. K., Kawaoka, Y., Klenk, H. D., Garten, W., & Strecker, T. (2013). The microtubule motor protein KIF13A is involved in intracellular trafficking of the Lassa virus matrix protein Z. *Cellular Microbiology*, *15*(2), 315–334. https://doi.org/10.1111/cmi.12095

Feng, Q., Gicking, A. M., & Hancock, W. O. (2020). Dynactin p150 promotes processive motility of DDB complexes by minimizing diffusional behavior of dynein (E. Holzbaur, Ed.). *Molecular Biology of the Cell*, *31*(8), 782–792. https://doi.org/10.1091/mbc.E19-09-0495

Ferenz, N. P., Gable, A., & Wadsworth, P. (2011). Mitotic Functions of Kinesin-5. *Cell*, *21*(3), 255–259. https://doi.org/10.1016/j.semcdb.2010.01.019.Mitotic

Ferro, L. S., Can, S., Turner, M. A., Elshenawy, M. M., & Yildiz, A. (2019). Kinesin and dynein use distinct mechanisms to bypass obstacles. *eLife*, *8*. https://doi.org/10.7554/eLife.48629

Forth, S., & Kapoor, T. M. (2017). The mechanics of microtubule networks in cell division. *Journal of Cell Biology*, *216*(6), 1525–1531. https://doi.org/10.1083/jcb.201612064

Fridolfsson, H. N., Ly, N., Meyerzon, M., & Starr, D. A. (2010). UNC-83 coordinates kinesin-1 and dynein activities at the nuclear envelope during nuclear migration. *Developmental Biology*, *338*(2), 237–250. https://doi.org/10.1016/j.ydbio.2009.12.004

Friel, C., & Howard, J. (2011). The kinesin-13 MCAK has an unconventional ATPase cycle adapted for microtubule depolymerization. *The EMBO Journal*, *30*(19), 3928–3939. https://doi.org/10.1038/emboj.2011.290

Fuchs, F., & Westermann, B. (2005). Role of Unc104/KIF1-related motor proteins in mitochondrial transport in Neurospora crassa. *Molecular Biology of the Cell*, *16*(1), 153–161. https://doi.org/10.1091/mbc.E04-05-0413

Gabrych, D. R., Lau, V. Z., Niwa, S., & Silverman, M. A. (2019). Going Too Far Is the Same as Falling Short†: Kinesin-3 Family Members in Hereditary Spastic Paraplegia. https://doi.org/10.3389/fncel.2019.00419

Grabenbauer, M., Sätzler, K., Baumgart, E., & Fahimi, H. D. (2000). Three-Dimensional Ultrastractural Analysis of Peroxisomes in HepG2 Cells: Absence of Peroxisomal Reticulum but Evidence of Close Spatial Association with the Endoplasmic Reticulum. *Cell Biochemistry and Biophysics*, *32*(1), 37–49. https://doi.org/10.1385/cbb:32:1-3:37

Grotjahn, D. A., Chowdhury, S., Xu, Y., McKenney, R. J., Schroer, T. A., & Lander, G. C. (2018). Cryo-electron tomography reveals that dynactin recruits a team of dyneins for processive motility. *Nature Structural and Molecular Biology*, *25*(3), 203–207. https://doi.org/10.1038/s41594-018-0027-7

Guo, J., Walss-Bass, C., & Ludueña, R. F. (2010). The β isotypes of tubulin in neuronal differentiation. *Cytoskeleton*, *67*(7), 431–441. https://doi.org/10.1002/cm.20455

Guo, X., Farías, G. G., Mattera, R., & Bonifacino, J. S. (2016). Rab5 and its effector FHF contribute to neuronal polarity through dynein-dependent retrieval of somatodendritic proteins from the axon. *Proceedings of the National Academy of Sciences of the United States of America*, *113*(36), E5318–E5327. https://doi.org/10.1073/pnas.1601844113

Gutierrez, P. A., Ackermann, B. E., Vershinin, M., & McKenney, R. J. (2017). Differential effects of the dynein-regulatory factor Lissencephaly-1 on processive dynein-dynactin motility. *Journal of Biological Chemistry*, *292*(29), 12245–12255. https://doi.org/10.1074/jbc.M117.790048

Hammond, J. W., Cai, D., Blasius, T. L., Li, Z., Jiang, Y., Jih, G. T., Meyhofer, E., & Verhey, K. J. (2009). Mammalian Kinesin-3 Motors Are Dimeric In Vivo and Move by Processive Motility upon Release of Autoinhibition (M. Schliwa, Ed.). *PLoS Biology*, *7*(3), e1000072. https://doi.org/10.1371/journal.pbio.1000072

Hancock, W. O. (2014). Bidirectional cargo transport: moving beyond tug of war. *Nature Reviews Molecular Cell Biology*, *15*(9), 615–628. https://doi.org/10.1038/nrm3853

Hancock, W. O. (2016). The Kinesin-1 Chemomechanical Cycle: Stepping Toward a Consensus. https://doi.org/10.1016/j.bpj.2016.02.025

Hendricks, A. G., Perlson, E., Ross, J. L., Schroeder, H. W., Tokito, M., & Holzbaur, E. L. F. (2010). Motor Coordination via a Tug-of-War Mechanism Drives Bidirectional Vesicle Transport. *Current Biology*, *20*(8), 697–702. https://doi.org/10.1016/j.cub.2010.02.058

Henrichs, V., Grycova, L., Barinka, C., Nahacka, Z., Neuzil, J., Diez, S., Rohlena, J., Braun, M., & Lansky, Z. (2020). Mitochondria-adaptor TRAK1 promotes kinesin-1 driven transport in crowded environments. *Nature Communications*, *11*(1), 1–13. https://doi.org/10.1038/s41467-020-16972-5

Hernández-Vega, A., Braun, M., Scharrel, L., Jahnel, M., Wegmann, S., Hyman, B. T., Alberti, S., Diez, S., & Hyman, A. A. (2017). Local Nucleation of Microtubule Bundles through Tubulin Concentration into a Condensed Tau Phase. *Cell Reports*, *20*(10), 2304–2312. https://doi.org/10.1016/j.celrep.2017.08.042

Herrmann, L., Wiegmann, C., Arsalan-Werner, A., Hilbrich, I., Jäger, C., Flach, K., Suttkus, A., Lachmann, I., Arendt, T., & Holzer, M. (2015). Hook proteins: Association with alzheimer pathology and regulatory role of Hook3 in amyloid beta generation. *PLoS ONE*, *10*(3), 1–23. https://doi.org/10.1371/journal.pone.0119423

Höing, S., Yeh, T. Y., Baumann, M., Martinez, N. E., Habenberger, P., Kremer, L., Drexler, H. C., Küchler, P., Reinhardt, P., Choidas, A., Zischinsky, M. L., Zischinsky, G., Nandini, S., Ledray, A. P., Ketcham, S. A., Reinhardt, L., Abo-Rady, M., Glatza, M., King, S. J., … Sterneckert, J. (2018). Dynarrestin, a Novel Inhibitor of Cytoplasmic Dynein. *Cell Chemical Biology*, *25*(4), 357–369. https://doi.org/10.1016/j.chembiol.2017.12.014

Hoogenraad, C. C., Akhmanova, A., Howell, S. A., Dortland, B. R., De Zeeuw, C. I., Willemsen, R., Visser, P., Grosveld, F., & Galjart, N. (2001). Mammalian golgi-associated Bicaudal-D2 functions in the dynein-dynactin pathway by interacting with these complexes. *EMBO Journal*, *20*(15), 4041–4054. https://doi.org/10.1093/emboj/20.15.4041

Hooikaas, P. J., Martin, M., Mühlethaler, T., Kuijntjes, G. J., Peeters, C. A., Katrukha, E. A., Ferrari, L., Stucchi, R., Verhagen, D. G., Van Riel, W. E., Grigoriev, I., Altelaar, A. F., Hoogenraad, C. C., Rüdiger, S. G., Steinmetz, M. O., Kapitein, L. C., & Akhmanova, A. (2019). MAP7 family proteins regulate kinesin-1 recruitment and activation. *Journal of Cell Biology*, *218*(4), 1298–1318. https://doi.org/10.1083/jcb.201808065

Horiguchi, K., Hanada, T., Fukui, Y., & Chishti, A. H. (2006). Transport of PIP3 by GAKIN, a kinesin-3 family protein, regulates neuronal cell polarity. *Journal of Cell Biology*, *174*(3), 425–436. https://doi.org/10.1083/jcb.200604031

Howell, B. J., McEwen, B. F., Canman, J. C., Hoffman, D. B., Farrar, E. M., Rieder, C. L., & Salmon, E. D. (2001). Cytoplasmic dynein/dynactin drives kinetochore protein transport to the spindle poles and has a role in mitotic spindle checkpoint inactivation. *Journal of Cell Biology*, *155*(7), 1159–1172. https://doi.org/10.1083/jcb.200105093

Htet, Z. M., Gillies, J. P., Baker, R. W., Leschziner, A. E., DeSantis, M. E., & Reck-Peterson, S. L. (2020). LIS1 promotes the formation of activated cytoplasmic dynein-1 complexes. *Nature Cell Biology*, *22*(5), 518–525. https://doi.org/10.1038/s41556-020-0506-z

Huang, J., Roberts, A. J., Leschziner, A. E., & Reck-Peterson, S. L. (2012). Lis1 acts as a "clutch" between the ATPase and microtubule-binding domains of the dynein motor. *Cell*, *150*(5), 975–986. https://doi.org/10.1016/j.cell.2012.07.022

Hung, C. O., & Coleman, M. P. (2016). KIF1A mediates axonal transport of BACE1 and identification of independently moving cargoes in living SCG neurons. *Traffic*, *17*(11), 1155–1167. https://doi.org/10.1111/tra.12428

Hunter, J. D. (2007). Matplotlib: A 2D graphics environment. *Computing in Science and Engineering*, *9*(3), 99–104. https://doi.org/10.1109/MCSE.2007.55

Hyman, A. A., Salser, S., Drechsel, D. N., Unwin, N., & Mitchison, T. J. (1992). Role of GTP hydrolysis in microtubule dynamics: information from a

slowly hydrolyzable analogue, GMPCPP. *Molecular biology of the cell*, *3*(10), 1155–67. https://doi.org/10.1091/mbc.E12-03-0186

Janke, C., & Magiera, M. M. (2020). The tubulin code and its role in controlling microtubule properties and functions. https://doi.org/10.1038/s41580-020-0214-3

Jeanneret, R., Pushkin, D. O., Kantsler, V., & Polin, M. (2016). Entrainment dominates the interaction of microalgae with micron-sized objects. *Nature Communications*, *7*(1), 1–7. https://doi.org/10.1038/ncomms12518

Jenal, M., Elkon, R., Loayza-Puch, F., van Haaften, G., Kühn, U., Menzies, F. M., Vrielink, J. A. O., Bos, A. J., Drost, J., Rooijers, K., Rubinsztein, D. C., & Agami, R. (2012). The Poly(A)-Binding Protein Nuclear 1 Suppresses Alternative Cleavage and Polyadenylation Sites. *Cell*, *149*(3), 538–553. https://doi.org/10.1016/j.cell.2012.03.022

Jiang, R., Vandal, S., Park, S., Majd, S., Tüzel, E., & Hancock, W. O. (2019). Microtubule binding kinetics of membrane-bound kinesin-1 predicts high motor copy numbers on intracellular cargo. *Proceedings of the National Academy of Sciences of the United States of America*, *116*(52), 26564–26570. https://doi.org/10.1073/pnas.1916204116

Kapitein, L. C., Schlager, M. A., Van Der Zwan, W. A., Wulf, P. S., Keijzer, N., & Hoogenraad, C. C. (2010). Probing intracellular motor protein activity using an inducible cargo trafficking assay. *Biophysical Journal*, *99*(7), 2143–2152. https://doi.org/10.1016/j.bpj.2010.07.055

Kardon, J. R., Reck-Peterson, S. L., & Vale, R. D. (2009). Regulation of the processivity and intracellular localization of Saccharomyces cerevisiae dynein by dynactin. *Proceedings of the National Academy of Sciences of the United States of America*, *106*(14), 5669–5674. https://doi.org/10.1073/pnas.0900976106

Kendrick, A. A., Dickey, A. M., Redwine, W. B., Tran, P. T., Vaites, L. P., Dzieciatkowska, M., Harper, J. W., & Reck-Peterson, S. L. (2019). Hook3 is a scaffold for the opposite-polarity microtubule-based motors cytoplasmic dynein-1 and KIF1C. *Journal of Cell Biology*. https://doi.org/10.1083/JCB.201812170

Kim, D. I., Jensen, S. C., Noble, K. A., Kc, B., Roux, K. H., Motamedchaboki, K., & Roux, K. J. (2016). An improved smaller biotin ligase for BioID proximity labeling. *Molecular Biology of the Cell*, *27*(8), 1188–1196. https://doi.org/10.1091/mbc.E15-12-0844

King, S. J., & Schroer, T. a. (2000). Dynactin increases the processivity of the cytoplasmic dynein motor. *Nature cell biology*, *2*(1), 20–24. https://doi.org/10.1038/71338

Klopfenstein, D. R., & Vale, R. D. (2004). The lipid binding pleckstrin homology domain in UNC-104 kinesin is necessary for synaptic vesicle transport in Caenorhabditis elegans. *Molecular Biology of the Cell*, *15*(8), 3729–3739. https://doi.org/10.1091/mbc.E04-04-0326

Kopp, P., Lammers, R., Aepfelbacher, M., Woehlke, G., Rudel, T., Machuy, N., Steffen, W., & Linder, S. (2006). The kinesin KIF1C and microtubule plus ends regulate podosome dynamics in macrophages. *Molecular Biology of the Cell*, *17*(6), 2811–2823. https://doi.org/10.1091/mbc.E05-11-1010

Kushwaha, V. S., & Peterman, E. J. (2020). The temperature dependence of kinesin motor-protein mechanochemistry. *Biochemical and Biophysical Research Communications*, *529*(3), 812–818. https://doi.org/10.1016/j.bbrc.2020.06.004

Lam, C., Vergnolle, M. A., Thorpe, L., Woodman, P. G., & Allan, V. J. (2010). Functional interplay between LIS1, NDE1 and NDEL1 in dynein-dependent organelle positioning. *Journal of Cell Science*, *123*(2), 202–212. https://doi.org/10.1242/jcs.059337

Lee, K. J., Kang, D., & Park, H. S. (2019). Site-Specific Labeling of Proteins Using Unnatural Amino Acids. https://doi.org/10.14348/molcells.2019.0078

Lee, P. L., Ohlson, M. B., & Pfeffer, S. R. (2015). The Rab6-regulated KIF1C kinesin motor domain contributes to Golgi organization. *eLife*, *2015*(4), 1–24. https://doi.org/10.7554/eLife.06029

Lipka, J., Kapitein, L. C., Jaworski, J., & Hoogenraad, C. C. (2016). Microtubule-binding protein doublecortin-like kinase 1 (DCLK1) guides kinesin-3-mediated cargo transport to dendrites. *The EMBO Journal*, *35*(3), 302–318. https://doi.org/10.15252/embj.201592929

Liu, Y., Salter, H. K., Holding, A. N., Johnson, C. M., Stephens, E., Lukavsky, P. J., Walshaw, J., & Bullock, S. L. (2013). Bicaudal-D uses a parallel, homodimericcoiled coil with heterotypic registry tocoordinate recruitment of cargos to dynein. *Genes and Development*, *27*(11), 1233–1246. https://doi.org/10.1101/gad.212381.112

Lo, K. Y., Kuzmin, A., Unger, S. M., Petersen, J. D., & Silverman, M. A. (2011). KIF1A is the primary anterograde motor protein required for the ax-

onal transport of dense-core vesicles in cultured hippocampal neurons. *Neuroscience Letters*, *491*(3), 168–173. https://doi.org/10.1016/j.neulet.2011.01.018

Maday, S., Twelvetrees, A. E., Moughamian, A. J., & Holzbaur, E. L. (2014). Axonal Transport: Cargo-Specific Mechanisms of Motility and Regulation. https://doi.org/10.1016/j.neuron.2014.10.019

Maldonado-Báez, L., Cole, N. B., Krämer, H., & Donaldson, J. G. (2013). Microtubule-dependent endosomal sorting of clathrin-independent cargo by Hook1. *Journal of Cell Biology*, *201*(2), 233–247. https://doi.org/10.1083/jcb.201208172

Matsushita, M., Tanaka, S., Nakamura, N., Inoue, H., & Kanazawa, H. (2004). A novel kinesin-like protein, KIF1Bβ3 is involved in the movement of lysosomes ot the cell periphery in non-neuronal cells. *Traffic*, *5*(3), 140–151. https://doi.org/10.1111/j.1600-0854.2003.00165.x

McDonald, H. B., Stewart, R. J., & Goldstein, L. S. (1990). The kinesin-like ncd protein of Drosophila is a minus end-directed microtubule motor. *Cell*, *63*(6), 1159–1165. https://doi.org/10.1016/0092-8674(90)90412-8

McKenney, R. J., Huynh, W., Tanenbaum, M. E., Bhabha, G., & Vale, R. D. (2014). Activation of cytoplasmic dynein motility by dynactin-cargo adapter complexes. *Science*, *345*(6194), 337–341. https://doi.org/10.1126/science.1254198

McKenney, R. J., Huynh, W., Vale, R. D., & Sirajuddin, M. (2016). Tyrosination of α-tubulin controls the initiation of processive dynein–dynactin motility. *The EMBO Journal*, *35*(11), 1175–1185. https://doi.org/10.15252/embj.201593071

Miki, H., Okada, Y., & Hirokawa, N. (2005). Analysis of the kinesin superfamily: Insights into structure and function. https://doi.org/10.1016/j.tcb.2005.07.006

Miller, P. M., Folkmann, A. W., Maia, A. R., Efimova, N., Efimov, A., & Kaverina, I. (2009). Golgi-derived CLASP-dependent microtubules control Golgi organization and polarized trafficking in motile cells. *Nature Cell Biology*, *11*(9), 1069–1080. https://doi.org/10.1038/ncb1920

Mitchison, T., & Kirschner, M. (1984). Dynamic instability of microtubule growth. *Nature*, *312*(5991), 237–242. https://doi.org/10.1038/312237a0

Mogessie, B., Roth, D., Rahil, Z., & Straube, A. (2015). A novel isoform of MAP4 organises the paraxial microtubule array required for muscle

cell differentiation. *eLife*, *2015*(4), 1–28. https://doi.org/10.7554/eLife. 05697

Monroy, B. Y., Sawyer, D. L., Ackermann, B. E., Borden, M. M., Tan, T. C., & Ori-Mckenney, K. M. (2018). Competition between microtubule-associated proteins directs motor transport. *Nature Communications*, *9*(1), 1–12. https://doi.org/10.1038/s41467-018-03909-2

Monroy, B. Y., Tan, T. C., Oclaman, J. M., Han, J. S., Simó, S., Niwa, S., Nowakowski, D. W., McKenney, R. J., & Ori-McKenney, K. M. (2020). A Combinatorial MAP Code Dictates Polarized Microtubule Transport. *Developmental Cell*, *53*(1), 60–72. https://doi.org/10.1016/j.devcel. 2020.01.029

Moss, D. K., Bellett, G., Carter, J. M., Liovic, M., Keynton, J., Prescott, A. R., Lane, E. B., & Mogensen, M. M. (2007). Ninein is released from the centrosome and moves bi-directionally along microtubules. *Journal of Cell Science*, *120*(17), 3064–3074. https://doi.org/10.1242/jcs.010322

Nakagawa, T., Setou, M., Seog, D. H., Ogasawara, K., Dohmae, N., Takio, K., & Hirokawa, N. (2000). A novel motor, KIF13A, transports mannose-6-phosphate receptor to plasma membrane through direct interaction with AP-1 complex. *Cell*, *103*(4), 569–581. https://doi.org/10.1016/S0092-8674(00)00161-6

Nangaku, M., Sato-Yoshitake, R., Okada, Y., Noda, Y., Takemura, R., Yamazaki, H., & Hirokawa, N. (1994). KIF1B, a novel microtubule plus end-directed monomeric motor protein for transport of mitochondria. *Cell*, *79*(7), 1209–1220. https://doi.org/10.1016/0092-8674(94)90012-4

Nguyen, H. L., Chari, S., Gruber, D., Lue, C. M., Chapin, S. J., & Bulinski, J. C. (1997). Overexpression of full- or partial-length MAP4 stabilizes microtubules and alters cell growth. *Journal of Cell Science*, *110*(2), 281–294.

Nogales, E. (2001). Structural Insights into Microtubule Function. *Annual Review of Biophysics and Biomolecular Structure*, *30*(1), 397–420. https://doi.org/10.1146/annurev.biophys.30.1.397

Okada, Y., Yamazaki, H., Sekine-Aizawa, Y., & Hirokawa, N. (1995). The neuron-specific kinesin superfamily protein KIF1A is a uniqye monomeric motor for anterograde axonal transport of synaptic vesicle precursors. *Cell*, *81*(5), 769–780. https://doi.org/10.1016/0092-8674(95)90538-3

Olenick, M. A., Tokito, M., Boczkowska, M., Dominguez, R., & Holzbaur, E. L. (2016). Hook adaptors induce unidirectional processive motility by enhancing the Dynein-Dynactin interaction. *Journal of Biological Chemistry*, *291*(35), 18239–18251. https://doi.org/10.1074/jbc.M116.738211

Oteyza, A. C., Battalo□lu, E., Ocek, L., Lindig, T., Reichbauer, J., Rebelo, A. P., Gonzalez, M. A., Zorlu, Y., Ozes, B., Timmann, D., Bender, B., Woehlke, G., Züchner, S., Schöls, L., & Schüle, R. (2014). Motor protein mutations cause a new form of hereditary spastic paraplegia. *Neurology*, *82*(22), 2007–2016. https://doi.org/10.1212/WNL.0000000000000479

Pamula, M. C., Ti, S. C., & Kapoor, T. M. (2016). The structured core of human β tubulin confers isotype-specific polymerization properties. *Journal of Cell Biology*, *213*(4), 425–433. https://doi.org/10.1083/jcb.201603050

Panda, D., Miller, H. P., Banerjee, A., Ludueña, R. F., & Wilson, L. (1994). Microtubule dynamics in vitro are regulated by the tubulin isotype composition. *Proceedings of the National Academy of Sciences of the United States of America*, *91*(24), 11358–11362. https://doi.org/10.1073/pnas.91.24.11358

Parker, A. L., Teo, W. S., McCarroll, J. A., & Kavallaris, M. (2017). An emerging role for tubulin isotypes in modulating cancer biology and chemotherapy resistance. https://doi.org/10.3390/ijms18071434

Patel, N. M., Siva, M. S. A., Kumari, R., Shewale, D. J., Rai, A., Ritt, M., Sharma, P., Setty, S. R. G., Sivaramakrishnan, S., & Soppina, V. (2021). KIF13A motors are regulated by Rab22A to function as weak dimers inside the cell. *Science Advances*, *7*(6), eabd2054. https://doi.org/10.1126/sciadv.abd2054

Peet, D. R., Burroughs, N. J., & Cross, R. A. (2018). Kinesin expands and stabilizes the GDP-microtubule lattice. *Nature Nanotechnology*, *13*(5), 386–391. https://doi.org/10.1038/s41565-018-0084-4

Pennings, M., Schouten, M. I., van Gaalen, J., Meijer, R. P., de Bot, S. T., Kriek, M., Saris, C. G., van den Berg, L. H., van Es, M. A., Zuidgeest, D. M., Elting, M. W., van de Kamp, J. M., van Spaendonck-Zwarts, K. Y., Die-Smulders, C. d., Brilstra, E. H., Verschuuren, C. C., de Vries, B. B., Bruijn, J., Sofou, K., … Kamsteeg, E. J. (2020). KIF1A variants are a frequent cause of autosomal dominant hereditary spastic paraplegia.

European Journal of Human Genetics, *28*(1), 40–49. https://doi.org/10.1038/s41431-019-0497-z

Qiang, L., Sun, X., Austin, T. O., Muralidharan, H., Jean, D. C., Liu, M., Yu, W., & Baas, P. W. (2018). Tau Does Not Stabilize Axonal Microtubules but Rather Enables Them to Have Long Labile Domains. *Current Biology*, *28*(13), 2181–2189. https://doi.org/10.1016/j.cub.2018.05.045

Raaijmakers, J. A., Tanenbaum, M. E., & Medema, R. H. (2013). Systematic dissection of dynein regulators in mitosis. *Journal of Cell Biology*, *201*(2), 201–215. https://doi.org/10.1083/jcb.201208098

Rai, A. K., Rai, A., Ramaiya, A. J., Jha, R., & Mallik, R. (2013). Molecular adaptations allow dynein to generate large collective forces inside cells. *Cell*, *152*(1-2), 172–182. https://doi.org/10.1016/j.cell.2012.11.044

Rashid, D. J., Bononi, J., Tripet, B. P., Hodges, R. S., & Pierce, D. W. (2005). Monomeric and dimeric states exhibited by the kinesin-related motor protein KIF1A. *Journal of Peptide Research*, *65*(6), 538–549. https://doi.org/10.1111/j.1399-3011.2005.00255.x

Reck-Peterson, S. L., Redwine, W. B., Vale, R. D., & Carter, A. P. (2018). The cytoplasmic dynein transport machinery and its many cargoes. *Nature Reviews Molecular Cell Biology*, *19*(6), 382–398. https://doi.org/10.1038/s41580-018-0004-3

Redwine, W. B., DeSantis, M. E., Hollyer, I., Htet, Z. M., Tran, P. T., Swanson, S. K., Florens, L., Washburn, M. P., & Reck-Peterson, S. L. (2017). The human cytoplasmic dynein interactome reveals novel activators of motility. *eLife*, *6*, 1–27. https://doi.org/10.7554/eLife.28257

Roberts, A. J., Kon, T., Knight, P. J., Sutoh, K., & Burgess, S. A. (2013). Functions and mechanics of dynein motor proteins. *Nature Reviews Molecular Cell Biology*, *14*(11), 713–726. https://doi.org/10.1038/nrm3667

Roossien, D. H., Miller, K. E., & Gallo, G. (2015). Ciliobrevins as tools for studying dynein motor function. *Frontiers in cellular neuroscience*, *9*(July), 252. https://doi.org/10.3389/fncel.2015.00252

Ross, J. L., Shuman, H., Holzbaur, E. L. F., & Goldman, Y. E. (2008). Kinesin and dynein-dynactin at intersecting microtubules: motor density affects dynein function. *Biophysical journal*, *94*(8), 3115–25. https://doi.org/10.1529/biophysj.107.120014

Roux, K. J., Kim, D. I., Raida, M., & Burke, B. (2012). A promiscuous biotin ligase fusion protein identifies proximal and interacting proteins

in mammalian cells. *Journal of Cell Biology*, *196*(6), 801–810. https: //doi.org/10.1083/jcb.201112098

Sagona, A. P., Nezis, I. P., Pedersen, N. M., Liestøl, K., Poulton, J., Rusten, T. E., Skotheim, R. I., Raiborg, C., & Stenmark, H. (2010). PtdIns(3)P controls cytokinesis through KIF13A-mediated recruitment of FYVE-CENT to the midbody. *Nature Cell Biology*, *12*(4), 362–371. https:// doi.org/10.1038/ncb2036

Sainath, R., & Gallo, G. (2015). The dynein inhibitor Ciliobrevin D inhibits the bidirectional transport of organelles along sensory axons and impairs NGF-mediated regulation of growth cones and axon branches. *Devel-opmental Neurobiology*, *75*(7), 757–777. https://doi.org/10.1002/ dneu.22246

Scarabelli, G., Soppina, V., Yao, X. Q., Atherton, J., Moores, C. A., Verhey, K. J., & Grant, B. J. (2015). Mapping the Processivity Determinants of the Kinesin-3 Motor Domain. *Biophysical Journal*, *109*(8), 1537–1540. https://doi.org/10.1016/j.bpj.2015.08.027

Schindelin, J., Arganda-Carreras, I., Frise, E., Kaynig, V., Longair, M., Piet-zsch, T., Preibisch, S., Rueden, C., Saalfeld, S., Schmid, B., Tinevez, J. Y., White, D. J., Hartenstein, V., Eliceiri, K., Tomancak, P., & Car-dona, A. (2012). Fiji: An open-source platform for biological-image analysis. https://doi.org/10.1038/nmeth.2019

Schlager, M. A., Hoang, H. T., Urnavicius, L., Bullock, S. L., & Carter, A. P. (2014). In vitro reconstitution of a highly processive recombinant hu-man dynein complex. *The EMBO Journal*, *33*(17), 1855–1868. https: //doi.org/10.15252/embj.201488792

Schlager, M. A., Kapitein, L. C., Grigoriev, I., Burzynski, G. M., Wulf, P. S., Keijzer, N., de Graaff, E., Fukuda, M., Shepherd, I. T., Akhmanova, A., & Hoogenraad, C. C. (2010). Pericentrosomal targeting of Rab6 secretory vesicles by Bicaudal-D-related protein 1 (BICDR-1) regu-lates neuritogenesis. *The EMBO Journal*, *29*(10), 1637–1651. https: //doi.org/10.1038/emboj.2010.51

Schneider, F., Sych, T., Eggeling, C., & Sezgin, E. (2021). Influence of nanobody binding on fluorescence emission, mobility, and organiza-tion of GFP-tagged proteins. *iScience*, *24*(1), 101891. https://doi.org/ 10.1016/j.isci.2020.101891

Scholz, D., Pöltl, D., Genewsky, A., Weng, M., Waldmann, T., Schildknecht, S., & Leist, M. (2011). Rapid, complete and large-scale generation of

post-mitotic neurons from the human LUHMES cell line. *Journal of Neurochemistry, 119*(5), 957–971. https://doi.org/10.1111/j.1471-4159.2011.07255.x

Schroeder, C. M., & Vale, R. D. (2016). Assembly and activation of dynein-dynactin by the cargo adaptor protein Hook3. *Journal of Cell Biology*. https://doi.org/10.1083/jcb.201604002

Shin, H., Wyszynski, M., Huh, K. H., Valtschanoff, J. G., Lee, J. R., Ko, J., Streuli, M., Weinberg, R. J., Sheng, M., & Kim, E. (2003). Association of the kinesin motor KIF1A with the multimodular protein liprin-α. *Journal of Biological Chemistry, 278*(13), 11393–11401. https://doi.org/10.1074/jbc.M211874200

Siddiqui, N., & Straube, A. (2017). Intracellular cargo transport by kinesin-3 motors. *Biochemistry (Moscow), 82*(7), 803–815. https://doi.org/10.1134/S0006297917070057

Siddiqui, N. (2018). *Regulation of KIF1C transport* (Doctoral dissertation). University of Warwick.

Siddiqui, N., Zwetsloot, A. J., Bachmann, A., Roth, D., Hussain, H., Brandt, J., Kaverina, I., & Straube, A. (2019). PTPN21 and Hook3 relieve KIF1C autoinhibition and activate intracellular transport. *Nature Communications, 10*(1). https://doi.org/10.1038/s41467-019-10644-9

Sirajuddin, M., Rice, L. M., & Vale, R. D. (2014). Regulation of microtubule motors by tubulin isotypes and post-translational modifications. *Nature Cell Biology, 16*(4), 335–344. https://doi.org/10.1038/ncb2920

Song, Y., Kirkpatrick, L. L., Schilling, A. B., Helseth, D. L., Chabot, N., Keillor, J. W., Johnson, G. V., & Brady, S. T. (2013). Transglutaminase and Polyamination of Tubulin: Posttranslational Modification for Stabilizing Axonal Microtubules. *Neuron, 78*(1), 109–123. https://doi.org/10.1016/j.neuron.2013.01.036

Soppina, V., Rai, A. K., Ramaiya, A. J., Barak, P., & Mallik, R. (2009). Tug-of-war between dissimilar teams of microtubule motors regulates transport and fission of endosomes. *Proceedings of the National Academy of Sciences of the United States of America, 106*(46), 19381–19386. https://doi.org/10.1073/pnas.0906524106

Soppina, V., & Verhey, K. J. (2014). The family-specific K-loop influences the microtubule on-rate but not the superprocessivity of kinesin-3 motors. *Molecular biology of the cell, 25*(14), 2161–70. https://doi.org/10.1091/mbc.E14-01-0696

Splinter, D., Tanenbaum, M. E., Lindqvist, A., Jaarsma, D., Flotho, A., Yu, K. L., Grigoriev, I., Engelsma, D., Haasdijk, E. D., Keijzer, N., Demmers, J., Fornerod, M., Melchior, F., Hoogenraad, C. C., Medema, R. H., & Akhmanova, A. (2010). Bicaudal D2, dynein, and kinesin-1 associate with nuclear pore complexes and regulate centrosome and nuclear positioning during mitotic entry. *PLoS Biology*, *8*(4). https://doi.org/10.1371/journal.pbio.1000350

Steinman, J. B., Santarossa, C. C., Miller, R. M., Yu, L. S., Serpinskaya, A. S., Furukawa, H., Morimoto, S., Tanaka, Y., Nishitan, M., Asano, M., Zalyte, R., Ondrus, A. E., Johnson, A. G., Ye, F., Nachury, M. V., Fukase, Y., Aso, K., Foley, M. A., Gelfand, V. I., … Kapoor, T. M. (2017). Chemical structure-guided design of dynapyrazoles, cell-permeable dynein inhibitors with a unique mode of action. *eLife*, *6*. https://doi.org/10.7554/eLife.25174

Svoboda, K., Schmidt, C. F., Schnapp, B. J., & Block, S. M. (1993). Direct observation of kinesin stepping by optical trapping interferometry. *Nature*, *365*(6448), 721–727. https://doi.org/10.1038/365721a0

Tanaka, Y., Niwa, S., Dong, M., Farkhondeh, A., Wang, L., Zhou, R., & Hirokawa, N. (2016). The Molecular Motor KIF1A Transports the TrkA Neurotrophin Receptor and Is Essential for Sensory Neuron Survival and Function. *Neuron*, *90*(6), 1215–1229. https://doi.org/10.1016/j.neuron.2016.05.002

Tas, R. P., Chazeau, A., Cloin, B. M., Lambers, M. L., Hoogenraad, C. C., & Kapitein, L. C. (2017). Differentiation between Oppositely Oriented Microtubules Controls Polarized Neuronal Transport. *Neuron*, *96*(6), 1264–1271. https://doi.org/10.1016/j.neuron.2017.11.018

Telley, I. A., Bieling, P., & Surrey, T. (2009). Obstacles on the microtubule reduce the processivity of kinesin-1 in a minimal in vitro system and in cell extract. *Biophysical Journal*, *96*(8), 3341–3353. https://doi.org/10.1016/j.bpj.2009.01.015

Theisen, U., Straube, E., & Straube, A. (2012). Directional Persistence of Migrating Cells Requires Kif1C-Mediated Stabilization of Trailing Adhesions. *Developmental Cell*, *23*(6), 1153–1166. https://doi.org/10.1016/j.devcel.2012.11.005

Thorn, K. S., Ubersax, J. A., & Vale, R. D. (2000). Engineering the processive run length of the kinesin motor. *Journal of Cell Biology*, *151*(5), 1093–1100. https://doi.org/10.1083/jcb.151.5.1093

Ti, S. C., Alushin, G. M., & Kapoor, T. M. (2018). Human β-Tubulin Isotypes Can Regulate Microtubule Protofilament Number and Stability. *Developmental Cell*, *47*(2), 175–190. https://doi.org/10.1016/j.devcel.2018.08.014

Tinevez, J. Y., Perry, N., Schindelin, J., Hoopes, G. M., Reynolds, G. D., Laplantine, E., Bednarek, S. Y., Shorte, S. L., & Eliceiri, K. W. (2017). TrackMate: An open and extensible platform for single-particle tracking. *Methods*, *115*, 80–90. https://doi.org/10.1016/j.ymeth.2016.09.016

Tokuraku, K., Katsuki, M., Nakagawa, H., & Kotani, S. (1999). A new model for microtubule-associated protein (MAP)-induced microtubule assembly. *European Journal of Biochemistry*, *259*(1-2), 158–166. https://doi.org/10.1046/j.1432-1327.1999.00019.x

Torisawa, T., Ichikawa, M., Furuta, A., Saito, K., Oiwa, K., Kojima, H., Toyoshima, Y. Y., & Furuta, K. (2014). Autoinhibition and cooperative activation mechanisms of cytoplasmic dynein. *Nature Cell Biology*, *16*(11), 1118–1124. https://doi.org/10.1038/ncb3048

Toropova, K., Zou, S., Roberts, A. J., Redwine, W. B., Goodman, B. S., Reck-Peterson, S. L., & Leschziner, A. E. (2014). Lis1 regulates dynein by sterically blocking its mechanochemical cycle. *eLife*, *3*, 3372. https://doi.org/10.7554/eLife.03372

Triclin, S., Inoue, D., Gaillard, J., Htet, Z. M., DeSantis, M. E., Portran, D., Derivery, E., Aumeier, C., Schaedel, L., John, K., Leterrier, C., Reck-Peterson, S. L., Blanchoin, L., & Théry, M. (2021). Self-repair protects microtubules from destruction by molecular motors. *Nature Materials*, 1–9. https://doi.org/10.1038/s41563-020-00905-0

Twelvetrees, A. E., Lesept, F., Holzbaur, E. L., & Kittler, J. T. (2019). The adaptor proteins HAP1a and GRIP1 collaborate to activate the kinesin-1 isoform KIF5C. *Journal of Cell Science*, *132*(24). https://doi.org/10.1242/jcs.215822

Twelvetrees, A. E. E., Pernigo, S., Sanger, A., Guedes-Dias, P., Schiavo, G., Steiner, R. A. A., Dodding, M. P. P., & Holzbaur, E. L. L. (2016). The Dynamic Localization of Cytoplasmic Dynein in Neurons Is Driven by Kinesin-1. *Neuron*, *90*(5), 1000–1015. https://doi.org/10.1016/j.neuron.2016.04.046

Ueno, H., Huang, X., Tanaka, Y., & Hirokawa, N. (2011). KIF16B/Rab14 Molecular Motor Complex Is Critical for Early Embryonic Develop-

ment by Transporting FGF Receptor. *Developmental Cell*, *20*(1), 60–71. https://doi.org/10.1016/j.devcel.2010.11.008

Uhlén, M., Fagerberg, L., Hallström, B. M., Lindskog, C., Oksvold, P., Mardinoglu, A., Sivertsson, Å., Kampf, C., Sjöstedt, E., Asplund, A., Olsson, I. M., Edlund, K., Lundberg, E., Navani, S., Szigyarto, C. A. K., Odeberg, J., Djureinovic, D., Takanen, J. O., Hober, S., … Pontén, F. (2015). Tissue-based map of the human proteome. *Science*, *347*(6220). https://doi.org/10.1126/science.1260419

Ulbrich, M. H., & Isacoff, E. Y. (2007). Subunit counting in membrane-bound proteins. *Nature Methods*, *4*(4), 319–321. https://doi.org/10.1038/nmeth1024

Urnavicius, L., Lau, C. K., Elshenawy, M. M., Morales-Rios, E., Motz, C., Yildiz, A., & Carter, A. P. (2017). Cryo-EM shows how dynactin recruits two dyneins for faster movement. *bioRxiv*. http://www.biorxiv.org/content/early/2017/08/31/183160

Urnavicius, L., Lau, C. K., Elshenawy, M. M., Morales-Rios, E., Motz, C., Yildiz, A., & Carter, A. P. (2018). Cryo-EM shows how dynactin recruits two dyneins for faster movement. *Nature*, *554*(7691), 202–206. https://doi.org/10.1038/nature25462

Urnavicius, L., Zhang, K., Diamant, A. G., Motz, C., Schlager, M. A., Yu, M., Patel, N. A., Robinson, C. V., & Carter, A. P. (2015). The structure of the dynactin complex and its interaction with dynein. *Science*. https://doi.org/10.1126/science.aaa4080

van Spronsen, M., Mikhaylova, M., Lipka, J., Schlager, M. A., van den Heuvel, D. J., Kuijpers, M., Wulf, P. S., Keijzer, N., Demmers, J., Kapitein, L. C., Jaarsma, D., Gerritsen, H. C., Akhmanova, A., & Hoogenraad, C. C. (2013). TRAK/Milton Motor-Adaptor Proteins Steer Mitochondrial Trafficking to Axons and Dendrites. *Neuron*, *77*(3), 485–502. https://doi.org/10.1016/j.neuron.2012.11.027

Vemu, A., Atherton, J., Spector, J. O., Szyk, A., Moores, C. A., & Roll-Mecak, A. (2016). Structure and dynamics of single-isoform recombinant neuronal human tubulin. *Journal of Biological Chemistry*, *291*(25), 12907–12915. https://doi.org/10.1074/jbc.C116.731133

Virtanen, P., Gommers, R., Oliphant, T. E., Haberland, M., Reddy, T., Cournapeau, D., Burovski, E., Peterson, P., Weckesser, W., Bright, J., van der Walt, S. J., Brett, M., Wilson, J., Millman, K. J., Mayorov, N., Nelson, A. R., Jones, E., Kern, R., Larson, E., … Vázquez-Baeza, Y. (2020).

SciPy 1.0: fundamental algorithms for scientific computing in Python. *Nature Methods*, *17*(3), 261–272. https://doi.org/10.1038/s41592-019-0686-2

Vuolo, L., Stevenson, N. L., Heesom, K. J., & Stephens, D. J. (2018). Dynein-2 intermediate chains play crucial but distinct roles in primary cilia formation and function. *eLife*, *7*. https://doi.org/10.7554/eLife.39655

Vuolo, L., Stevenson, N. L., Mukhopadhyay, A. G., Roberts, A. J., & Stephens, D. J. (2020). Cytoplasmic dynein-2 at a glance. https://doi.org/10.1242/jcs.240614

Walker, R. A., Salmon, E. D., & Endow, S. A. (1990). The Drosophila claret segregation protein is a minus-end directed motor molecule. *Nature*, *347*(6295), 780–782. https://doi.org/10.1038/347780a0

Wang, Z., Khan, S., & Sheetzt, M. P. (1995). *Single Cytoplasmic Dynein Molecule Movements: Characterization and Comparison with Kinesin* (tech. rep.). https://doi.org/10.1016/S0006-3495(95)80071-8

Waterman-Storer, C. M., Karki, S. B., Kuznetsov, S. a., Tabb, J. S., Weiss, D. G., Langford, G. M., & Holzbaur, E. L. (1997). The interaction between cytoplasmic dynein and dynactin is required for fast axonal transport. *Proceedings of the National Academy of Sciences of the United States of America*, *94*(22), 12180–12185. https://doi.org/10.1073/pnas.94.22.12180

Watson, P., & Stephens, D. J. (2006). Microtubule plus-end loading of p150Glued is mediated by EB1 and CLIP-170 but is not required for intracellular membrane traffic in mammalian cells. *Journal of Cell Science*, *119*(13), 2758–2767. https://doi.org/10.1242/jcs.02999

Wegmann, S., Eftekharzadeh, B., Tepper, K., Zoltowska, K. M., Bennett, R. E., Dujardin, S., Laskowski, P. R., MacKenzie, D., Kamath, T., Commins, C., Vanderburg, C., Roe, A. D., Fan, Z., Molliex, A. M., Hernandez☐Vega, A., Muller, D., Hyman, A. A., Mandelkow, E., Taylor, J. P., & Hyman, B. T. (2018). Tau protein liquid–liquid phase separation can initiate tau aggregation. *The EMBO Journal*, *37*(7), e98049. https://doi.org/10.15252/embj.201798049

Wharton, R. P., & Struhl, G. (1989). Structure of the Drosophila BicaudalD protein and its role in localizing the posterior determinant nanos. *Cell*, *59*(5), 881–892. https://doi.org/10.1016/0092-8674(89)90611-9

Wickstead, B., & Gull, K. (2006). A "Holistic" Kinesin Phylogeny Reveals New Kinesin Families and Predicts Protein Functions. *Molecular biology of the cell*, *17*(1), 1734–1743. https://doi.org/10.1091/mbc.E05

Wienken, C. J., Baaske, P., Rothbauer, U., Braun, D., & Duhr, S. (2010). Protein-binding assays in biological liquids using microscale thermophoresis. *Nature Communications*, *1*(7). https://doi.org/10.1038/ncomms1093

Wordeman, L., & Mitchison, T. J. (1995). Identification and partial characterization of mitotic centromere- associated kinesin, a kinesin-related protein that associates with centromeres during mitosis. *Journal of Cell Biology*, *128*(1-2), 95–105. https://doi.org/10.1083/jcb.128.1.95

Xing, B. M., Yang, Y. R., Du, J. X., Chen, H. J., Qi, C., Huang, Z. H., Zhang, Y., & Wang, Y. (2012). Cyclin-dependent kinase 5 controls TRPV1 membrane trafficking and the heat sensitivity of nociceptors through KIF13B. *Journal of Neuroscience*, *32*(42), 14709–14721. https://doi.org/10.1523/JNEUROSCI.1634-12.2012

Xu, L., Sowa, M. E., Chen, J., Li, X., Gygi, S. P., & Harper, J. W. (2008). An FTS/Hook/p107FHIP complex interacts with and promotes endosomal clustering by the homotypic vacuolar protein sorting complex. *Molecular Biology of the Cell*. https://doi.org/10.1091/mbc.E08-05-0473

Yamada, K. H., Hanada, T., & Chishti, A. H. (2007). The effector domain of human Dlg tumor suppressor acts as a switch that relieves autoinhibition of kinesin-3 motor GAKIN/KIF13B. *Biochemistry*, *46*(35), 10039–10045. https://doi.org/10.1021/bi701169w

Yamada, K. H., Nakajima, Y., Geyer, M., Wary, K. K., Ushio-Fukai, M., Komarova, Y., & Malik, A. B. (2014). KIF13B regulates angiogenesis through Golgi to plasma membrane trafficking of VEGFR2. *Journal of Cell Science*, *127*(20), 4518–4530. https://doi.org/10.1242/jcs.156109

Yi, J. Y., Ori-McKenney, K. M., McKenney, R. J., Vershinin, M., Gross, S. P., & Vallee, R. B. (2011). High-resolution imaging reveals indirect coordination of opposite motors and a role for LIS1 in high-load axonal transport. *Journal of Cell Biology*, *195*(2), 193–201. https://doi.org/10.1083/jcb.201104076

Yücel-Yılmaz, D., Yücesan, E., Yalnızoğlu, D., Oğuz, K. K., Sağıroğlu, M. Ş., Özbek, U., Serdaroğlu, E., Bilgiç, B., Erdem, S., İşeri, S. A. U., Hanağası, H., Gürvit, H., Özgül, R. K., & Dursun, A. (2018). Clinical phenotype of hereditary spastic paraplegia due to KIF1C gene muta-

tions across life span. *Brain and Development*, *40*(6), 458–464. https: //doi.org/10.1016/j.braindev.2018.02.013

Zhang, J., Li, S., Fischer, R., & Xiang, X. (2003). Accumulation of cytoplasmic dynein and dynactin at microtubule plus ends in Aspergillus nidulans is kinesin dependent. *Molecular Biology of the Cell*, *14*(4), 1479–1488. https://doi.org/10.1091/mbc.E02-08-0516

Zhang, K., Foster, H. E., Rondelet, A., Lacey, S. E., Bahi-Buisson, N., Bird, A. W., & Carter, A. P. (2017). Cryo-EM Reveals How Human Cytoplasmic Dynein Is Auto-inhibited and Activated. *Cell*, *169*(7), 1303–1314. https://doi.org/10.1016/j.cell.2017.05.025

Zhang, Z., Goldtzvik, Y., & Thirumalai, D. (2017). Parsing the roles of neck-linker docking and tethered head diffusion in the stepping dynamics of kinesin. *Proceedings of the National Academy of Sciences of the United States of America*, *114*(46), E9838–E9845. https://doi.org/10. 1073/pnas.1706014114

Zhou, R., Niwa, S., Guillaud, L., Tong, Y., & Hirokawa, N. (2013). A Molecular Motor, KIF13A, Controls Anxiety by Transporting the Serotonin Type 1A Receptor. *Cell Reports*, *3*(2), 509–519. https://doi.org/10.1016/j. celrep.2013.01.014

Zwetsloot, A. J., Tut, G., & Straube, A. (2018). Measuring microtubule dynamics. *Essays in Biochemistry*, *0*(October), 1–11. https://doi.org/10.1042/ EBC20180035